DESIGN OF A 7 DEGREE-OF-FREEDOM HAPTIC ROBOT

By

Christopher E. Marince

Thesis

Submitted to the Faculty of the

Graduate School of Vanderbilt University in

partial fulfillment of the requirements

for the degree of

MASTER OF SCIENCE

in

Mechanical Engineering

August, 2015

Nashville, Tennessee

Approved:

Robert J. Webster III

Thomas Withrow

Alvin Strauss

ACKNOWLEDGMENTS

This research was completed with unwavering support from Vanderbilt University and, specifically, the Medical Engineering and Discovery Lab.

I would like to thank Professor Robert J. Webster III for allowing me to take on an ambitious project to benefit the MEDLab and for being an inspirational mentor.

I would like to thank Hunter Gilbert for his hands-on guidance through every step of the project. The knowledge I have gained in our work together, in both theoretical and practical matters, is immeasurably beneficial.

I would like to thank Ray Lathrop for his many design contributions to the project.

I would like to thank Rich Hendrick for his guidance through kinematics and dynamics.

I would like to thank the Professor Webster, Professor Withrow, Professor Strauss, and Phil Swaney for their suggestions regarding my thesis and defense.

I would like to thank Suzanne Weiss and Myrtle Daniels for assisting with the logistics in successfully completing this degree.

I would like to thank Alex Pedchanko and Jake Noble for their support in handling the adversity and stress associated with completing this research.

I would like to thank Michael, Sarah, and Millie Marince for supporting me through my work in both undergraduate and graduate studies.

Finally, I would like to thank my parents, Mary Kay and Gary Marince, for their continual support through all of my endeavors. Thank you for consistently believing in me and doing your best to keep my life moving in the right direction.

TABLE OF CONTENTS

LIST OF FIGURES

LIST OF TABLES

CHAPTER I

INTRODUCTION AND BACKGROUND

Motivation

Robot-assisted surgical systems are becoming increasingly common in medical procedures as they embrace many of the benefits of minimally invasive surgery including decreased patient trauma, reduced recovery time, and less financially costly treatment [1]. Medical errors can cause tissue trauma and can even result in fatal consequences. It has been found that over 400,000 deaths occurred in American hospitals due to medical errors per year [25]. The technology incorporated into surgical robots is promising for its potential to provide surgeons with superhuman capabilities. These abilities allow for procedures to be performed more safely and quickly when compared to procedures without robotic assistance. For example, robot-assisted surgical systems have the ability to dexterously navigate through tissue with both surgical tools and endoscopic cameras. These systems allow for relatively easy navigation within confined spaces where an operator's human hand would normally be greatly limited. This dexterity is further strengthened through motion scaling, which translates large motions by the operator into diminutive actions of the robotic end effector. Finally, hand tremors generated by the doctor may be filtered and removed by robotic systems [3][4]. In addition to these technical enhancements to single surgical procedures, the potential for telesurgery, in which a doctor trained in a specialty field can conduct a procedure over great distances without needing to travel, opens doors to healthcare for regions of the world currently limited in medical training and experience [4].

In order for these systems to be utilized most effectively, the doctors operating them must have a complete and thorough understanding of both the robot's abilities and the physiology of the human body. While the knowledge of how live tissue reacts to surgical procedures is gained through attending medical school and observing operations, the skills associated with successfully performing a procedure can only be developed through practice. Surgeons may receive limited practice for technically challenging procedures before performing them on live patients, because cadavers are expensive and involved procedures may only be able to be performed once. Additionally, mistakes are expected to occur during training and these can often render the rest of the cadaver useless for future studies [5]. Alternatively, many institutions use mannequins to represent a human body, but these fall short in simulating realism to the operator [6]. In desperate attempts to gain practical experience, students are even training venipuncture on other students [7]. These hindrances make training expensive for the hospital to provide to its surgeons, as a great number of repetitions may be necessary for a doctor to achieve full proficiency for a procedure. For example, one study has shown that a surgeon performing keyhole surgery requires 750 operations before he or she has perfected the skill [8].

One of the most promising teaching aides for surgeons is the medical training simulator. This technology simulates a three-dimensional environment for many different medical procedures. The operator manipulates a robot to navigate through virtual tissue as seen on a computer monitor. This method of practicing surgical procedures through robotic training simulators has been shown to be a more efficient mode of learning than the use of cadavers. Statistically, it is estimated that one hour of training using a robotics simulator can have the same effects as three hours of training on a human cadaver [9].

While existing surgical robots and virtual surgical trainers are useful, limitations still exist. The aspect of the surgical systems that generates the sense of realism to the user is haptic feedback, which is the sense of touch. Haptic feedback provides the user with kinesthetic information regarding the real or virtual environment of the operation [4][10]. Without such force feedback, the operator has to rely entirely on visual cues from tissue manipulation to decide whether the forces applied are appropriate. This is a challenge that even expert surgeons find difficult. For example, experienced cardiac surgeons inadvertently applied forces great enough to rip fine polypropylene sutures and damage tissue when training with the da Vinci surgical robot without haptic feedback [11]. However, when haptic feedback was included in the system, these surgeons applied more consistent tensions in sutures and caused less tissue harm [11]. In a study of blunt dissections, a comparison of robot-assisted surgery with and without haptic feedback revealed that errors resulting in tissue damage were decreased by 66% when force feedback was utilized [12]. These studies demonstrate the clear need for further research into haptic feedback as it applies to robot-assisted surgery and training.

Previous Research

Haptic robots have been an active area of research over the last 44 years for both general applications and medical purposes [5]. In addition to surgical applications, haptics are applied in flight simulators, video game systems, and mobile devices. These haptic devices are both kinesthetic and tactile. Kinesthetic feedback means the haptics apply sensations to joint muscles. Tactile feedback generates feeling through surface texture. The research has led to the application of a variety of actuation methods such as DC electric motors, pneumatics, hydraulics, shape memory metals, magnetics, piezoelectric materials, and electrorheological fluids. For all

haptic purposes, the goal of the designer is to optimize the accuracy and magnitude of the forces being returned to the user and the speed with which those forces are applied. Unfortunately, these two qualities are often trade-offs, thus, compromises must be made. In order to maintain the sense of realism for general tasks, the user must experience both forces and torques, along all six degrees of freedom of a general rigid body. This challenging requirement often results in difficulty maintaining both low cost and high performance, despite several decades of haptics research [5].

As such, the commercial availability for a haptic device and the number of degrees of freedom the haptic device offers are inversely related. In fact, the commercial availability of a seven degree-of-freedom haptic robot, similar to that being designed in this paper, is remarkably low. One of the few systems that provides seven degrees of force feedback is the MPB Technologies F7S: a system that provides a maximum torque of 2.5 Nm with a stiffness of 2 N/mm at a cost greater than $32,000. The Force Dimensions Omega 7 also provides seven degrees of freedom but only utilizes three for force feedback. However, the maximum torque feedback available is relatively large at 12 Nm [5]. The SensAble Technologies' Premium 1.0, 1.5, and 3.0 are all six degree of freedom systems that have scissor-grip and thumb-pad end-effectors available to increase their dexterity to seven degrees of freedom.

There are a number of six degree of freedom systems available for commercial use including the SensAble Technologies Premium 1.0, 1.5, and 3.0, the Force Dimensions Delta 6, the Haption Virtuose 6D Desktop, 6D35-45, 6D40-40, and INCA 6D, and the MPB Technologies Freedom 6S. The maximum torque feedback of these robots ranges considerably from 2.5 Nm to 100 Nm with maximum stiffness values of 1 to 3.5 N/mm. These machines cost between $20,000 and $140,000, correlating strongly with maximum torque feedback [5].

These haptic systems have been applied to medical training for a wide variety of specialties. One of the most common haptic studies is training for needle insertion. The Mediseus Epidural simulator uses a low-cost SensAble PHANTOM Omni and a modified syringe end effector to create a commercially available haptic system for needle insertion [17]. A higher-fidelity option, EpiSim from Yantric Inc., is available and uses a SensAble PHANTOM Desktop and a 6 DOF Premium to provide a more accurate simulation [18]. The National University of Singapore has developed an advanced feedback simulation for percutaneous vertebroplasty that requires the manipulation of three separate haptic devices [19]. At this point, the National University of Singapore's research is still cost restrictive with efforts towards a financially viable solution. There are also many other needle insertion tasks which have been simulated in a haptic environment, including acupuncture, catheter insertion, spine needle biopsy, lumbar punctures, and suturing for wound closure. Most of the haptic systems developed for these purposes are based on commercially available systems with modified end effectors [5]. The encouraging results of these studies call for more research into high degree of freedom haptic devices for needle insertion procedures.

There have been endeavors by other research institutions to build their own 7 degree-of-freedom haptic devices entirely independent of any existing commercially available systems. However, few of them provide force-feedback at all 7 joints, which is a major point of the design presented in this thesis. One example of a haptic robot that does provide force-feedback through all 7 degrees-of-freedom is the SPIDAR-G, which is a tendon-driven system developed by MIMIC Technologies in Seattle, WA. The SPIDAR-G's unique method of actuation uses eight cables to manipulate a sphere in the center of a cube. This allows the inertia felt by the user to be low but requires a very intricate design [20].

Contribution

This thesis presents the design and implementation of a four degree-of-freedom robot integrated with a preexisting three degree-of-freedom robot. This resulting seven degree-of-freedom haptic robot for use in robot-assisted surgery and surgical training is gravity-compensated to maximize the realism felt by the user.

Design Goals

The most important characteristic for any haptic robot is providing realistic force feedback. For a surgical robot, a realistic force can be related to a commonly performed medical practice such as suture tying. Approximately 2-5 N of force are produced during suture tying procedures [11]. The system shall be able to produce at least 2 N of force in all directions. This minimum value puts the force generated within the range expected in suture tying. Additionally, 2 Newtons is not enough force to injure the user. The torque requirements are largely based on the desire for the device to enforce that hand alignment matches the operator's view of a tool. Humans can produce on average about 13 to 18 N-m at the wrist [22]. The system shall be able to produce torques of at least 5% of these maximums, or .9 N-m about all axes.

As previously stated, low inertia is critical for providing a sense of transparency to the user. Thus, one of the design goals is to minimize the robot's mass. This is a notably challenging goal in that a 7 degree-of-freedom robot with force feedback inherently requires a significant amount of mass to function. At low speeds, the effects of the mass can be mitigated by statically balancing the device, which prevents the user from feeling the weight when not in motion. This also helps to minimize operator fatigue. The static weight felt by the operator shall be less than that of a 50 g mass, or .5 N.

Most commercially available haptic devices have a workspace of at least 10 cm in each direction. Very few of these systems exceed 50 cm in any particular direction [5]. A large workspace allows for the scaling of the user's actions so that he or she can make large natural movements, which are then interpreted and scaled down to small, precise movements by the slave robot. The system shall have a workspace of at least 10 cm in all directions. The angular workspace shall be at least ±45 degrees along all axes away from the designated starting position of the device.

There are also some design guidelines which are not quantified, but which informed the choice of kinematic mechanism. One key requirement for providing a sense of realism to the operator is low friction. An ideal system would have virtually no friction, thus, allowing the user to accurately feel the forces that are intentionally transmitted based on the virtual operating environment. In addition to minimizing friction, the device must have high stiffness. This will prevent any false motion of the end effector caused by unintended deflection.

One preexisting constraint on the robot is that it will be a 4 degree-of-freedom robot that must be compatible with the previously constructed 3 degree-of-freedom haptic robot constructed by Carl M. Perry in 1997 [21]. Thus, the goal is to build a 4 degree-of-freedom system and integrate the two together. The new additions shall not substantially restrict the workspace or capabilities of the 3 degree-of-freedom base robot. This workspace is described in the summary of the three degree-of-freedom base robot.

In summary, the quantitative performance requirements for the design are shown in Table 1-1. The following general guidelines were also used to inform the design

- Minimize the device's inertia
- Minimize the device's friction

- Maximize the device's workspace
- Maximize the device's stiffness

Maximum Force	2-5 N
Maximum Torque	900 mN-m
Translational Workspace	>10 cm in all axes
Angular Workspace	±45 degrees in all axes
Uncompensated Weight	< 50 mN

Table 1-1: Quantified design goals

Base Robot Summary

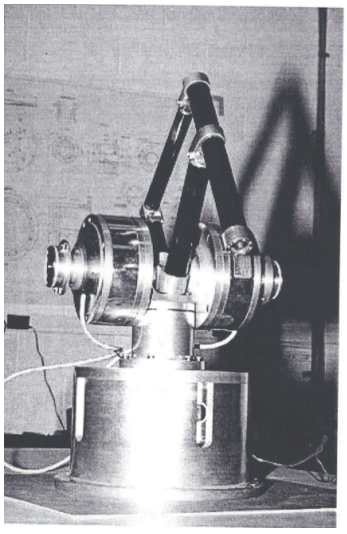

Figure 1-1: Complete base robot assembly

The 3 degree-of-freedom robot designed by Carl M. Perry is used to provide translation of the new 4 degree-of-freedom wrist and end effector. This base robot was built with the same intentions previously listed for the new haptic device. The system is a high-performance 3

degree-of-freedom system for haptic feedback with minimal rotational inertia and joint friction, low backlash between components, and high link stiffness [21].

The base robot has a serial-parallel configuration and uses a five bar linkage as a means of actuation. Two links of the five bar linkage are driven directly by Kollmorgen ServoDisc brushed DC motors with peak torques of 14.9 Nm. A Kollmorgen ServoDisc brushed DC motor with a peak torque of 37.02 Nm directly actuates the base of the robot. The range of motion for the two actuated links of the four bar linkage was measured to be 135° while the base can rotate ±90°. The links, made of thin-walled carbon fiber tubes, were designed to be lightweight but long enough to provide a reasonable workspace. Each has a mass under 90 g with a maximum length of 27.3 cm.

The 3 degrees-of-freedom associated with this robot provide the gross translational motions at the end effector of the new 7 DOF system. The translation motion achieves >10 cm in each direction, thereby satisfying one of the previously listed design requirements. Each Midori CP-5UY rotary potentiometer senses its respective shaft's rotation angle. These potentiometers are of high resolution with little noise and inertia. This data was not only utilized in determining the end effector's position, but also for calculating the joint velocities through differentiation.

CHAPTER II

GIMBAL DESIGN

Introduction

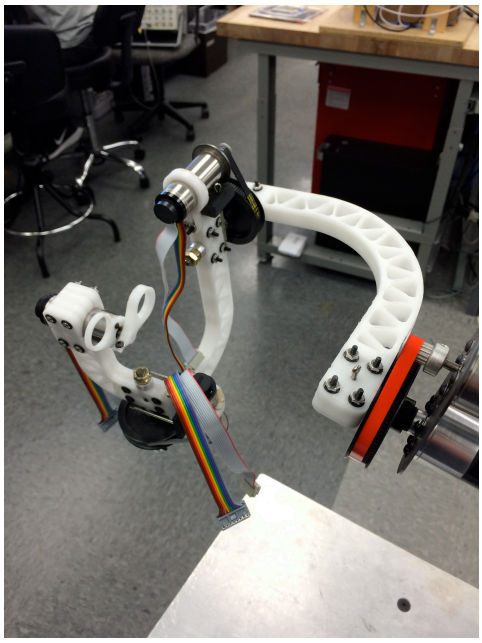

Figure 2-1: Complete gimbal assembly

The gimbal is one type of mechanism which has been successfully integrated into surgical haptic devices. This tool can be designed to provide a statically balanced, lightweight, natural method of controlling an end-effector. One of the more intricately designed high degree-of-freedom haptic robots that incorporates a gimbal is the Da Vinci Surgical System by Intuitive Surgical. This teleoperated robot is currently used for minimally invasive procedures, as its slave end effectors are small and precisely actuated. The workspace of the haptic user interface is of a reasonable size in that it is large enough to allow the user to move naturally and the system to utilize motion scaling effectively, yet small enough to where the links can maintain a low inertia

and a high stiffness. Intuitive Surgical's gimbal design, as seen in Figure 2-2, has been demonstrated to successfully achieve many of the design goals previously listed, though its haptics are not currently used in surgery; however, the interface is capable of haptics. As such, this mechanism served as the primary inspiration for the haptic end-effector presented in this thesis. The final gimbal design utilized in this thesis's system is featured in Figure 2-1.

Figure 2-2 da Vinci Surgical System Controller

Design Considerations

The goals previously listed were the guidelines that led to the final design, which is a three degree of freedom gimbal mechanism with a fourth gripper degree of freedom attached at the innermost gimbal link. In this section, the considerations which led to all aspects of this design are discussed. The drawings of each component are featured in Appendix A.

Link Configuration

The gimbal and scissor-type end effector are comprised of four links in series to result in the desired total 7 degrees-of-freedom. In an effort to reduce the system's mass, each of

the three gimbal links is only a quarter-circle, which keeps the rotational inertia as low as possible and also allows the user to more easily fit his or her hand into the system. Using a semicircle or full circle design for each link would have resulted in impeded motion for the user. However, the semicircle or full circle design does have the benefit of greater stiffness. In order for the gimbal to function properly, all axes of rotation must intersect at a single point. The three gimbal axes are non-collinear and offset from each preceding axis by 90°. The complete gimbal assembly is seen in Figure 2-3.

The scissor-type end effector link is designed so that the user grasps around the shaft of the final motor. This provides an intuitive method of controlling the gripper, which can be actuated by the user independently from the rotation of the gimbal links. This decoupling keeps the apparent inertia of the gripper low, and simplifies the control of the device.

The weight and stiffness of the final assembly motivate the choice of engineering plastics for the gimbal arms. Delrin Acetal Resin is a plastic known for its low weight and high stiffness. As such, each link is comprised of two ¼" Delrin sheets bolted together, as shown in the exploded views in Figures 2-5, 2-6, and 2-7. Keeping the links as short as possible benefits both the stiffness and the weight of the system. To further reduce the inertia of the robot, the links are hollowed in a truss-style pattern, which reduces mass by 20 – 33% over a solid link, depending on the particular link.

Delrin has a density of 1420 kg/m^3 and a yield strength of 75842330 Pa. In calculating the strength to weight ratio of delrin, the formula is given as

$$StrengthToWeight = \frac{\sigma_y}{\rho}$$

where σ_y is the yield strength and ρ is the density of the material. For delrin, this results in a strength-to-weight ratio of 53410 m^2/s^2. This is a very high value for a plastic material.

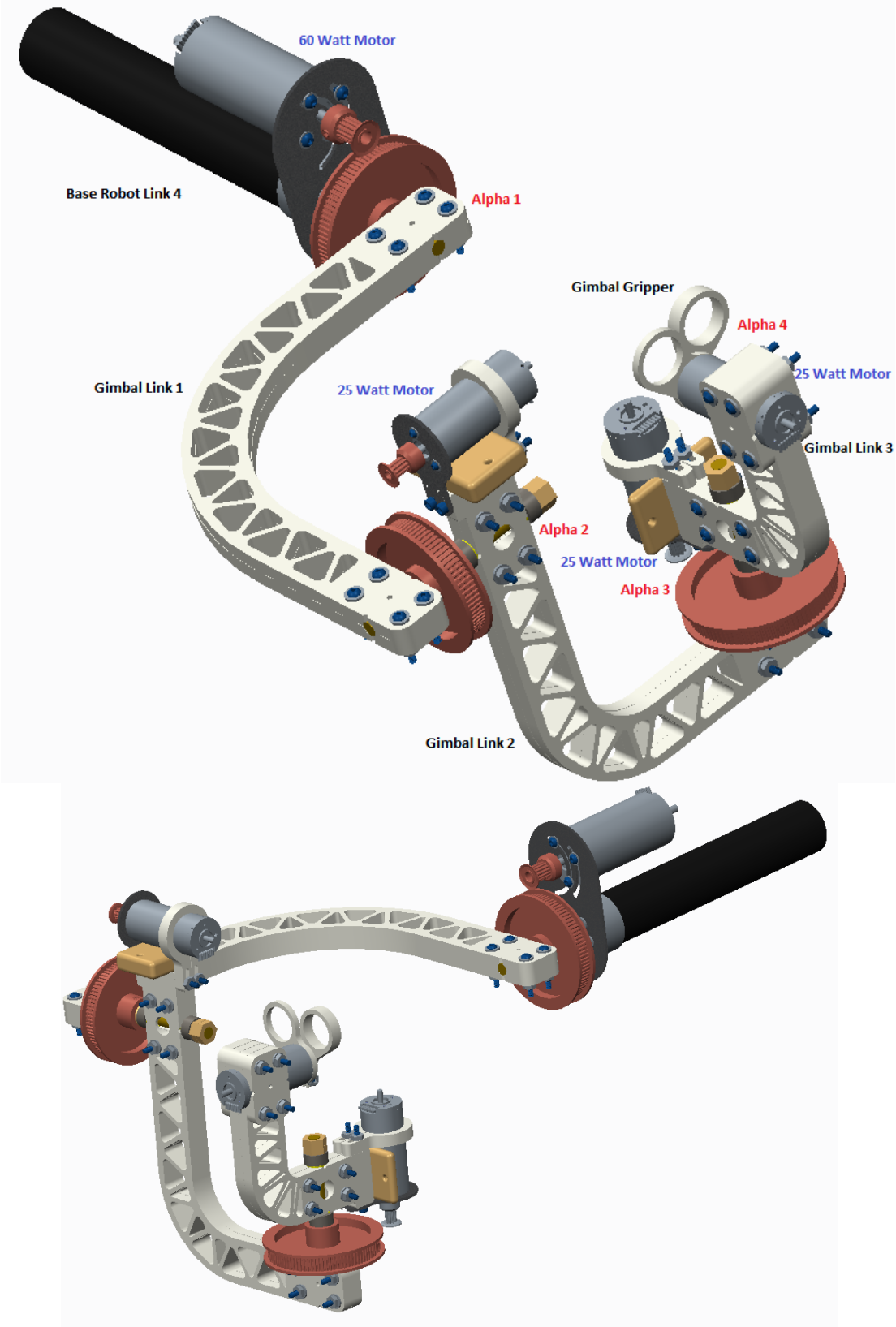

Figure 2-3: Complete gimbal assembly

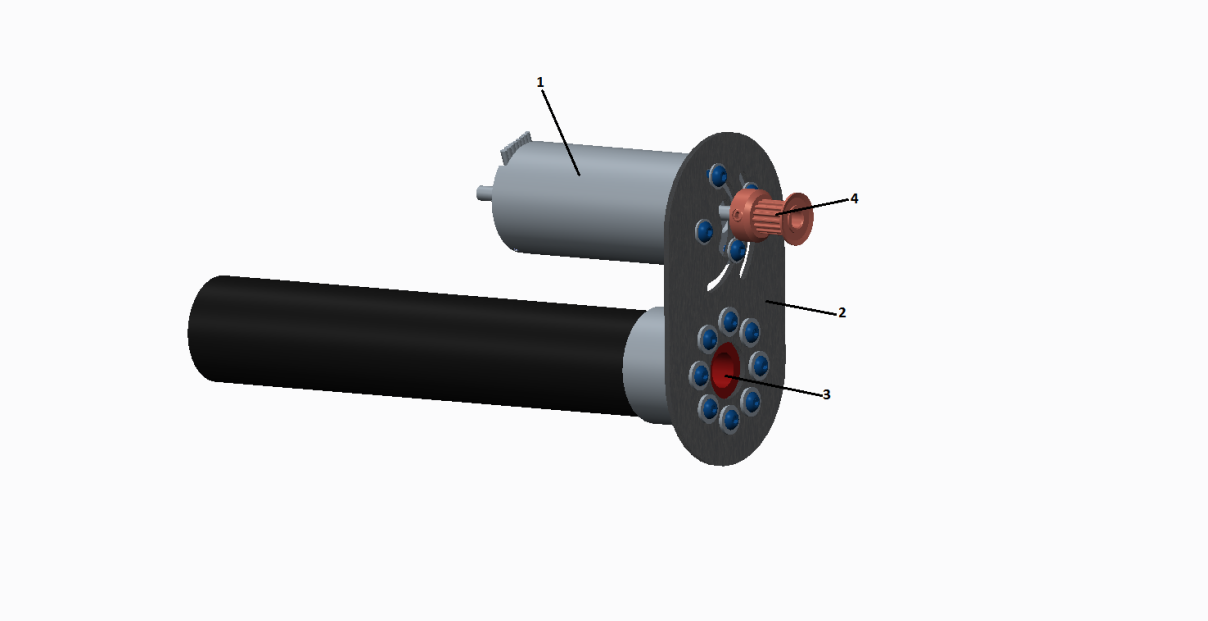

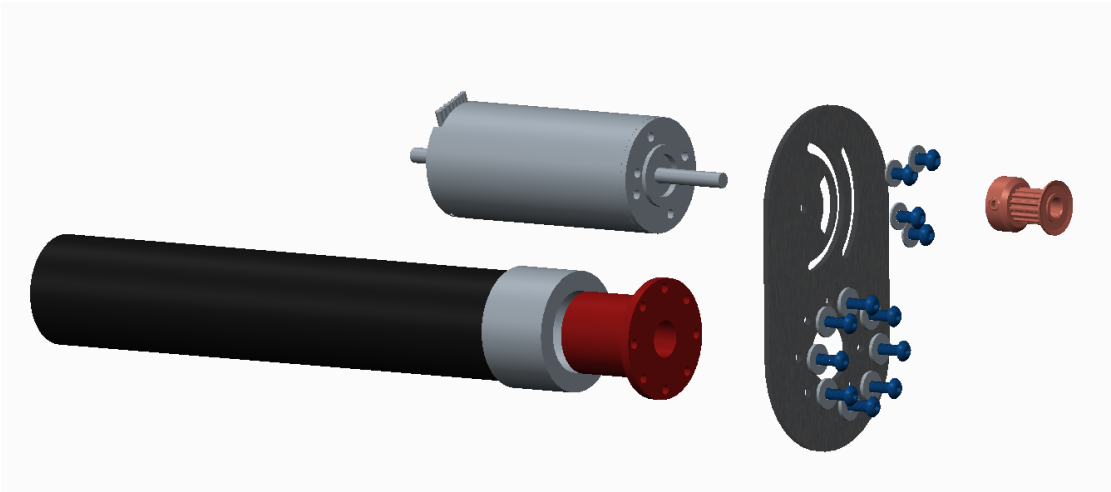

Figure 2-4: Base robot link 4 with exploded view. Technical drawings for labeled components are provided in Appendix A.

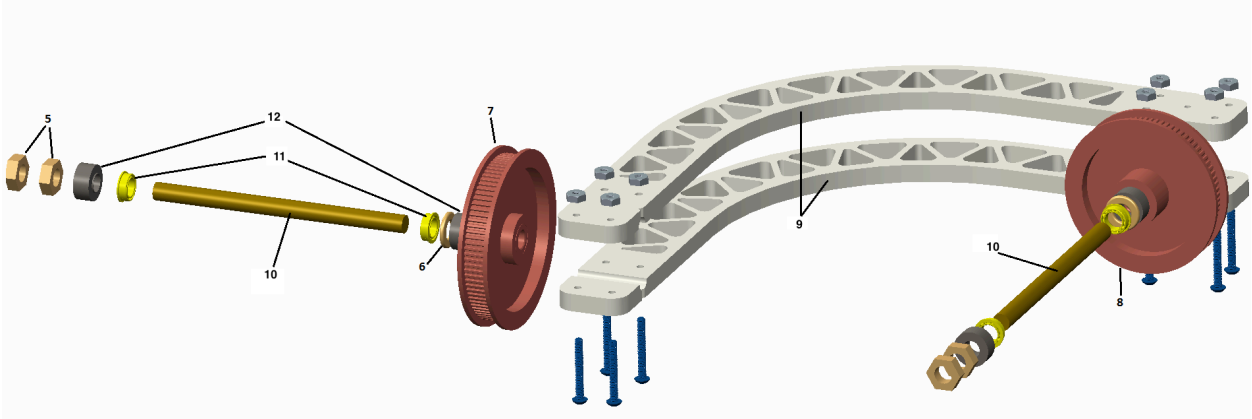

Figure 2-5: Link 1 with exploded view. Technical drawings for labeled components are provided in Appendix A.

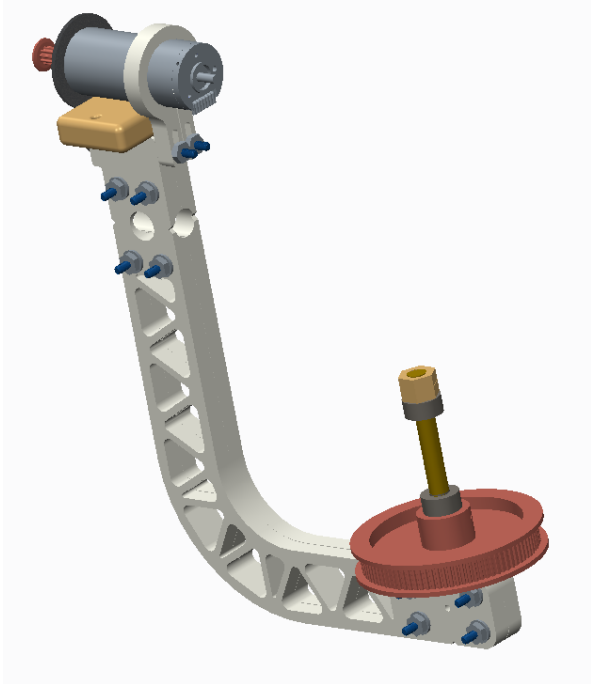

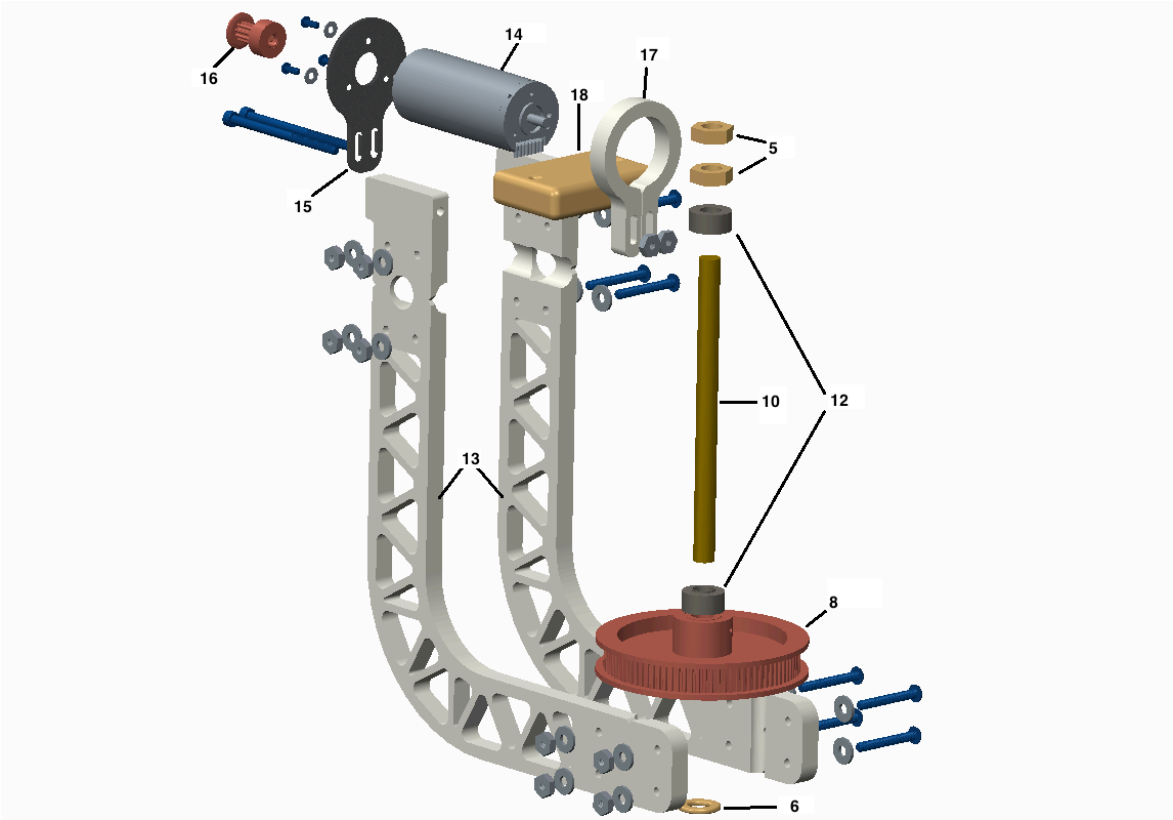

Figure 2-6: Link 2 with exploded view. Technical drawings for labeled components are provided in Appendix A.

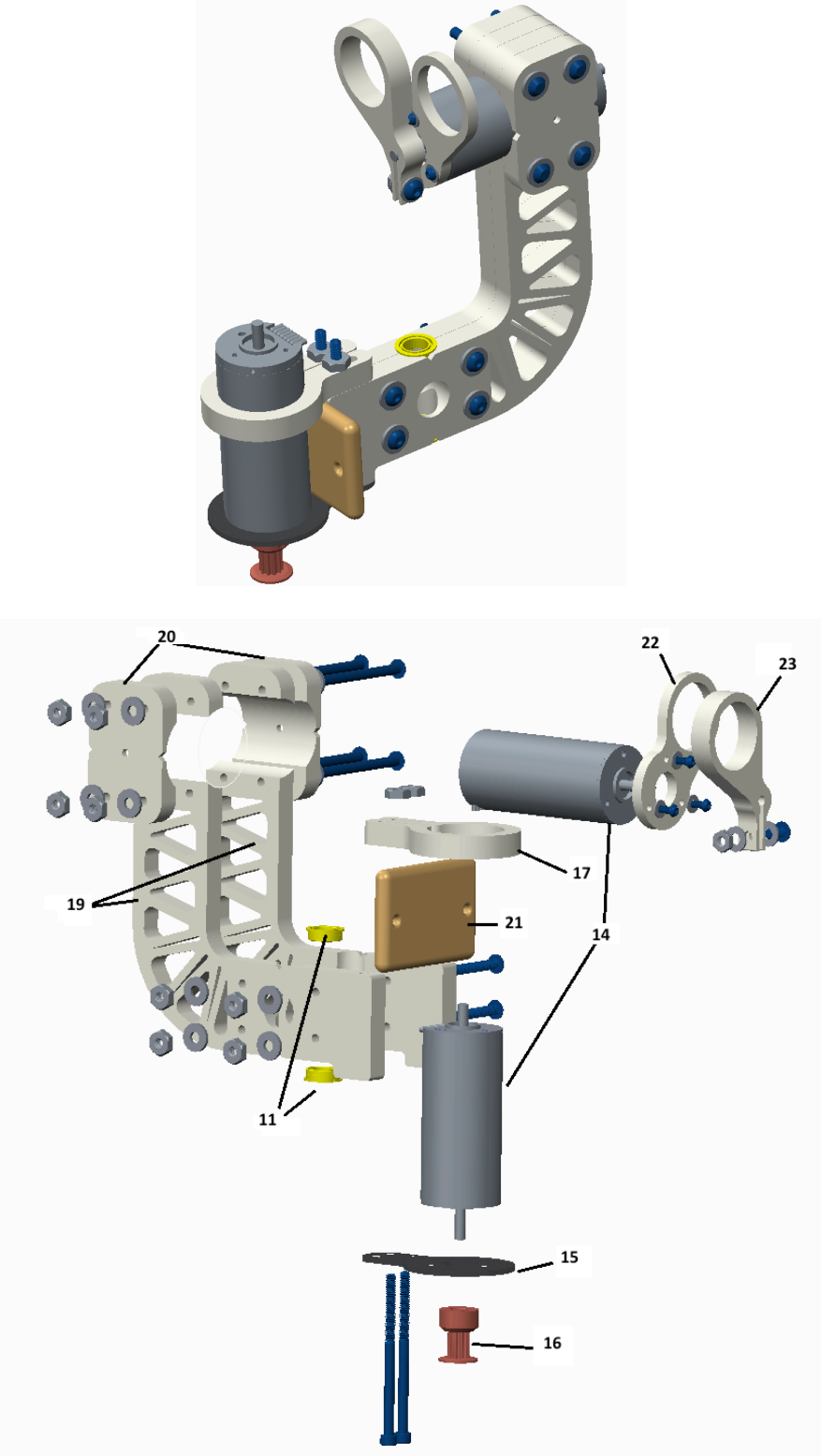

Figure 2-7: Link 3 with exploded view. Technical drawings for labeled components are provided in Appendix A.

Force Transmission

A common approach for reducing apparent inertia of kinematic mechanisms is to keep all of the motors near the base of the mechanism. For parallel kinematic structures, this approach is straightforward, but for serial mechanisms like a gimbal, placing the actuators at the base introduces the problem of transmitting torques to each subsequent joint. Transmission of the motor torques can be accomplished with cables and pulleys, but complicated three-dimensional cable routing is difficult to assemble and maintain, and also introduces unwanted friction. Thus, each motor is placed directly at the joint it actuates. This allows a simple, low friction, gear or timing belt system to drive each joint. To allow for manufacturing and assembly tolerances, an adjustable-tension timing belt system connects the motors to the links. The distance between each motor and corresponding link rotation axis is adjustable to appropriately set the tension of the timing belt. This distance is very minimal such that it does not strongly impact the static balance of the system. All calculations were made with the motors in their final positions. For example, in Figure 2-6, items 14, 15, 16, and 17 can move in unison along the length of the link. The belt wrapped around item 15 and item 8 in Figure 2-5 becomes tensioned, at which point, the wedge pictured as item 18 can be placed between link 2 and the motor to prevent the tension from being released.

Other considerations with regard to torque transmission are friction, backlash, backdrivability, and the additional weight caused by the motors. To achieve minimal backlash, the axles chosen were of very low tolerances. As such, the axles were tightly held by the bearings. The bearing bores are reamed to the outer diameter of the bearing races. Two bearings separated by at least 1 inch support each link mounted to its respective axle, providing stability to the joint. The bearings used in the system all earned the ABEC-5 precision certification, and

are open style bearings to minimize friction. Of the available bearings for the robot given the dimensional constraints, the ABEC-5 bearings had a higher dynamic load capacity than the ABEC-7 bearings. This is significant because the bearings have a radially applied load from the timing belt's tension. The ABEC-5 bearings have a radial load capacity of 84 pounds vs. 38 pounds for the ABEC-7 bearings. The open bearings are well-covered by other components to help prevent dirt from entering the inner races.

A haptic robot must be easily backdrivable as to prevent the user from feeling any unnecessary inertia in the system. Unfortunately, the motors used in the robot were not powerful enough to allow for a 1:1 gear ratio between the motors and each link's axle without the use of additional torque. This difficulty arises from a need to keep motor weight low. Motors powerful enough to maintain a 1:1 transmission would have been excessively heavy. Thus, a 6:1 gear ratio is used for the motor controlling link 1 while an 8:1 gear ratio is applied to the motor controlling links 2 and 3. This means that the user feels additional inertia to that of the links and the motor from the gear ratios.

The magnitude of this reflected inertia was found by multiplying the rotor inertia value given on the motor's specification sheet by the square of the gear ratio. The equation for the total inertia for a given link is

$$J_t = J_r N^2 + J_l$$

where J_t is the total inertia, J_r is the rotor inertia provided on the specification sheet, N is the gear ratio, and J_l is the inertia of the remaining components that make up the link.

For the motor controlling link 1, a Maxon 272765 brushless motor, the given rotor inertia is 21.9 g-cm^2. With the 6:1 gear ratio, this becomes 788.4 g-cm^2. J_l for link 1 is 21948 g-cm^2. J_t without the 6:1 gear ratio is 21970 g-cm^2. J_t with the 6:1 gear ratio is 22736 g-cm^2. The reflected

inertia makes up <4% of the inertia felt in link 1. J_t with the 6:1 gear ratio is negligibly larger than J_t without the 6:1 gear ratio. Thus, the increased inertia would not dramatically impact the user's experience.

For links 2 and 3, Maxon 283858 brushless motors with rotor inertias of 4.45 g-cm^2 were used with 8:1 gear ratios. Thus, the reflected inertia of the rotor is 284.8 g-cm^2. For link 2, J_t without the gear ratio is 20781 g-cm^2 while J_t with the 8:1 gear ratio is 21062 g-cm^2. For link 3, J_t without the gear ratio is 8871 g-cm^2 while J_t with the 8:1 gear ratio is 9151.8 g-cm^2. The reflected inertias are a small compromise and make up a negligible part of the total system inertia felt by the user. The gear ratios allow the motors to stay within their continuous torque limits at all times.

Mounting the motors directly at the gimbal links does add to the J_l inertia term felt by the user. This added inertia is minimized by placing the motors as close to the axes of rotation as possible, decreasing the moment arm of the motor. For example, the motor controlling α_2 sits 5.28 cm away from the center of rotation. With a mass of 110 g, the motor contributes a moment of inertia of $J = mr^2 = 110 * 5.28^2 = 3066 gcm^2$. As the r term in this equation increases, the inertia increases quadratically. The motors are also positioned such that their mass provides partial static balancing to the system. Relative to each link's axis of rotation, the motor actuating each joint sits opposed to most of the mass of the link. As described in Chapters II and III, the remaining static balance correction for the gimbal is accomplished through a spring apparatus, software, and commanded as motor torques.

Motor Selection

The key for motor selection is power. Power is defined as $P = \omega \times \tau$ where ω is the motor's speed and τ is the motor's torque. The assumption was made that for a haptic robot such as this gimbal, the motor's speed will remain quite low (<60 rpm). The torque is much more critical in order for the user to feel the desired forces. For the purposes of keeping inertia low, the second priority for the motors was a high torque-to-weight ratio. Because of the disparity in significance between torque and speed, choosing motors became focused on finding motors with enough torque to compensate handle the inertias of each link while remaining lightweight. Once motors were selected, the power demanded by each motor was examined to ensure the values were within reasonable limits. The motor chosen to manipulate the first link is a Maxon 272765 brushless 60 Watt DC motor with a peak torque of 519 mNm and a weight of 305 grams. A Maxon 283858 brushless 25 Watt DC motor with a peak torque of 121 mNm and a weight of 110 grams actuates each subsequent link and the gripper. A larger motor was chosen to manipulate the base link because of the increased inertial load felt on that link. Additionally, the 60 Watt motor is mounted to Link 4 of the original haptic robot, thus, it does not affect the inertia of the gimbal. These motors provide sufficient torque to achieve 5% of human average maximum wrist torque of 18 N listed in the design specifications. However, these torques were between the continuous torque limits and the stall torques. Thus, the previously described transmissions were applied in the form of timing belts. The data sheets for these motors are included in Appendix A.

Position Sensing and Force Commands

The motors use built-in magnetic incremental encoders to determine the position of the joints. This position is used to calculate the robot Jacobian matrix as described in the next

section. Through the Jacobian matrix, the required force is converted to required joint torques. Since the design includes very few sources of friction, commanded forces may be produced open-loop by computing the required motor currents, where for each motor the torque-current relationship is given by

$$\tau = k_{tj} i$$
$$j = 1,...,7$$

where τ is the motor torque, k is the torque constant, and i is the current.

CHAPTER III

KINEMATIC ANALYSIS AND CONTROLS

Introduction

The kinematic analysis of the system includes determining the forward kinematics, the Spatial Jacobian, the Body Jacobian, and the gravity terms of the system dynamics.

Forward Kinematics

The forward kinematics were determined through the application of screw theory. The initial starting configuration of the robot was chosen by manipulating the system without any forces from the motors. The configuration that felt most natural was established as the starting position, and this home orientation is featured in Figure 2-3. Coordinate frames were assigned such that the z-axis is the axis of rotation for each joint. Positive angle values were assigned arbitrarily for joint rotation. Only the first 6 active links of the robot were addressed in the forward kinematics. The final link, the gripper, will be addressed individually as its purpose is unique to the system.

The forward kinematics can be obtained through the application of the product of exponentials formula, which relates each configuration of the robot to its starting configuration as

$$g_i(\theta_1,...,\theta_n) = e^{\hat{\xi}_1\theta_1}...e^{\hat{\xi}_n\theta_n}g_i(0),$$

Where $g_i(0)$ is the homogeneous transformation matrix corresponding to the reference configuration of link i, $g_i(\theta_1,...,\theta_n)$ is the configuration of link i corresponding to the joint

angles θ_1 through θ_n, and the exponentials are matrix exponentials of the joint twists $\hat{\xi}_1$ through $\hat{\xi}_n$ multiplied by the joint angles.

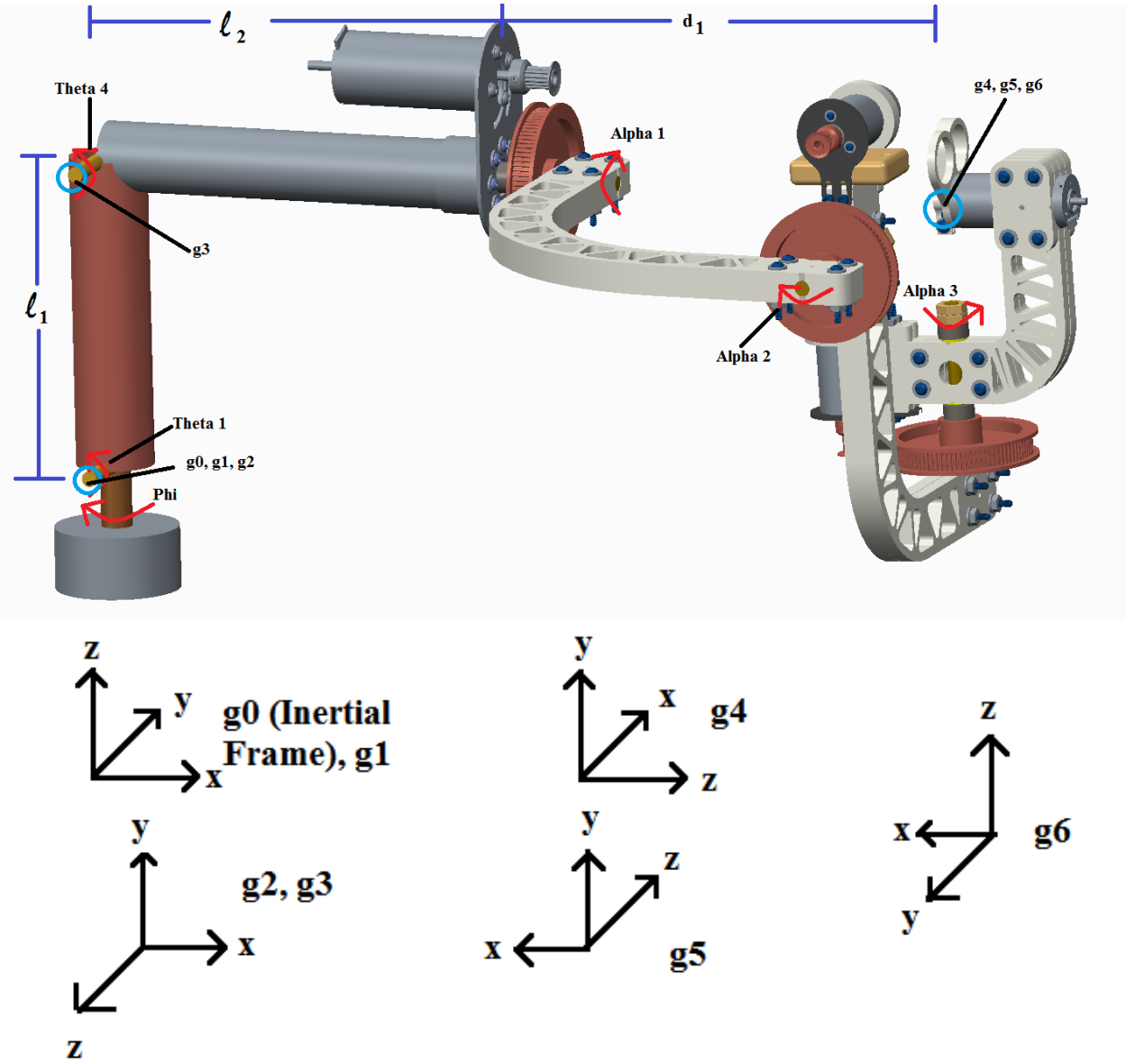

Figure 3-1: Diagram featuring joint angle assignments, distance variables, and coordinate frame orientations

The joint twists are given as follows

$$\xi_1 = \begin{bmatrix} 0 \\ 0 \\ 0 \\ 0 \\ 0 \\ 1 \end{bmatrix}, \xi_2 = \begin{bmatrix} 0 \\ 0 \\ 0 \\ 0 \\ -1 \\ 0 \end{bmatrix}, \xi_3 = \begin{bmatrix} .178 \\ 0 \\ 0 \\ 0 \\ -1 \\ 0 \end{bmatrix}, \xi_4 = \begin{bmatrix} 0 \\ -.2072 \\ 0 \\ -1 \\ 0 \\ 0 \end{bmatrix}, \xi_5 = \begin{bmatrix} -.2072 \\ 0 \\ .356 \\ 0 \\ 1 \\ 0 \end{bmatrix}, \xi_6 = \begin{bmatrix} 0 \\ -.356 \\ 0 \\ 0 \\ 0 \\ 1 \end{bmatrix}$$

Body Jacobian and Spatial Jacobian

The Jacobian matrix is formulated column-wise, and in the case of the Body Jacobian is given by

$$J_{st}^{b}(\theta) = [\,\xi_1^T, \ldots, \xi_{n-1}^T, \xi_n^T\,]$$

$$\xi_i^T = Ad_{(e^{\hat{\xi}_i\theta_i} \ldots e^{\hat{\xi}_n\theta_n} g_{st}(0))^{-1}} \xi_I$$

$$\xi_i = \begin{bmatrix} v_i \\ \omega_i \end{bmatrix} = \begin{bmatrix} -\omega_i \times q_i(0) \\ \omega_i \end{bmatrix}$$

$$\hat{\xi}_i = \begin{bmatrix} [\omega_i]_\times, v_i \\ 0 \quad 0 \quad 0 \quad 0 \end{bmatrix}$$

$$[\omega_i]_\times = \begin{bmatrix} 0 & -\omega_{iz} & \omega_{iy} \\ \omega_{iz} & 0 & -\omega_{ix} \\ -\omega_{iy} & \omega_{ix} & 0 \end{bmatrix}$$

The columns of the Body Jacobian are joint twists written with respect to the end effector frame [24]. The Spatial Jacobian is given by

$$J_{st}^{s}(\theta) = [\,\xi_1, \xi_2', \ldots, \xi_n'\,]$$

$$\xi_i' = Ad_{(e^{\hat{\xi}_1\theta_1} \ldots e^{\hat{\xi}_{i-1}\theta_{i-1}})} \xi_i$$

For serial robots, the Jacobian matrix of the robot relates the end effector velocity to the joint velocities, as given by the equation

$$J\dot{q} = \dot{x},$$

where $\dot{q}$ represents the joint angle velocities, $\dot{x}$ is the rigid body velocity of the end effector, and J is the Jacobian matrix. The Jacobian can be determined by analyzing the twists of each joint. This was done for both the Spatial and the Body Jacobian. The code that generated these Jacobian matrices is found in Appendix C.

The Jacobian matrix also provides the static force mapping between end effector forces and joint torques for serial robots. This relationship is given by

$$\tau = J^T F,$$

where F is the force applied at the end effector and τ is the vector of joint torques. This relationship is used by control software to translate the desired force and torque at the end effector to the appropriate joint torques.

Equivalent Serial Robot

The parallelogram structure of the 3 degree-of-freedom base robot has an equivalent serial kinematic formulation. This allows the static force mapping of the previous section to be used to compute the joint torques of an equivalent serial robot, which are then converted to the torques to be applied to the parallel mechanism. The parallelogram manipulator shown in Figure 3-2 can be actuated either by joint torques acting along the coordinates θ_1 and θ_2, as a parallel robot, or by joint torques acting along the coordinates θ_1 and θ_4, as a serial robot. Joint torques computed for the serial structure are converted to torques for the parallel structure as follows.

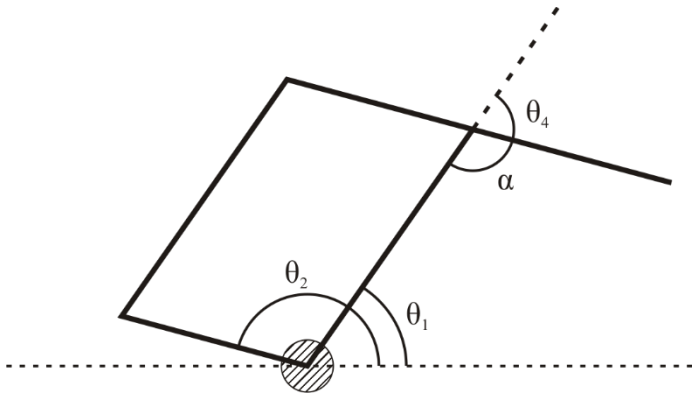

Figure 3-2: Parallelogram representation of the original haptic system

The parallelogram property implies that α (positive as drawn) is equal to

$$\alpha = \theta_2 - \theta_1$$

Since θ_4 (negative as drawn) and α (positive as drawn) are complementary angles,

$$-\theta_4 + \alpha = \pi$$

Solving for θ_4, we find that

$$\theta_4 = \theta_2 - \theta_1 - \pi$$

The virtual work of a virtual displacement along the angles θ_1 and θ_2 is given by

$$\delta W = \tau_1 \delta\theta_1 + \tau_2 \delta\theta_2$$

In the serial robot formulation, the motors would act along θ_1 and θ_4, giving the virtual work

$$\delta W = \bar{\tau}_1 \delta\theta_1 + \bar{\tau}_2 \delta\theta_4$$

Assume that $\bar{\tau}_1$ and $\bar{\tau}_2$ are known. By equating the virtual work, we find the required motor torques τ_1 and τ_2 in the parallel structure:

$$\tau_1 \delta\theta_1 + \tau \delta\theta_2 = \bar{\tau}_1 \delta\theta_1 + \bar{\tau} \delta\theta_4$$

By the constraint equation defining θ_4 above, we have

$$\delta\theta_4 = \delta\theta_2 - \delta\theta_1$$

$$\Rightarrow \tau_1\delta\theta_1 + \tau_2\delta\theta_2 = \bar{\tau}_1\delta\theta_1 + \bar{\tau}_2(\delta\theta_2 - \delta\theta_1)$$
$$\Rightarrow \tau_1\delta\theta_1 + \tau_2\delta\theta_2 = (\bar{\tau}_1 - \bar{\tau}_2)\delta\theta_1 + \bar{\tau}_2\delta\theta_2$$

Since the variations are arbitrary, the torques must be related by

$$\begin{aligned} \tau_1 &= \bar{\tau}_1 - \bar{\tau}_2 \\ \tau_2 &= \bar{\tau}_2 \end{aligned},$$

which completes the description of how the equivalent serial robot torques are converted to the parallel robot torques.

Gravity Compensation

The gimbal added significant weight to the original haptic system. In order to ensure that the design requirement for static weight is met, the motors of the base robot can be used to compensate for this added mass. To control the motors for such compensation, the gravity matrix for the system must to be calculated. To solve for this matrix, the gravitational potential energy for the robot is determined, and then differentiated with respect to each degree of freedom six separate times: once for each motor, excluding the gripper.

The potential energy of each link of the robot can be used to find the static torques required at the motors to counteract the forces due to gravity. The height of the center of mass of each link is isolated from the forward kinematics and placed into a 6x1 matrix, h. The mass of each link is ordered as a 1x6 matrix, m. The gravitational potential energy of the robot is given as a scalar. The constant acceleration due to gravity, g, is 9.81 m/s^2.

$$V=mgh$$

The torque at each motor is given by differentiating V with respect to each of the angles. For joint 1, the torque is computed by

$$\tau_1 = \frac{\delta V}{\delta \theta_1} - \frac{\delta V}{\delta \theta_2}$$

due to the interpretation of θ_2 a serial joint in the kinematics.

Although the base robot was originally designed to be statically balanced, as stated in Chap. 1 [21], the inclusion of the gimbal imbalances the design. As previously noted, static balance is an important factor in creating a sense of realism for the user.

The torque calculations show that the motors for links 1 and 2 do not have a high enough continuous torque limit to compensate the weight of the gimbal in all positions. It was calculated that the link 1 joint would require, at most, a torque of 1.97 Nm and the link 2 joint would require 3.23 Nm simply to maintain static balance at all points. The motors operating these joints have a continuous torque of 1.39 Nm and a peak torque of 14.9 Nm. While the necessary torques are capable of being output by the motors, it is dangerous to operate the motors outside of the continuous torque limit for an extended amount of time. As such, an alternative solution is needed.

The most obvious method for adjusting the system to increase the motors' torques is to use a gear ratio. With high speed being unimportant to the device, this is a logical path to follow for solving the weight problem. However, attempting to compensate for the additional weight through applying a gear ratio would require significant modifications to the design of the original system. This is unnecessarily challenging when there is a viable alternative to balancing with the motors through the use of springs. Building a spring apparatus won't require redesigning the base robot. Attempting to place a gearhead on the motors of the three degree-of-freedom robot would call for a substantial overhaul of the system.

Spring compensation of the base robot is an ideal solution for static balancing, because springs add little mass but can counteract the gravity torques. The original system was designed to be very compact to keep the inertia and footprint low. The small size causes difficulties fitting springs to the robot, because real springs need a significant amount of space for extension and compression in order to remain linear and prevent permanent deformation of the springs. Fortunately, it is possible to add springs to the base robot without any significant modification to the original design. Following the methods of Herder in [23], as shown in Figure 3-3, both ends of a spring may be rotated about the joint axis the spring acts on without changing the stored energy. Utilizing this technique, a spring balancing apparatus becomes feasible.

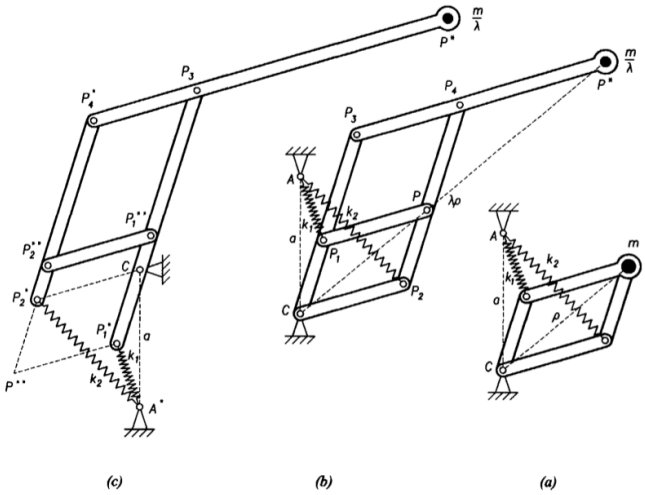

Figure 5.25 Conception of several two-degree-of-freedom equilibrators using the principle of superposition (from right to left): (a) combined balancing systems for two degrees-of-freedom according to figure 4.22, (b) extension using a pantograph linkage, (c) rotation of spring-lever elements.

Figure 3-3: Diagram from [23] which shows how the rotation of spring elements produces equal compensation.

The structure of the spring balancing mechanism for both links is shown in Figure 3-4. Because commercial off-the-shelf springs are sold only in discrete steps of length, stiffness, and diameter, an iterative process of spring choice and choice of the design parameters is required to find an approximate solution for static balancing. Although it should be theoretically possible to

achieve exact balance for a point mass held at the distal end of the base robot, the requirement that the springs have zero unstretched length cannot be met for joint θ_2 since real springs always have nonzero unstretched length. Since motor torques can be used to correct for minor errors in the spring balance, a solution which requires only motor torques within the continuous torque limit of the motors is acceptable.

Springs within the feasible ranges of diameter and length were tested in simulation to determine the final choice of spring. Feasible diameters were limited to ½" to allow for the springs to be added without making contact with surrounding components. Realistic spring lengths were limited to maximum extended lengths of 9". This value was chosen to maintain a small footprint. By discretizing the joint space of the robot, the maximum motor torques required for perfect balancing after the inclusion of the springs can be calculated for each spring. The spring found to produce the lowest required motor torques was selected as the balancing spring for each joint.

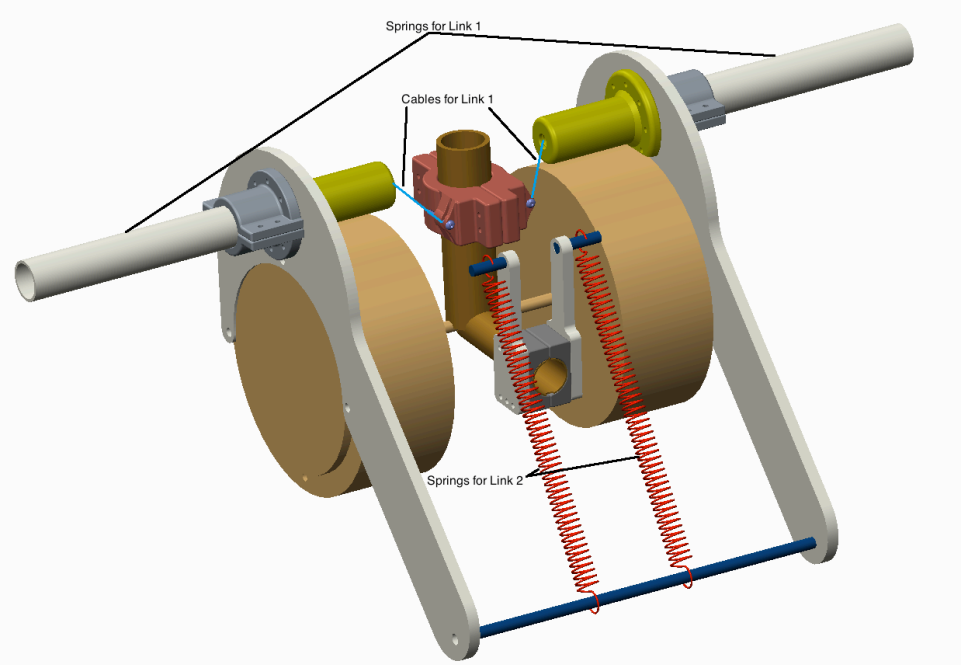

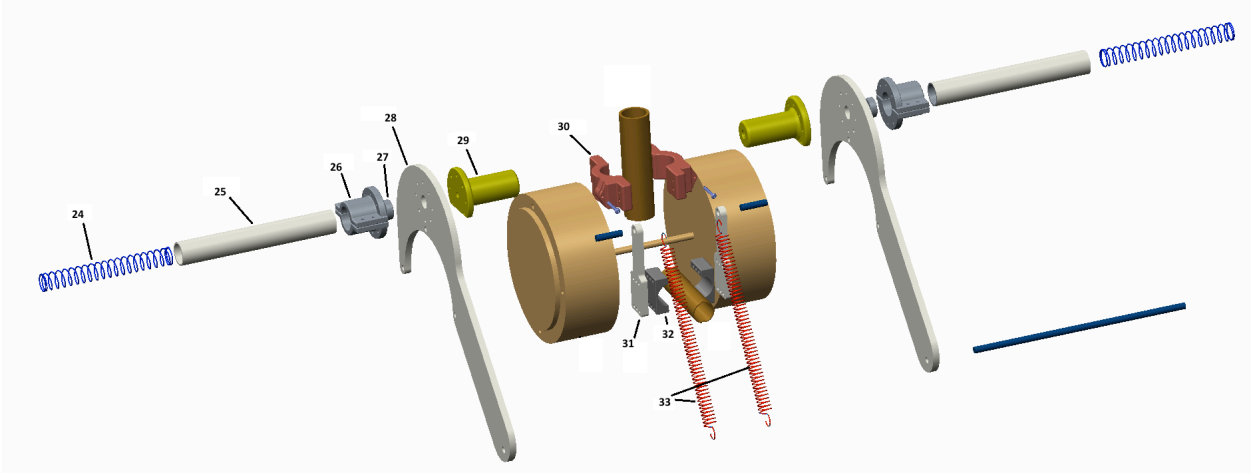

Figure 3-4: Gravity compensation apparatus with exploded view. Technical drawings for labeled components are provided in Appendix A.

3 DoF Robot - θ_2 Controlled Link (Link 2)

The first step is to determine the free length of the spring. This is different from the initial length given in the spring's specifications because the spring is under a load even at the initial length. Thus, its free length can be determined using Hooke's Law.

$$F_i = k(\ell_s - \ell_f)$$
$$\ell_f = \ell_s - \frac{F_i}{k}$$

Here, ℓ_f is the free length of the spring, ℓ_s is the initial length of the spring, k is the spring rate, and F_i is the initial load of the spring. From here, the extended length of the spring at any position of the robot can be determined using the Law of Cosines as follows.

$$\ell_e = \sqrt{d_1^2 + d_2^2 - 2d_1 d_2 \cos(\frac{\pi}{2} - \theta_1 - \theta_4)}$$

Here, ℓ_e is the extended length of the spring at a given orientation, d_1 is the distance from the center of rotation of one spring terminal, and d_2 is the distance from the center of rotation of the second spring terminal. The angle within the cosine function was determined by the placement of items 31 and 32 in Figure 3-4.

Using the equation for potential energy of a spring, the amount of energy added to the system through the spring apparatus is determined as follows.

$$E_2 = 2 * \frac{1}{2} k(\ell_e - \ell_f)^2$$

The spring energy is multiplied by 2 due to the 2 parallel springs acting on the system at all times. This energy was then added to the gravitational potential energy previously determined and is included in the differentiation that leads to the necessary motor torque.

The spring chosen, which produces the lowest required motor torque within the feasible range of spring choices and mechanism designs, has the following specifications.

$$k = .8\frac{lb}{inch} = 140.2\frac{N}{m}$$
$$\ell_s = 3inches = .0762m$$
$$F_i = .5lb = 2.225N$$

The joint torque that is needed to statically balance link 2 will never exceed 37.9 N-cm. Since the continuous torques for these motors is 139 N-cm, the motors will always be well within the their accepted operational limits.

3 DoF Robot - θ_1 Controlled Link (Link 1)

To balance the torque on joint 1, a similar process was used. The ideal spring balancing mechanism would place a tension or compression spring directly above or below the rotational axis of link 1, but the existing robot design does not allow such a placement. By using compression springs and cables in place of tension springs, the springs can be placed to either side of link 1 and attached directly to the link, as shown in Figure 3-4.

The height offset between the center of the spring and its attachment point on link 1 calls for a projection between the eyelet and the attachment plane. The cable is connected to a washer that sits against the end of the spring. The other end of the spring sits against a Delrin plate that is mounted to the outside of the motors. The cable runs through the middle of the compression spring and through an eyelet that is slightly above the terminal on link 1. The cable must make a sharp turn around this eyelet so low friction ceramic eyelets were used. From here, trigonometry was used to determine the spring energy as follows.

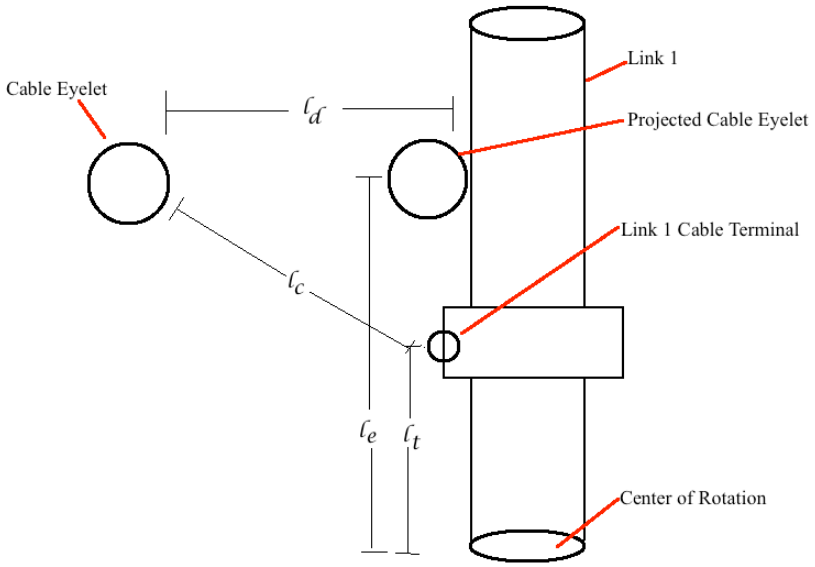

Figure 3-5: Cable routing diagram for Link 1 gravity compensation

The following steps describe the math to determine ℓ_c, featured in Figure 3-5. The first step was to determine the length between the eyelet, which is a fixed height, and the cable terminal on link 1. To do so, the eyelet height was projected onto the same plane as the cable terminal. The law of cosines could easily be applied using the eyelet height as one length of the triangle and the distance from the cable terminal on link 1 to the center of rotation as the other length.

$$\ell_p = \sqrt{\ell_e^2 + \ell_t^2 - 2\ell_e \ell_t \cos(\theta_1)}$$

Here, ℓ_p is the distance between the projected eyelet height and the cable terminal on link 1, ℓ_e is the projected eyelet height, and ℓ_t is the distance between the cable terminal and the center of rotation. From here, there is a right triangle formed using the distance from the eyelet to the plane on which it was previously projected as one leg and ℓ_p as the other leg. Applying Pythagorean's Theorem results in the final distance between the eyelet and the cable terminal at all points. This distance is calculated as follows.

$$\ell_c = \sqrt{\ell_p^2 + \ell_d^2}$$

Here, ℓ_d is the distance between the eyelet and the plane of the cable terminal and ℓ_c is the distance between the eyelet and the cable terminal. As with the gravity compensation for link 2, now the spring energy can be calculated easily for all orientations.

$$E_1 = 2 * \frac{1}{2} k \ell_c^2$$

Once again, two springs were used in parallel for this compensation meaning the energy is doubled. The springs ultimately chosen for this application have the following qualities.

$$k = 1.3 \frac{lb}{inch} = 227.8 \frac{N}{m}$$
$$\ell_u = 5 inches = .127 m$$

Here, ℓ_u represents the uncompressed length of the spring. E_1 and E_2 are then added to the V term previously defined. These are included in the subsequent differentiation for determining the joint torques necessary at every position. With the springs chosen, the maximum joint torque necessary to maintain any orientation at link 1 is .50 N-cm. As with link 2, the continuous torques for these motors is 139 N-cm, thus, the motors are always held within their operational constraints.

Electronics Package

Potentiometer Signal Conditioning

In order to operate the original 3 degree-of-freedom robot, readings from the high resolution potentiometers attached to each motor needed to be made. The voltage output by a potentiometer is linearly related to the angle by which the corresponding motor has turned. A

signal conditioning circuit was constructed to supply +5 Volts to each potentiometer while also amplifying the output signal to increase its resolution and reducing noise through filtering. After being processed by the circuit, the potentiometer signal was found to have noise <±2 mV; a value that corresponds to ~.4° of variance in the measurement of the joint angles. This circuit is an entirely new circuit that did not exist with the original robot at the start of this integration project. The circuit is detailed in Appendix B.

A significant issue with reading potentiometer signals is that of noise: both emitted from surrounding electronics and generated through ground loops. Careful consideration was taken in wiring the system to prevent any ground loops from being inadvertently constructed. The problem of emitted noise was addressed using shielded cable for all connections. The shields were all grounded to the earth. Low pass filters were used in the NI Analog Input box, as well. These steps were successful in reducing noise to the <±2 mV experienced.

Digital Encoder Readings

The digital encoders mounted on the motors of the gimbal are connected to the computers through a Contec CNT32-8M(PCI) card and in-house designed printed circuit board. The circuit boards are shown in Appendix B.

Servo Drives

The original base robot motors are driven by Advanced Motion Controls 25A8 PWM servo drives. These operate at a continuous current of 12.5 amps with a peak current of 25 amps. They are supplied 60 volts through a linear power supply.

The minimum inductance requirement of 200 μH for these amplifiers is not met by the Kollmorgen motors. External inductors of ~224 μH were built and put in series with the motors and the servoamps. The inductors consist of powder core toroids wound with 78 turns of a pair of 18 Ga magnet wires in parallel.

The gimbal motors use Advanced Motion Controls AZB12A8 PWM servo drives for operation. These amplifiers are rated for 6 amps of continuous current with a peak current of 12 amps. The 60 watt motor's servo drive is provided 48 volts from a switching power supply (Mean Well RSP-500-48). The 25 watt motors are powered from a 24 volt switching power supply (Mean Well SP-480-24).

Data Acquisition

All analog input and digital output connections between the servoamps and the computer are made through a National Instruments SCB-68 connector block and a National Instruments CB-68LPR connector block. The data acquisition card is a National Instruments M series 6229 PCI card. The details of these connections are listed in Table D1. The + Current Reference In and - Current Reference In pins on the servoamps are driven by a Measurement Computing PCI-DAC 6703 PCI analog output card.

Computer Controller

The controller for the haptic system was built in Matlab's Simulink RealTime. The controller approximates cancellation for the gravity terms of the robot to keep the system statically balanced through its entire use. The input is the angular position of each joint and the output is the torque required to compensate for the gravity in that orientation. This impendance

controller reduces the uncompensated weight to create transparency for the user. The software brings the uncompensated weight below 50 mN, as targeted in the design goals.

To demonstrate the force feedback capabilities of the system, a virtual haptic box was built in the controller. When the end effector is inside of the box, the only torque being applied by the motors is that of gravity compensation. When the end effector makes contact with the walls of the box, a spring-damper system is introduced to simulate the feeling of running into a real-world wall. The gimbal is still rotatable when the end effector is pressed against the wall; however, the translation motion is strongly restricted. The virtual spring has a spring constant of -1000 N/m, thus, generated a significant amount of force quickly. Images of the Simulink controller are featured in Appendix C.

Results and Conclusion

The haptic control successfully proved the robot's feedback abilities. Figure 3-6 shows the position of the end effector being consistently halted at the haptic box walls in all directions during a trial. Figure 3-7 shows how the torques of each motors reacted to impact with the haptic walls during that same trial.

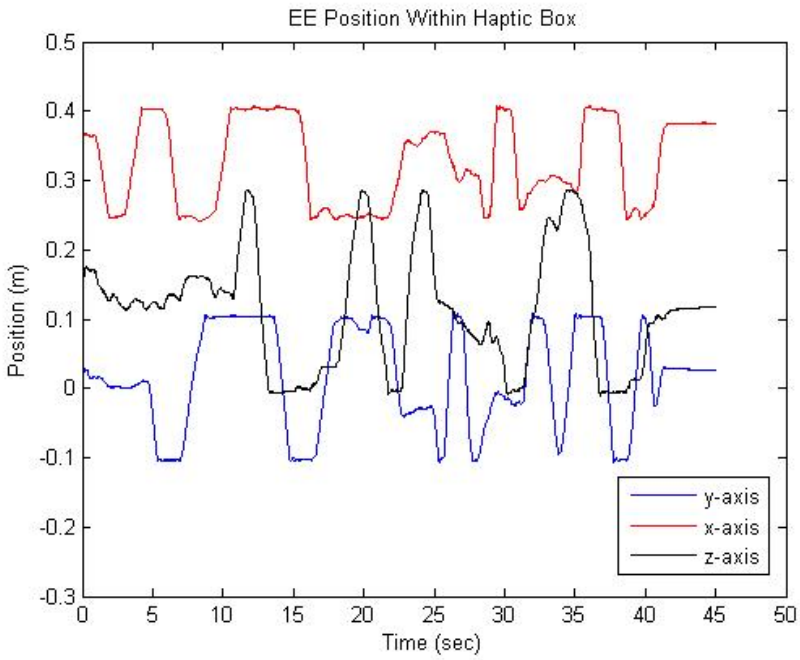

Figure 3-6: Position of the end effector within the haptic box

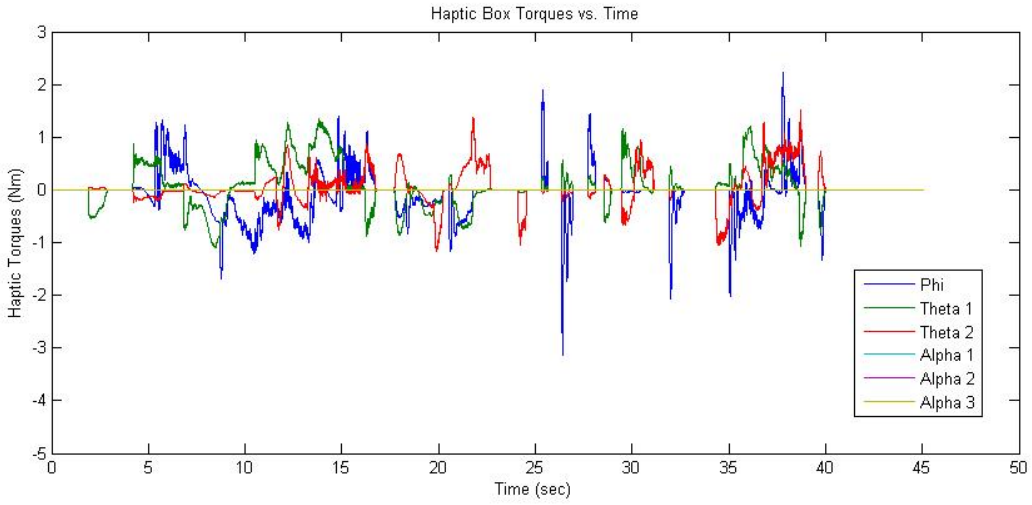

Figure 3-7: Haptic torques reacting to impact within the haptic box

The 7 degree-of-freedom haptic robot has achieved all of its design goals. The tool's characteristics fall within or exceed the expectations set by other commercially available systems. The result is a viable haptic interface for implementation into surgical robotics research.

The system can serve in a master-slave system effectively for many applications due to its large workspace and haptic feedback.

APPENDIX A

Appendix A consists of technical drawings and data sheets for all the components that comprise the gimbal and spring support system.

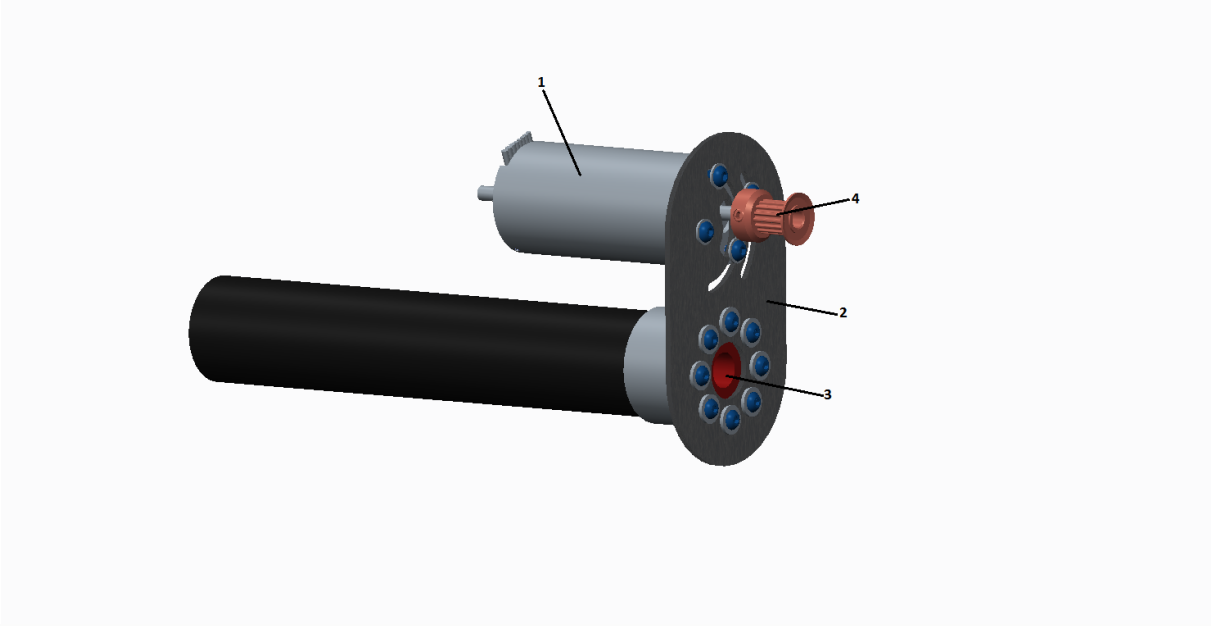
1
4
2
3

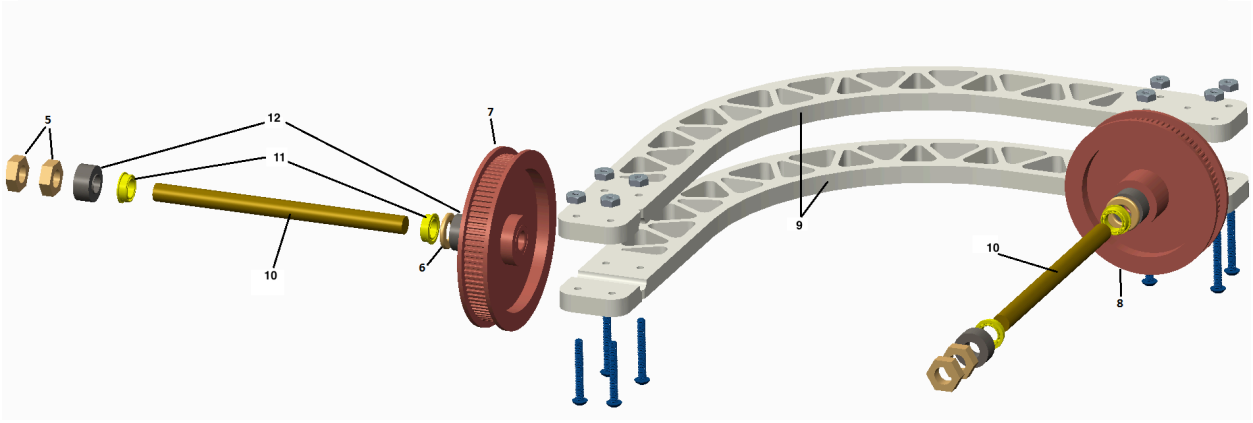
5
12
11
10
7
6
9
10
8

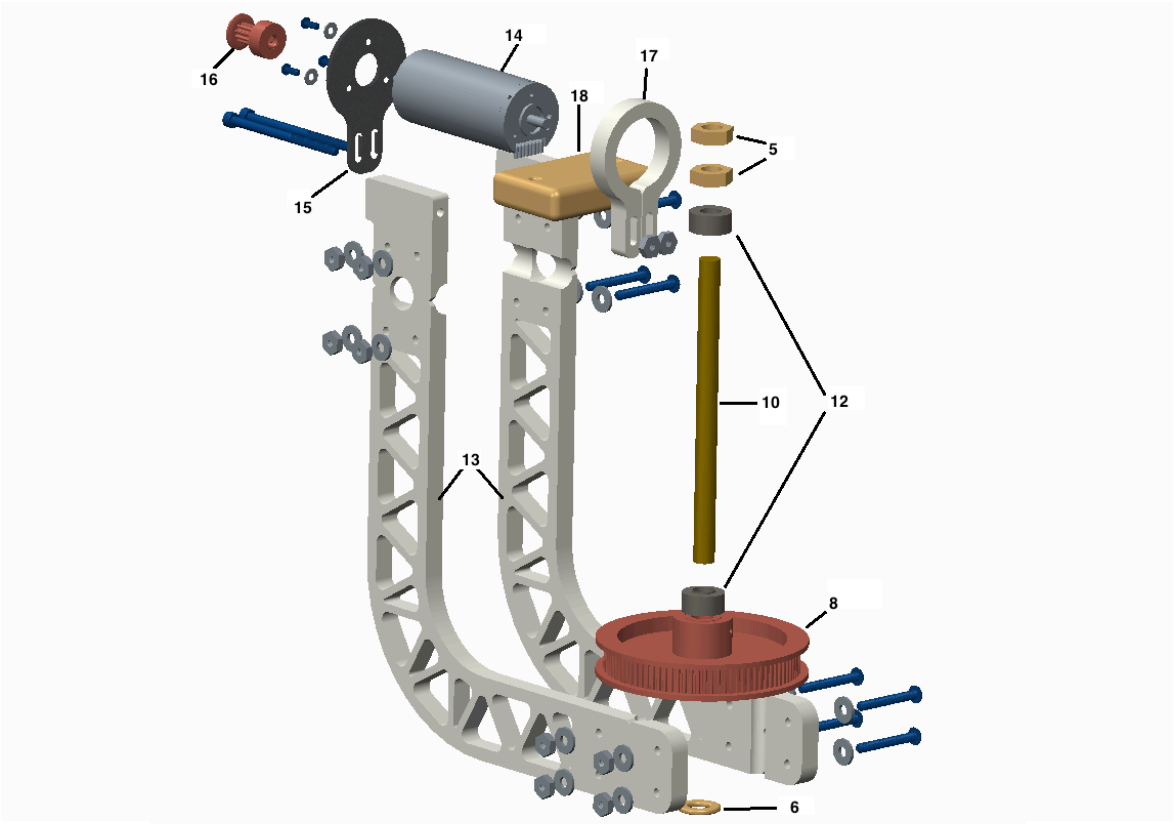
16
14
17
18
5
15
10
12
13
8
6

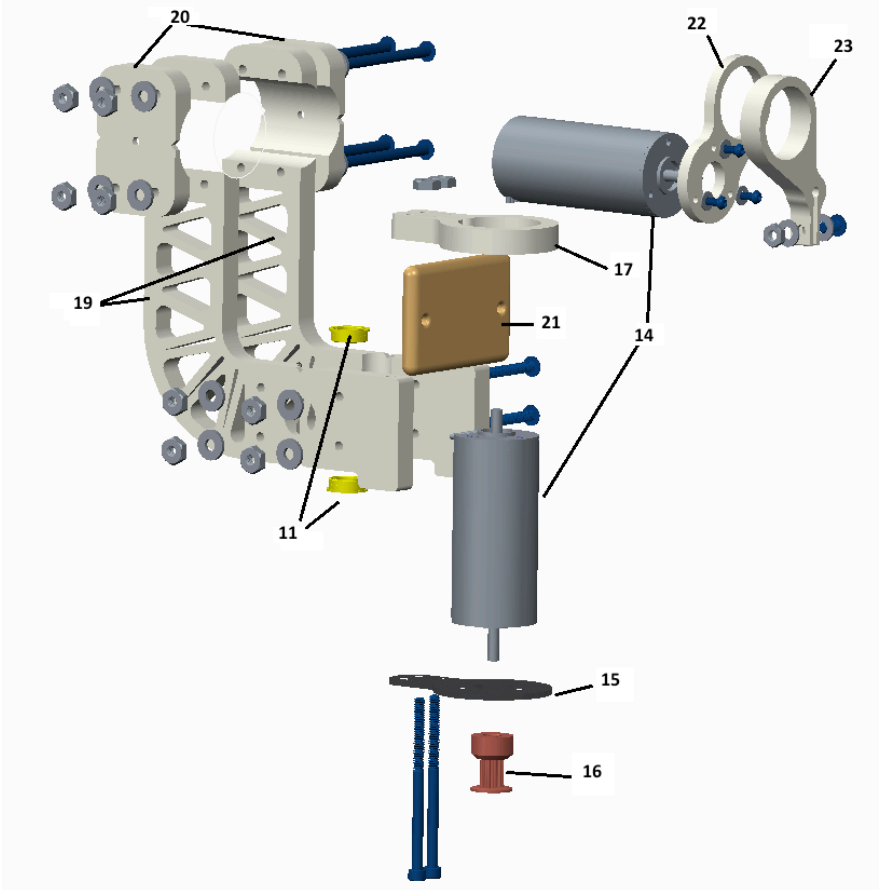
20
22
23
17
19
21
14
11
15
16

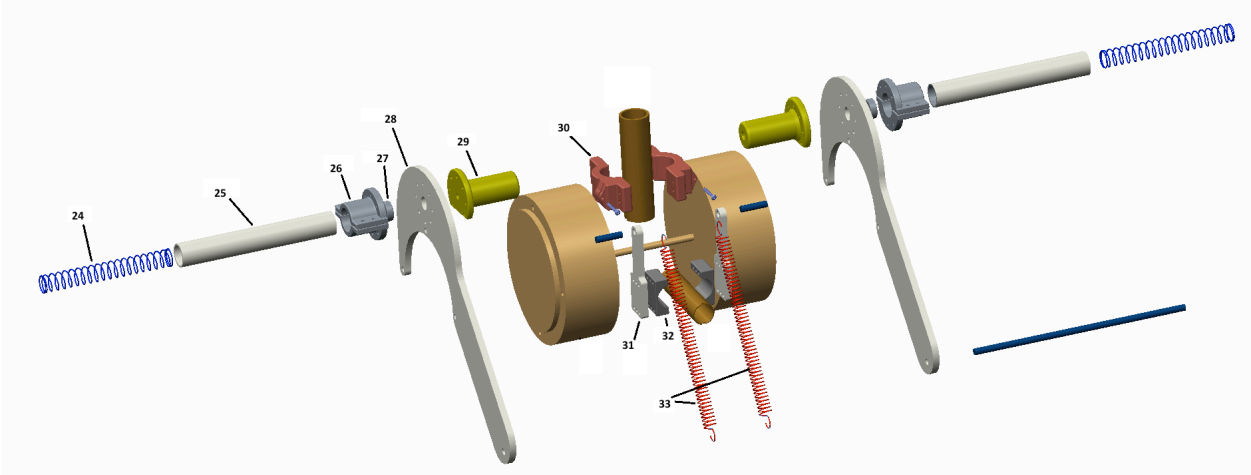
24
25
26
27
28
29
30
31
32
33

EC-max 30 ∅30 mm, brushless, 60 Watt

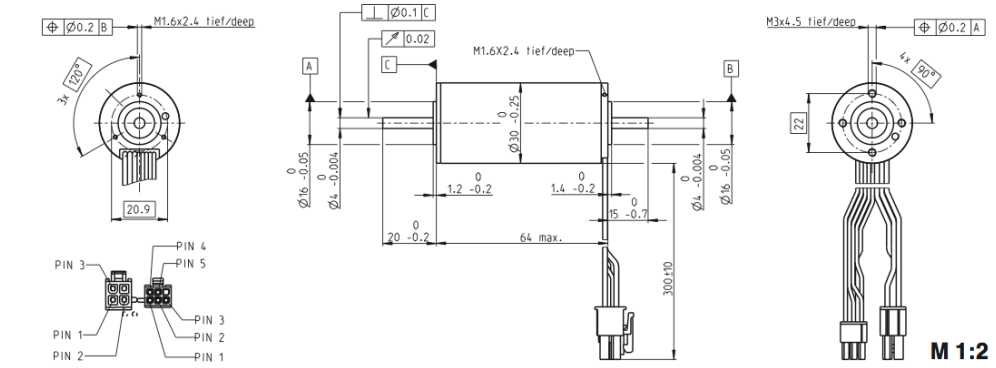

Stock program
Standard program
Special program (on request)

Motor Data		Part Numbers 272762	272763	272764	272765
Values at nominal voltage					
1 Nominal voltage	V	12	24	36	48
2 No load speed	rpm	7980	9340	9490	9350
3 No load current	mA	302	191	130	95.4
4 Nominal speed	rpm	6590	8040	8270	8130
5 Nominal torque (max. continuous torque)	mNm	63.6	60.7	63.7	64.1
6 Nominal current (max. continuous current)	A	4.72	2.66	1.88	1.4
7 Stall torque	mNm	381	458	522	519
8 Stall current	A	26.8	18.8	14.5	10.7
9 Max. efficiency	%	80	81	82	82
Characteristics					
10 Terminal resistance phase to phase	Ω	0.447	1.27	2.48	4.49
11 Terminal inductance phase to phase	mH	0.049	0.143	0.312	0.573
12 Torque constant	mNm/A	14.2	24.3	35.9	48.6
13 Speed constant	rpm/V	672	393	266	197
14 Speed/torque gradient	rpm/mNm	21.2	20.6	18.4	18.2
15 Mechanical time constant	ms	4.86	4.73	4.21	4.17
16 Rotor inertia	gcm²	21.9	21.9	21.9	21.9

Specifications

Thermal data

17	Thermal resistance housing-ambient	7.4 K/W
18	Thermal resistance winding-housing	0.5 K/W
19	Thermal time constant winding	2.76 s
20	Thermal time constant motor	1000 s
21	Ambient temperature	-40…+100°C
22	Max. winding temperature	+155°C

Mechanical data (preloaded ball bearings)

23	Max. speed		15000 rpm
24	Axial play at axial load	< 6.0 N	0 mm
		> 6.0 N	0.14 mm
25	Radial play		preloaded
26	Max. axial load (dynamic)		5 N
27	Max. force for press fits (static)		98 N
	(static, shaft supported)		1300 N
28	Max. radial load, 5 mm from flange		25 N

Other specifications

29	Number of pole pairs	1
30	Number of phases	3
31	Weight of motor	305 g

Values listed in the table are nominal.

Connection motor (Cable AWG 20)

red	Motor winding 1	Pin 1
black	Motor winding 2	Pin 2
white	Motor winding 3	Pin 3
	N.C.	Pin 4

Connector Molex **Part number** 39-01-2040

Connection sensors (Cable AWG 26)

yellow	Hall sensor 1	Pin 1
brown	Hall sensor 2	Pin 2
grey	Hall sensor 3	Pin 3
blue	GND	Pin 4
green	V_{Hall} 3…24 VDC	Pin 5
	N.C.	Pin 6

Connector Molex **Part number** 430-25-0600

Wiring diagram for Hall sensors see p. 33

Operating Range

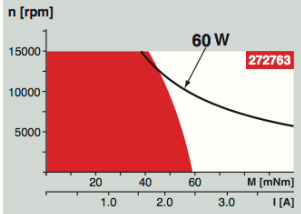

Comments

Continuous operation
In observation of above listed thermal resistance (lines 17 and 18) the maximum permissible winding temperature will be reached during continuous operation at 25°C ambient.
= Thermal limit.

Short term operation
The motor may be briefly overloaded (recurring).

Assigned power rating

maxon Modular System

Overview on page 20–25

Planetary Gearhead
Ø32 mm
1.0 - 8.0 Nm
Page 308/310

Koaxdrive
Ø32 mm
1.0 - 4.5 Nm
Page 312

Planetary Gearhead
Ø42 mm
3 - 15 Nm
Page 315

Recommended Electronics:

Notes	Page 24
ESCON 36/3 EC	379
ESCON Mod. 50/4 EC-S	379
ESCON Module 50/5	379
ESCON 50/5	380
DEC Module 50/5	382
EPOS2 Module 36/2	386
EPOS2 24/5, 50/5	387
EPOS2 P 24/5	390
EPOS3 70/10 EtherCAT	393
MAXPOS 50/5	396

Encoder MR
500/1000 CPT,
3 channels
Page 355

Encoder HEDL 5540
500 CPT,
3 channels
Page 366

Brake AB 20
24 VDC
0.1 Nm
Page 406

Figure A1: Item 1 – 30 mm DC Motor

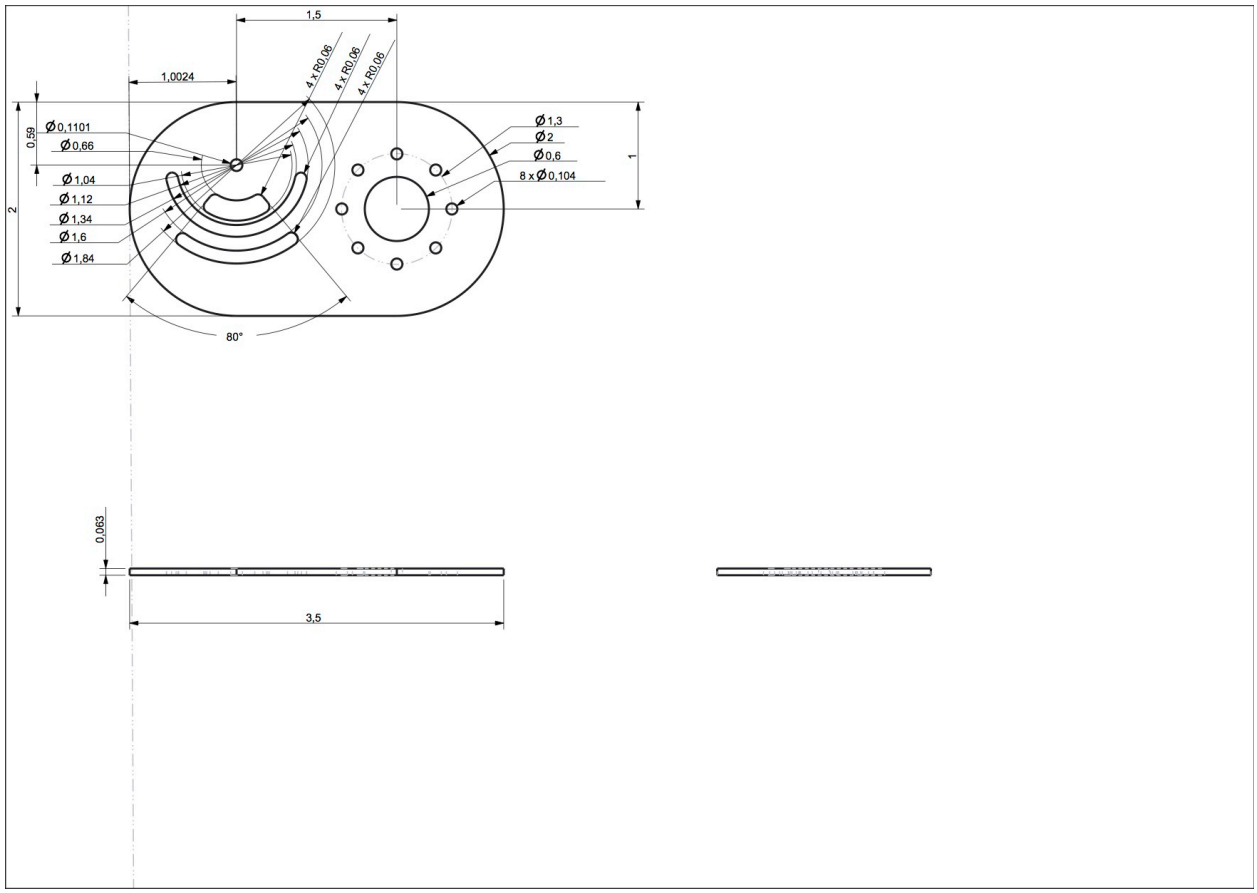

Figure A2: Item 2 – 30 mm Motor mount (all measurements in inches)

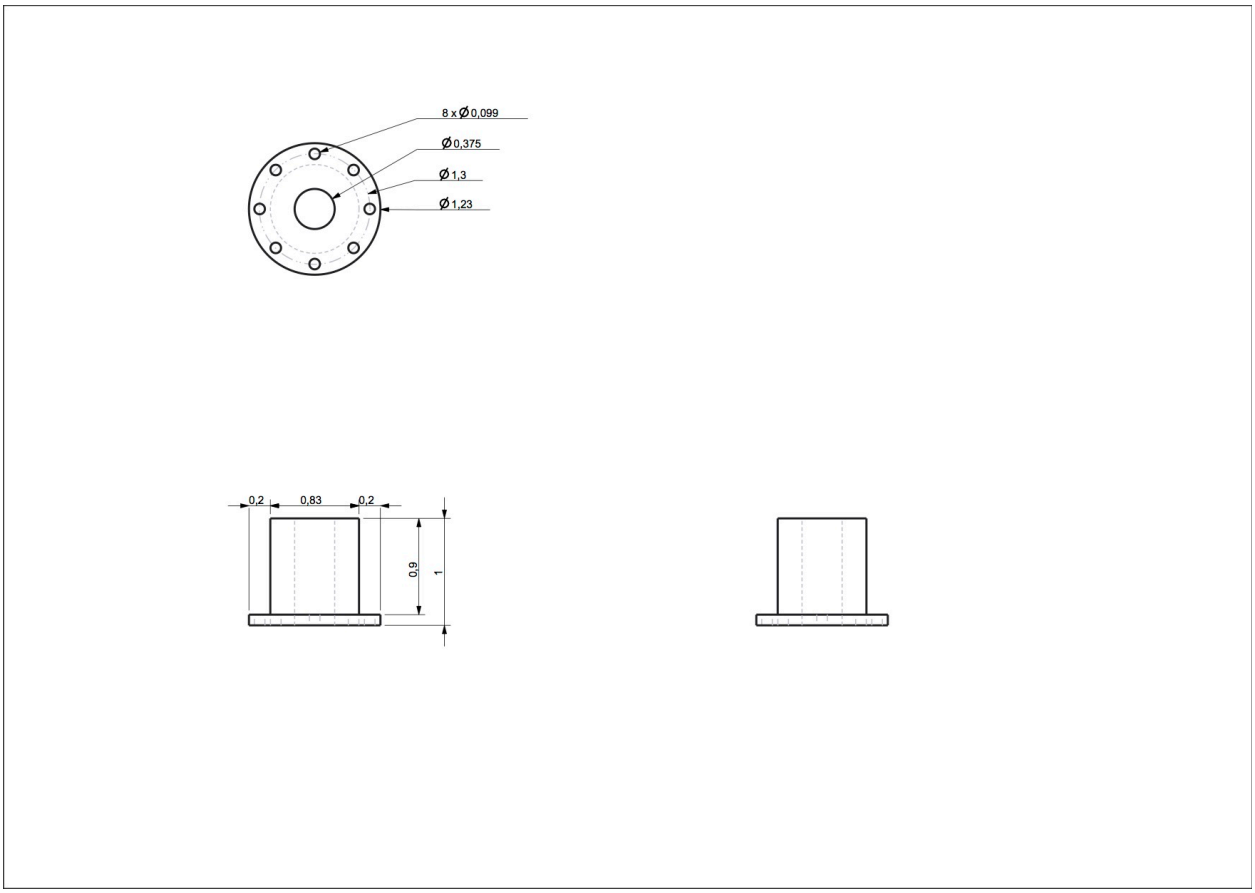

Figure A3: Item 3 – Aluminum mount link (all measurements in inches)

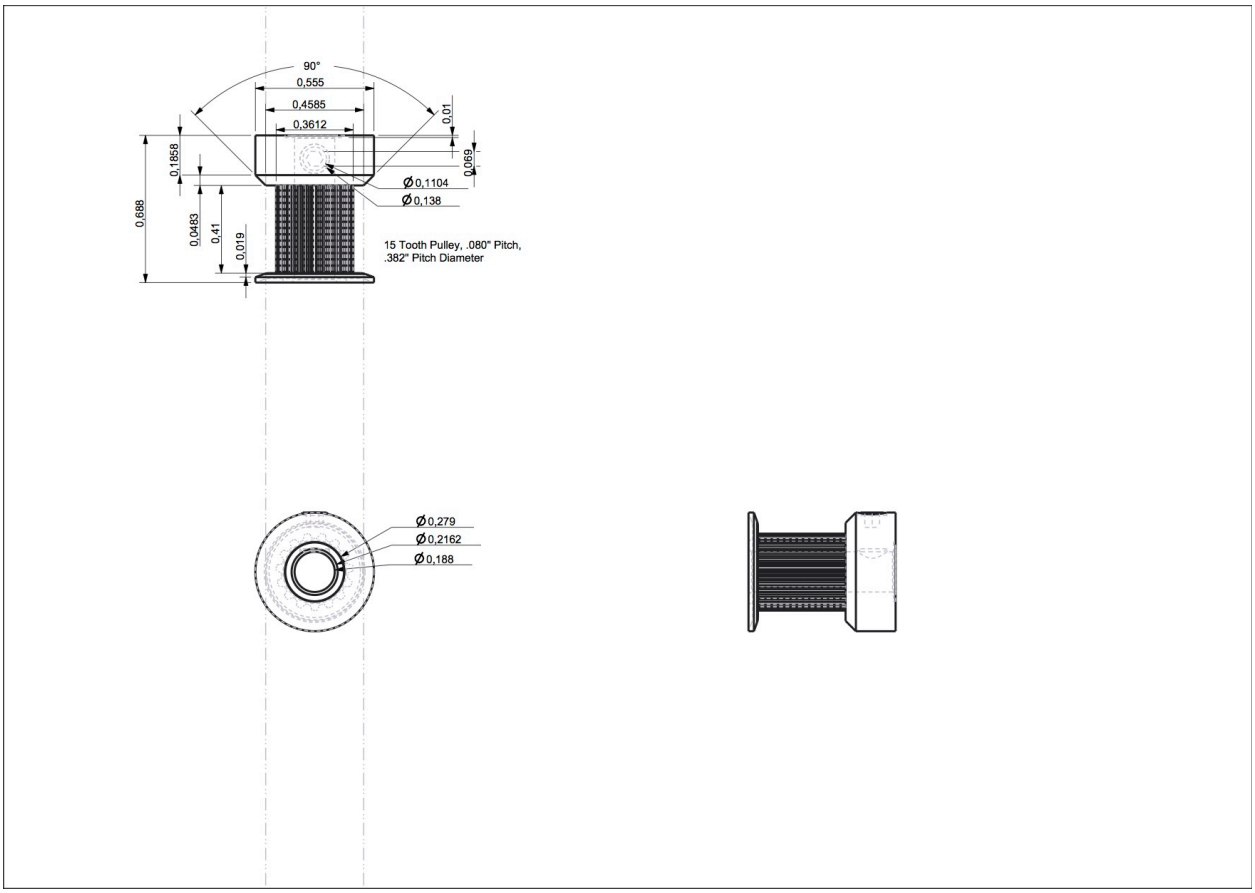

Figure A4: Item 4 – 15 tooth timing belt (SDP-SI Part # A 6N16-015DF1206) (All measurements in inches)

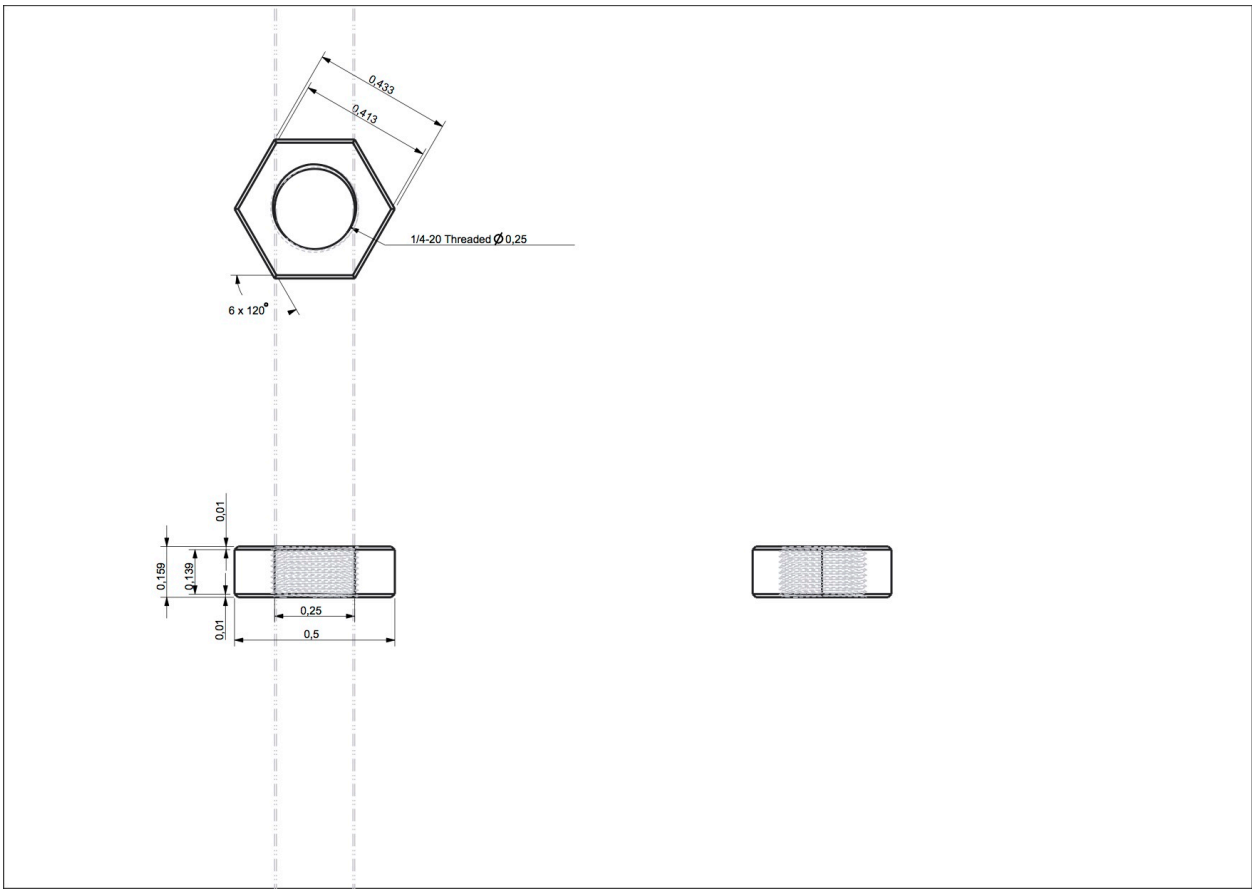

Figure A5: Item 5 - ¼” Hex nut (Inches)

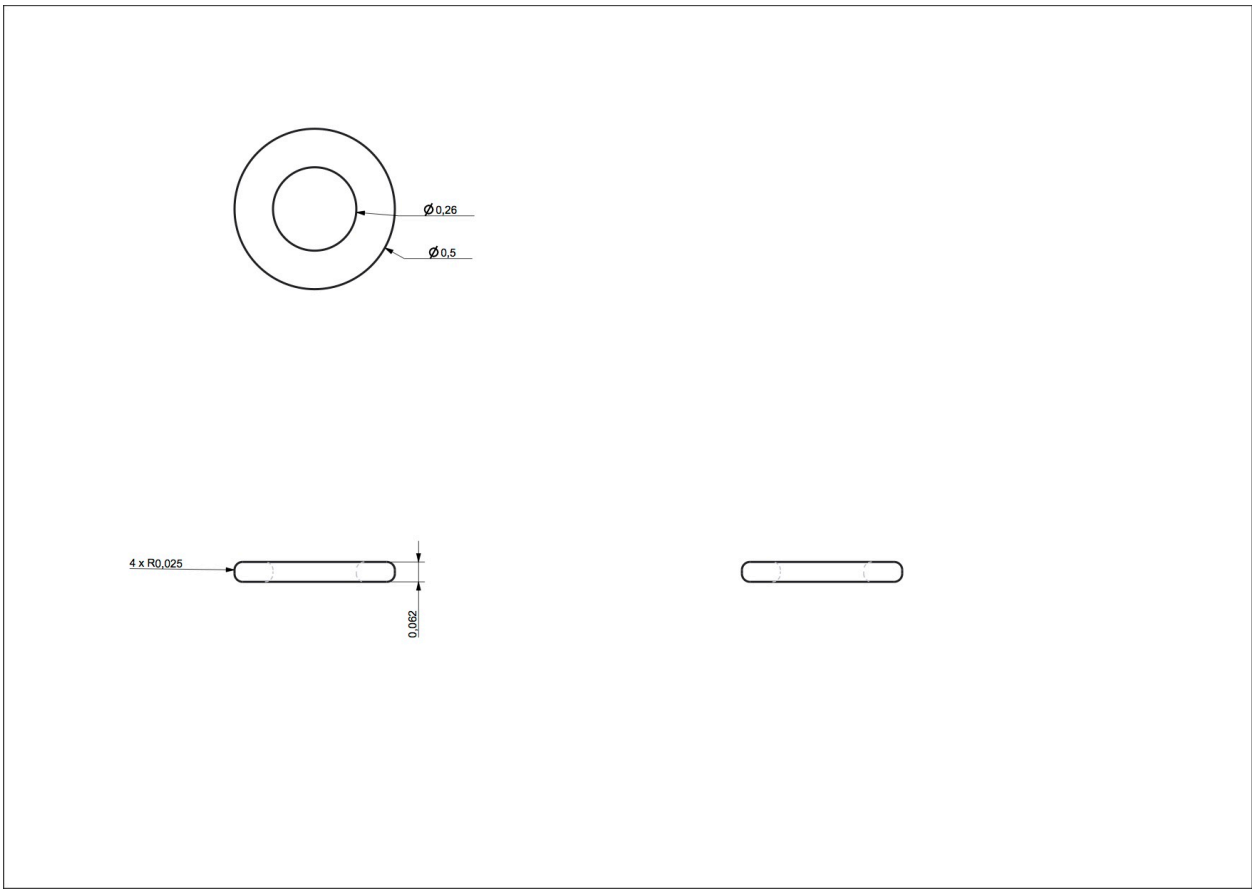

Figure A6: Item 6 - Belt spacer (Inches)

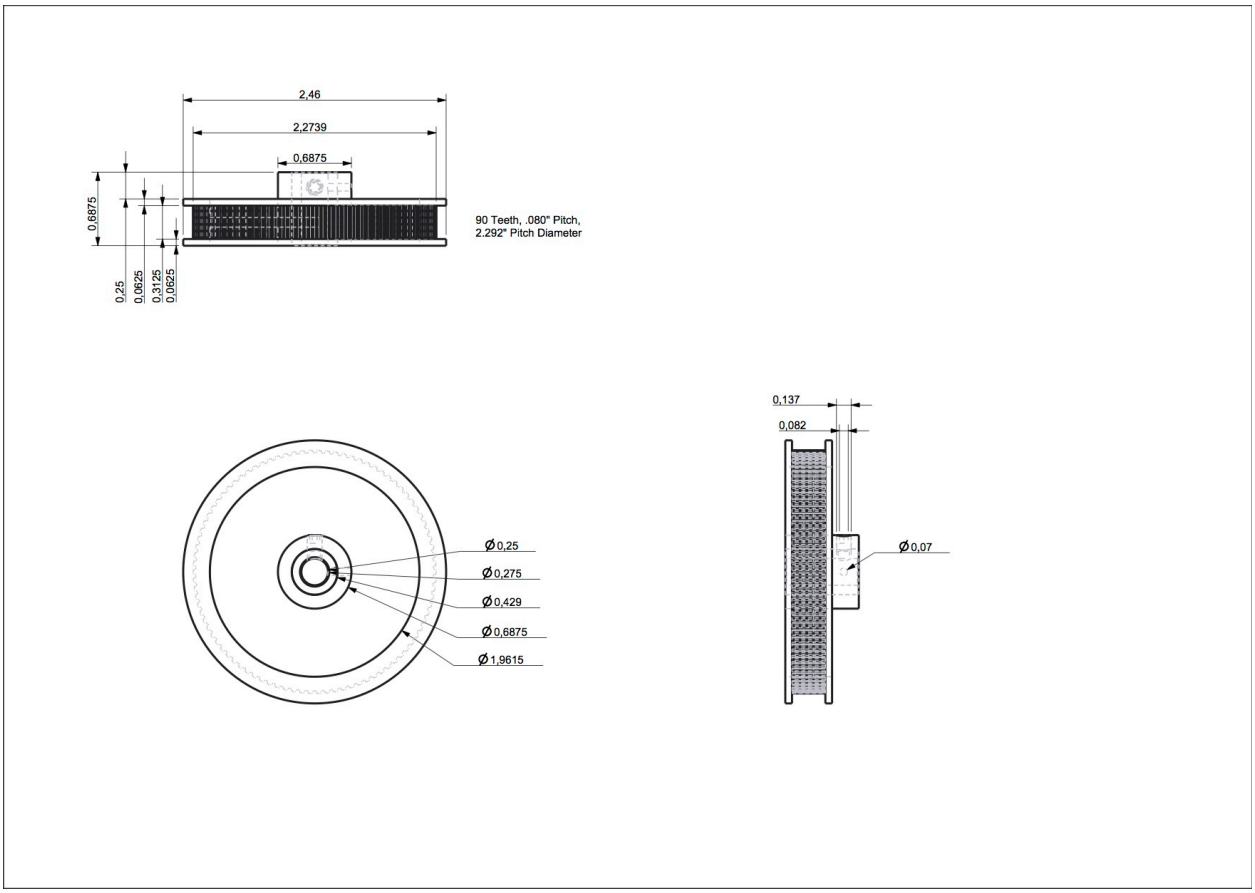

Figure A7: Item 7 – 90 tooth timing belt (SDP-SI Part # A 6Z16-090DF2508) (Inches)

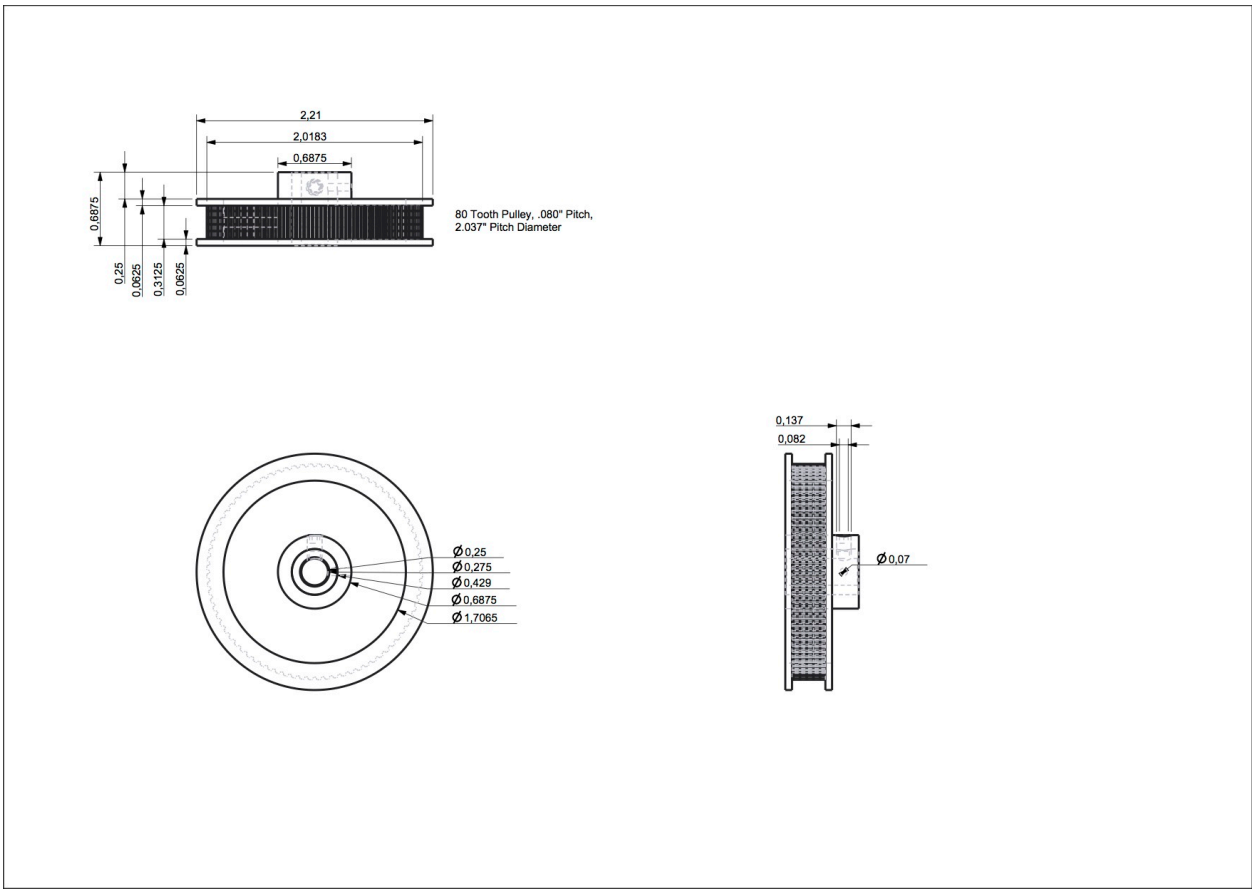

Figure A8: Item 8 – 80 tooth pulley (SDP-SI Part # A 6Z16-080DF2508) (Inches)

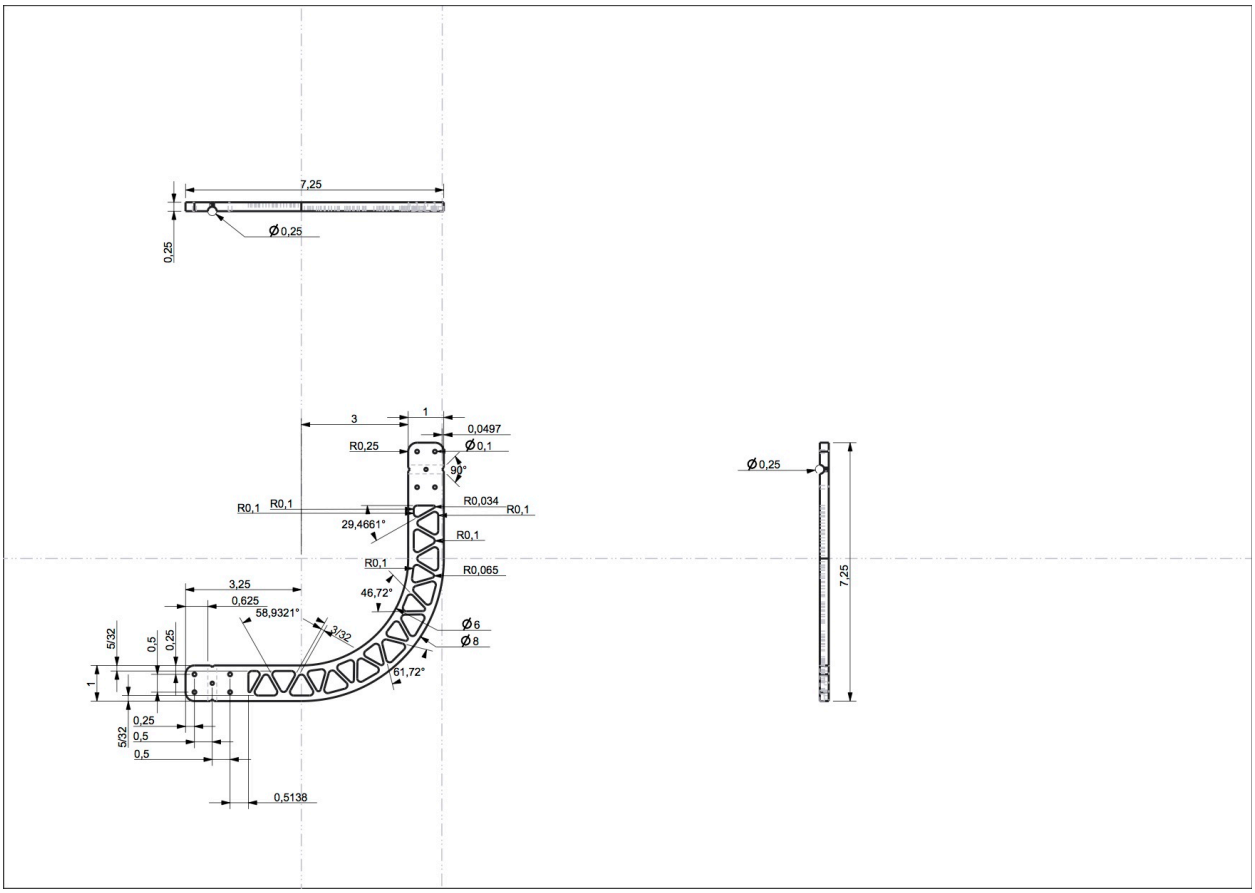

Figure A9: Item 9 – Delrin gimbal link 1 (Inches)

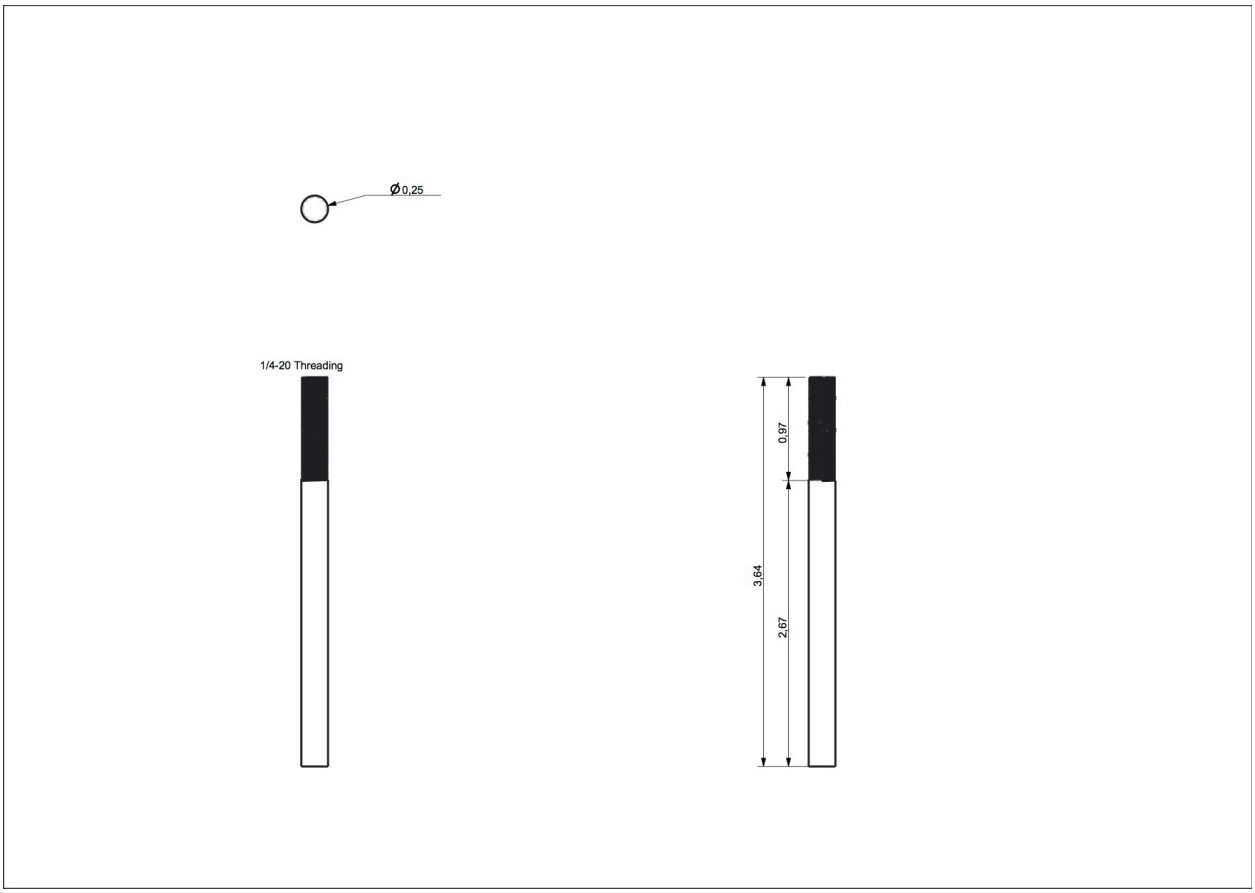

Figure A10: Item 10 – ¼” gimbal axle (Inches)

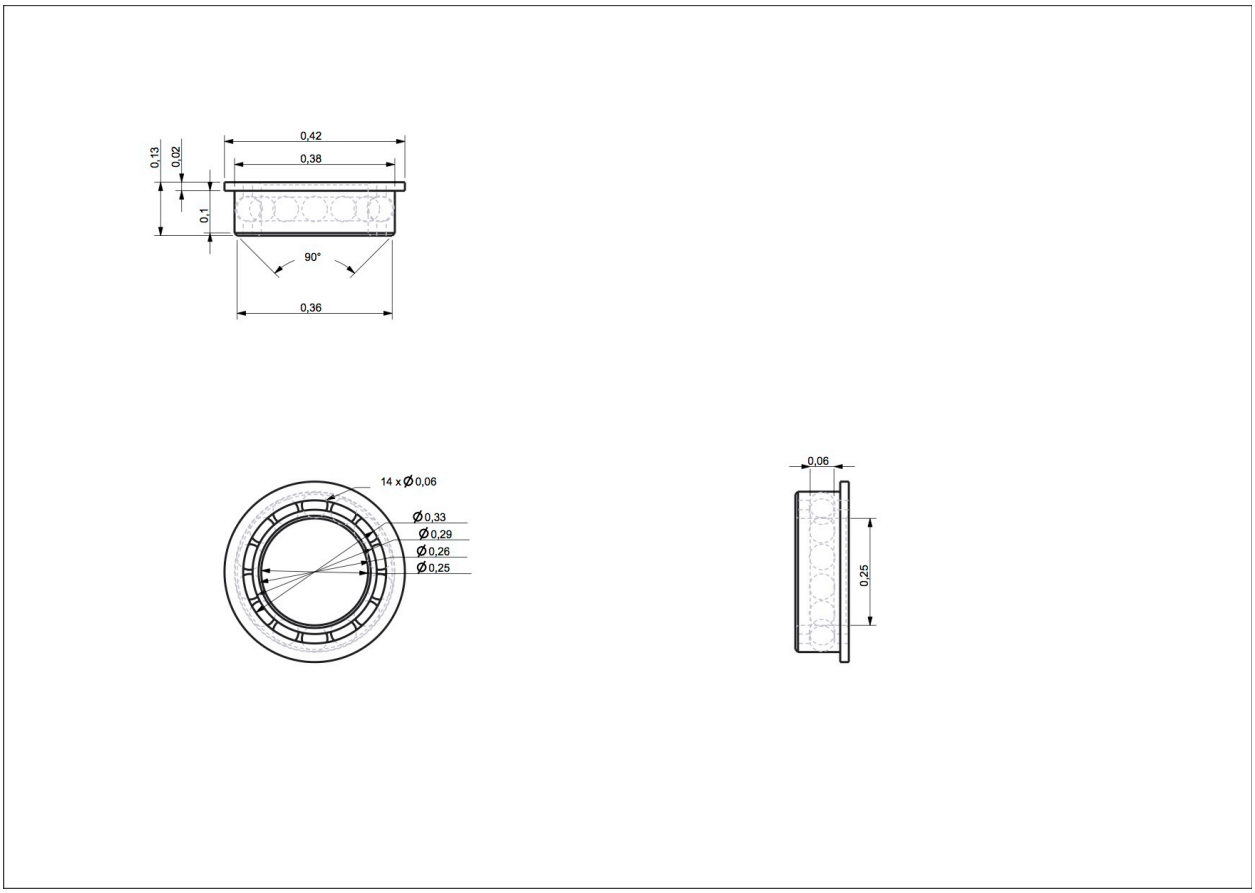

Figure A11: Item 11 – Open ball bearing (Inches)

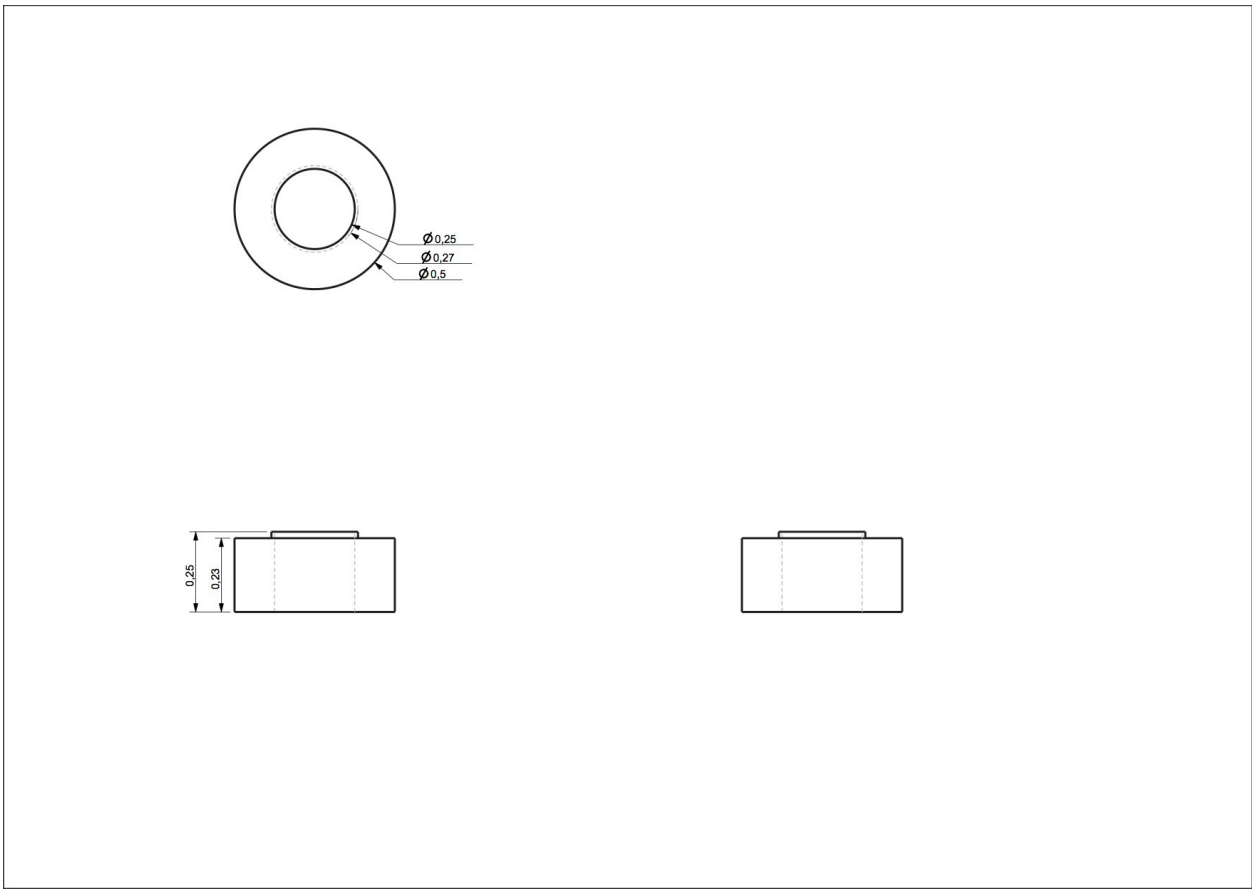

Figure A12: Item 12 – Bearing spacer (Inches)

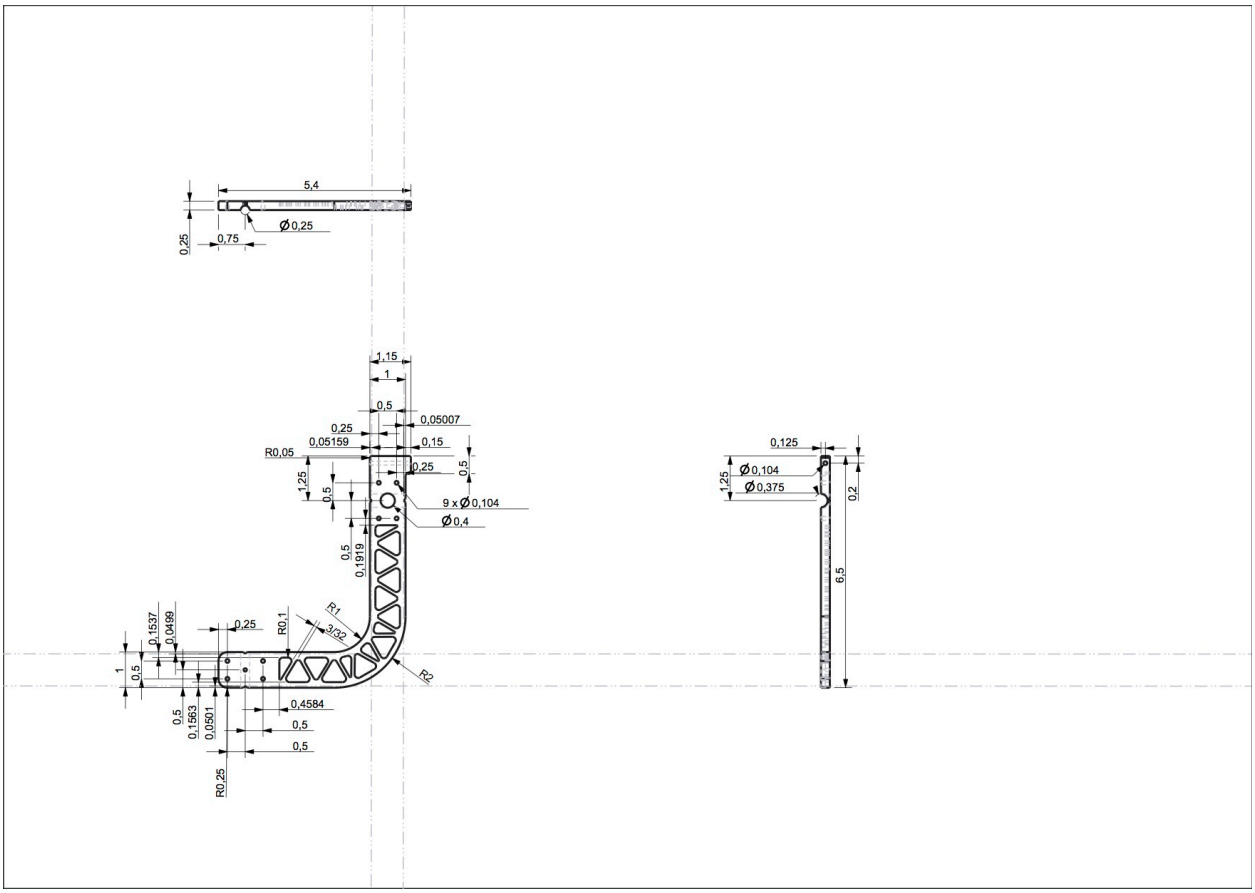

Figure A13: Item 13 – Delrin gimbal link 2 (Inches)

EC-max 22 Ø22 mm, brushless, 25 Watt

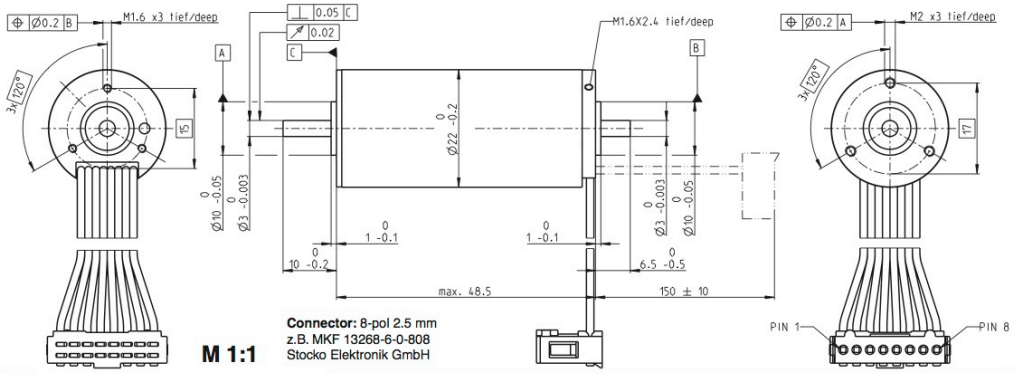

Stock program
Standard program
Special program (on request)

Part Numbers

		283856	283857	283858	283859	283860
Motor Data						
	Values at nominal voltage					
1	Nominal voltage	V	12	18	24	36	48
2	No load speed	rpm	12400	12900	12900	12200	12900
3	No load current	mA	226	161	121	73.5	60.4
4	Nominal speed	rpm	9800	10300	10400	9630	10500
5	Nominal torque (max. continuous torque)	mNm	23	21.8	22.7	22.5	23.2
6	Nominal current (max. continuous current)	A	2.71	1.8	1.4	0.872	0.716
7	Stall torque	mNm	114	112	121	111	127
8	Stall current	A	12.6	8.55	6.97	4	3.66
9	Max. efficiency	%	76	75	76	75	77
	Characteristics						
10	Terminal resistance phase to phase	Ω	0.955	2.1	3.44	9.01	13.1
11	Terminal inductance phase to phase	mH	0.0498	0.103	0.182	0.462	0.729
12	Torque constant	mNm/A	9.1	13	17.4	27.7	34.8
13	Speed constant	rpm/V	1050	732	549	345	274
14	Speed/torque gradient	rpm/mNm	110	118	109	112	103
15	Mechanical time constant	ms	5.14	5.5	5.06	5.23	4.82
16	Rotor inertia	gcm²	4.45	4.45	4.45	4.45	4.45

Specifications

Thermal data

17	Thermal resistance housing-ambient	10.2 K/W
18	Thermal resistance winding-housing	1.02 K/W
19	Thermal time constant winding	1.99 s
20	Thermal time constant motor	628 s
21	Ambient temperature	-40…+100°C
22	Max. winding temperature	+155°C

Mechanical data (preloaded ball bearings)

23	Max. speed		18000 rpm
24	Axial play at axial load	< 4 N	0 mm
		> 4 N	0.14 mm
25	Radial play		preloaded
26	Max. axial load (dynamic)		3.5 N
27	Max. force for press fits (static)		60 N
	(static, shaft supported)		1000 N
28	Max. radial load, 5 mm from flange		16 N

Other specifications

29	Number of pole pairs	1
30	Number of phases	3
31	Weight of motor	110 g

Values listed in the table are nominal.

Connection (Cable AWG 24)

brown	Motor winding 1	Pin 1
red	Motor winding 2	Pin 2
orange	Motor winding 3	Pin 3
yellow	V_{Hall} 3…24 VDC	Pin 4
green	GND	Pin 5
blue	Hall sensor 1	Pin 6
violet	Hall sensor 2	Pin 7
grey	Hall sensor 3	Pin 8

Wiring diagram for Hall sensors see p. 33

Operating Range

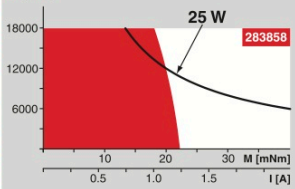

Comments

Continuous operation
In observation of above listed thermal resistance (lines 17 and 18) the maximum permissible winding temperature will be reached during continuous operation at 25°C ambient.
= Thermal limit.

Short term operation
The motor may be briefly overloaded (recurring).

Assigned power rating

maxon Modular System

Overview on page 20–25

Planetary Gearhead
Ø22 mm
0.5 - 3.4 Nm
Seite 294/297

Planetary Gearhead
Ø32 mm
1.0 - 6.0 Nm
Page 308

Koaxdrive
Ø32 mm
1.0 - 4.5 Nm
Page 312

Spindle Drive
Ø32 mm
Page 334–336

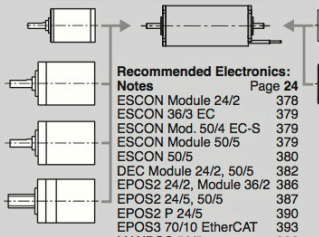

Recommended Electronics:

Notes	Page 24
ESCON Module 24/2	378
ESCON 36/3 EC	379
ESCON Mod. 50/4 EC-S	379
ESCON Module 50/5	379
ESCON 50/5	380
DEC Module 24/2, 50/5	382
EPOS2 24/2, Module 36/2	386
EPOS2 24/5, 50/5	387
EPOS2 P 24/5	390
EPOS3 70/10 EtherCAT	393
MAXPOS 50/5	396

Encoder MR
128/256/512 CPT,
2/3 channels
Page 354

Brake AB 20
24 VDC
0.1 Nm
Page 406

Figure A14: Item 14 – 22 mm DC motor

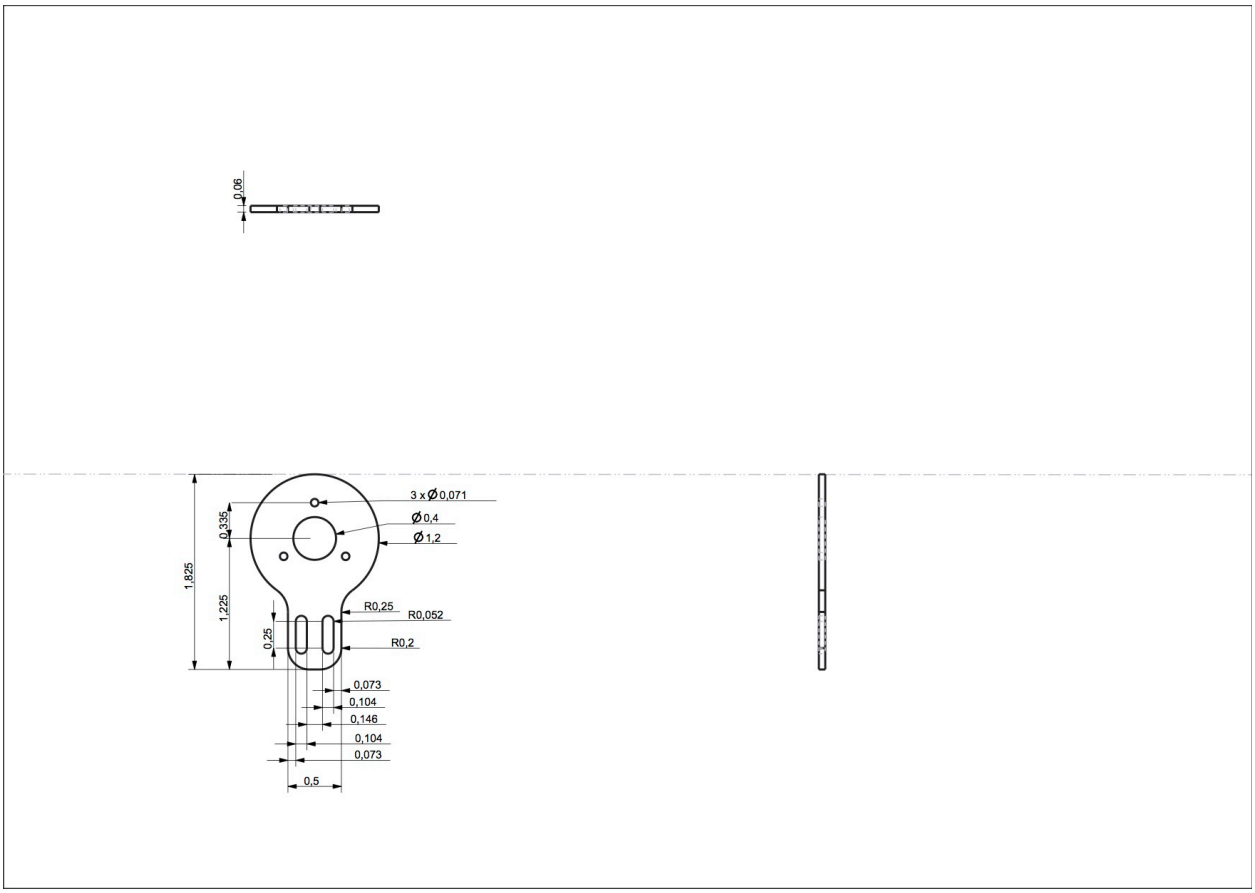

Figure A15: Item 15 – 22 mm motor mount (Inches)

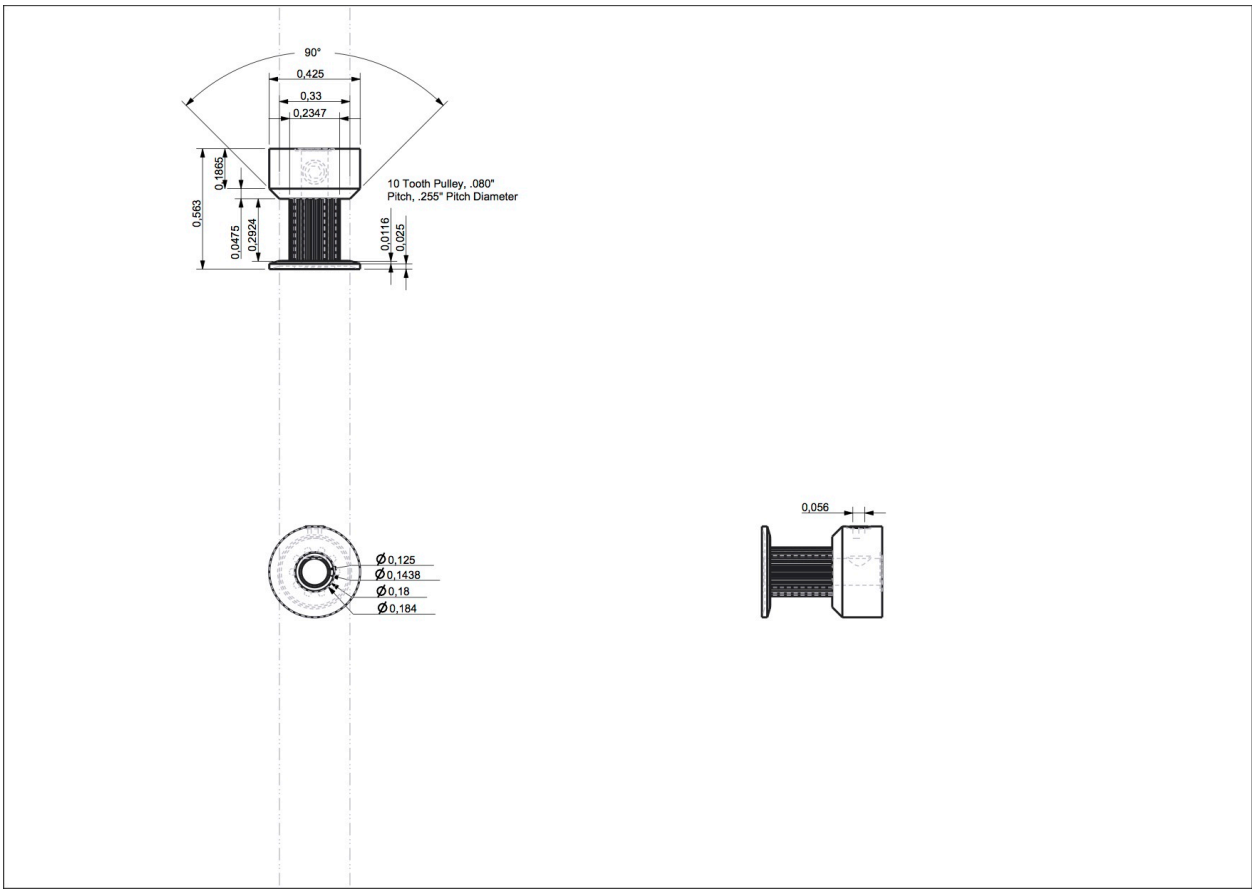

Figure A16: Item 16 – 10 tooth timing belt (SDP-SI Part # A 6N16-010DF1204) (Inches)

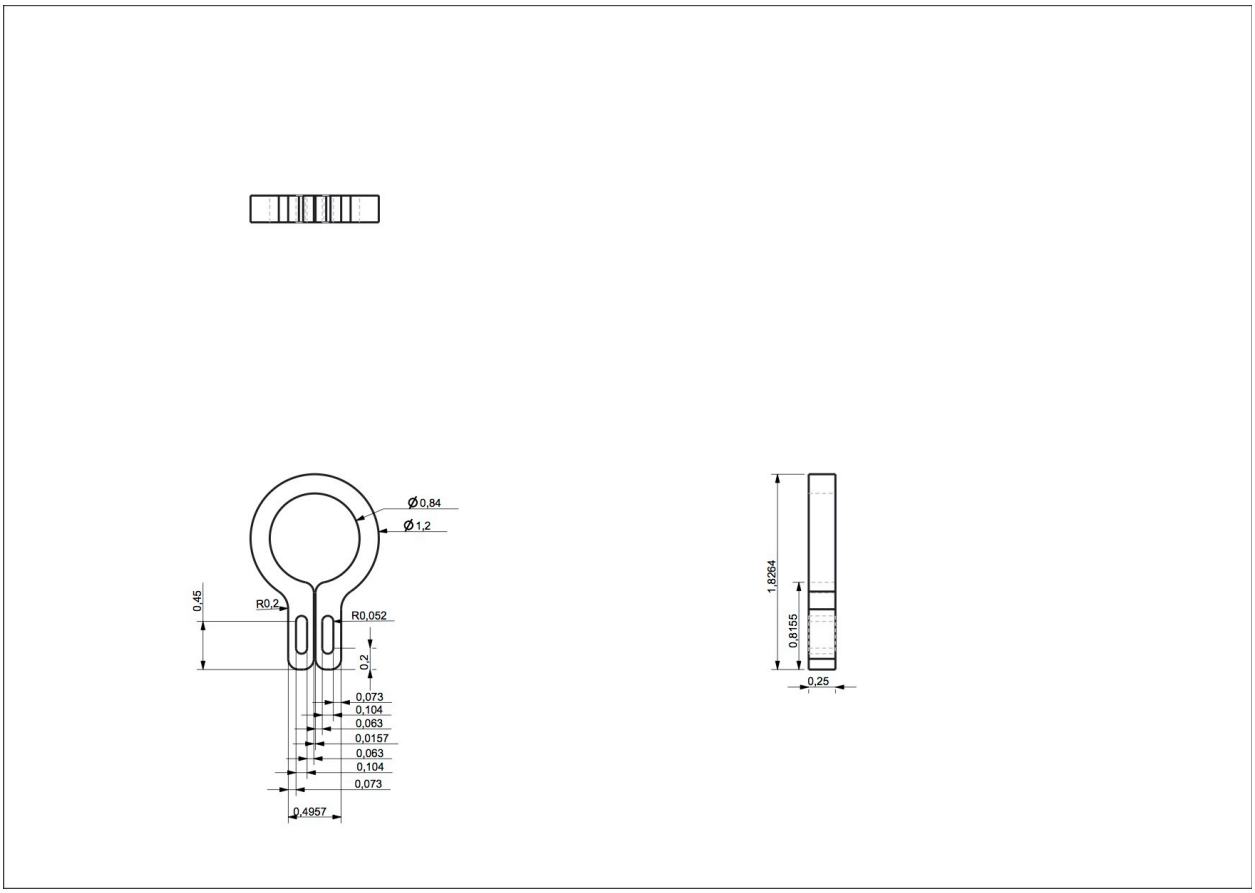

Figure A17: Item 17 – Acrylic 22 mm motor holder (Inches)

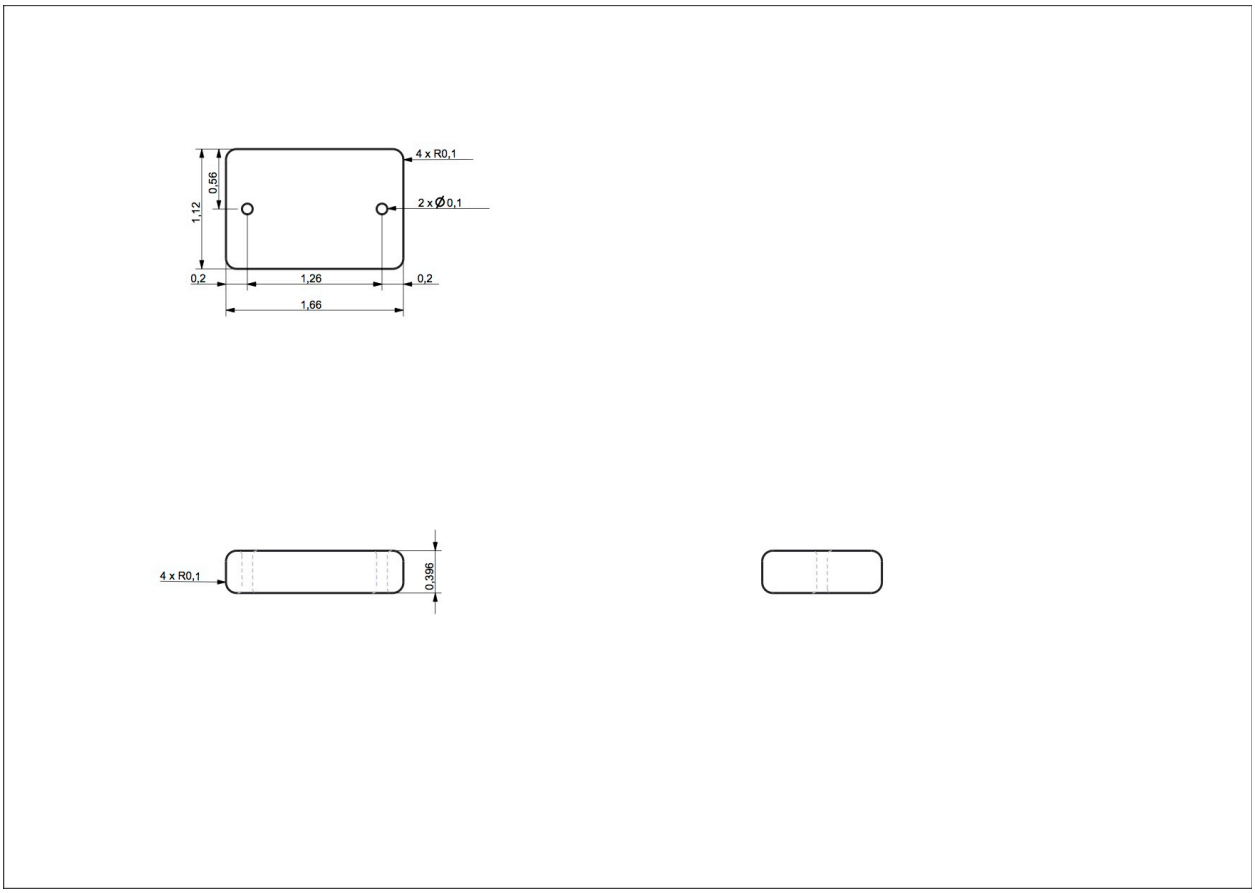

Figure A18: Item 18 – Alpha 2 ABS wedge (Inches)

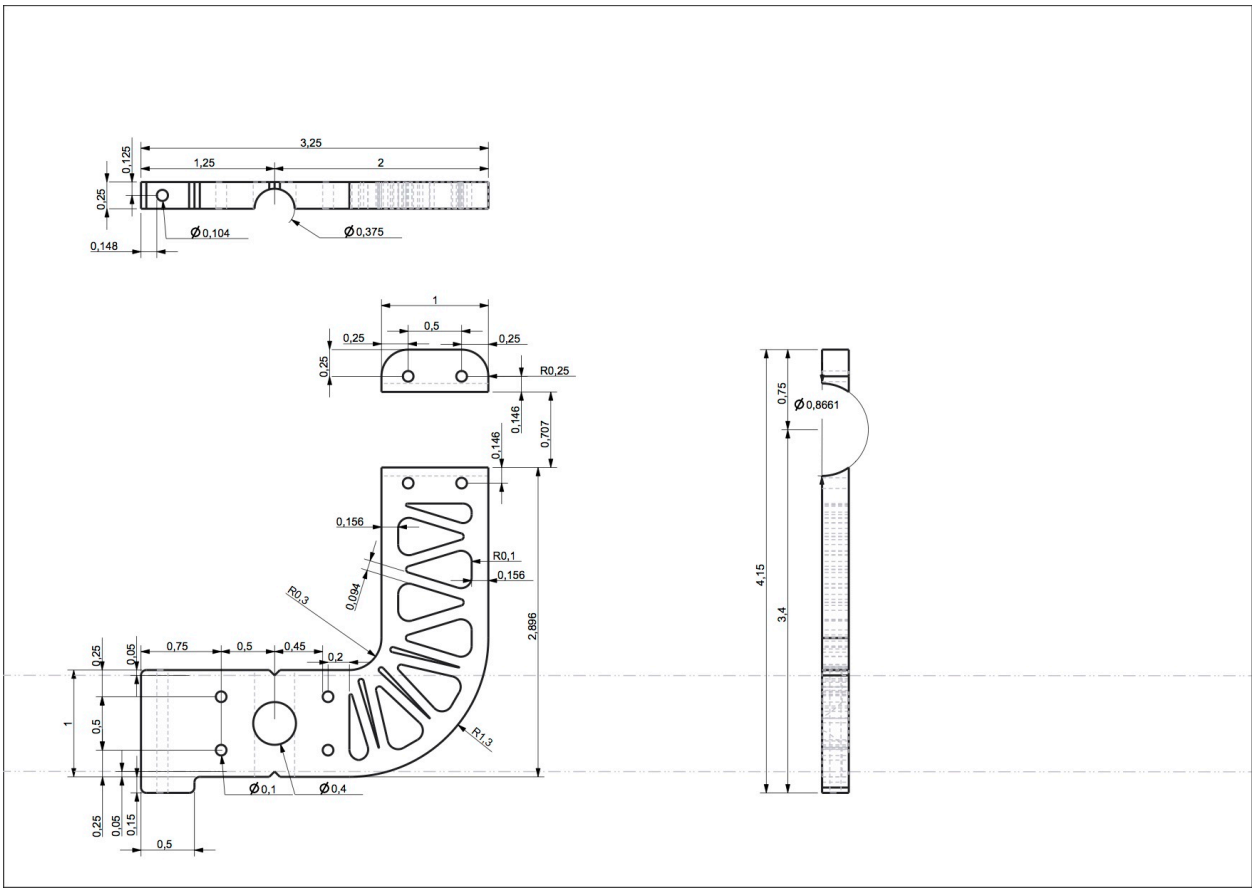

Figure A19: Item 19 – Delrin gimbal link 3 (Inches)

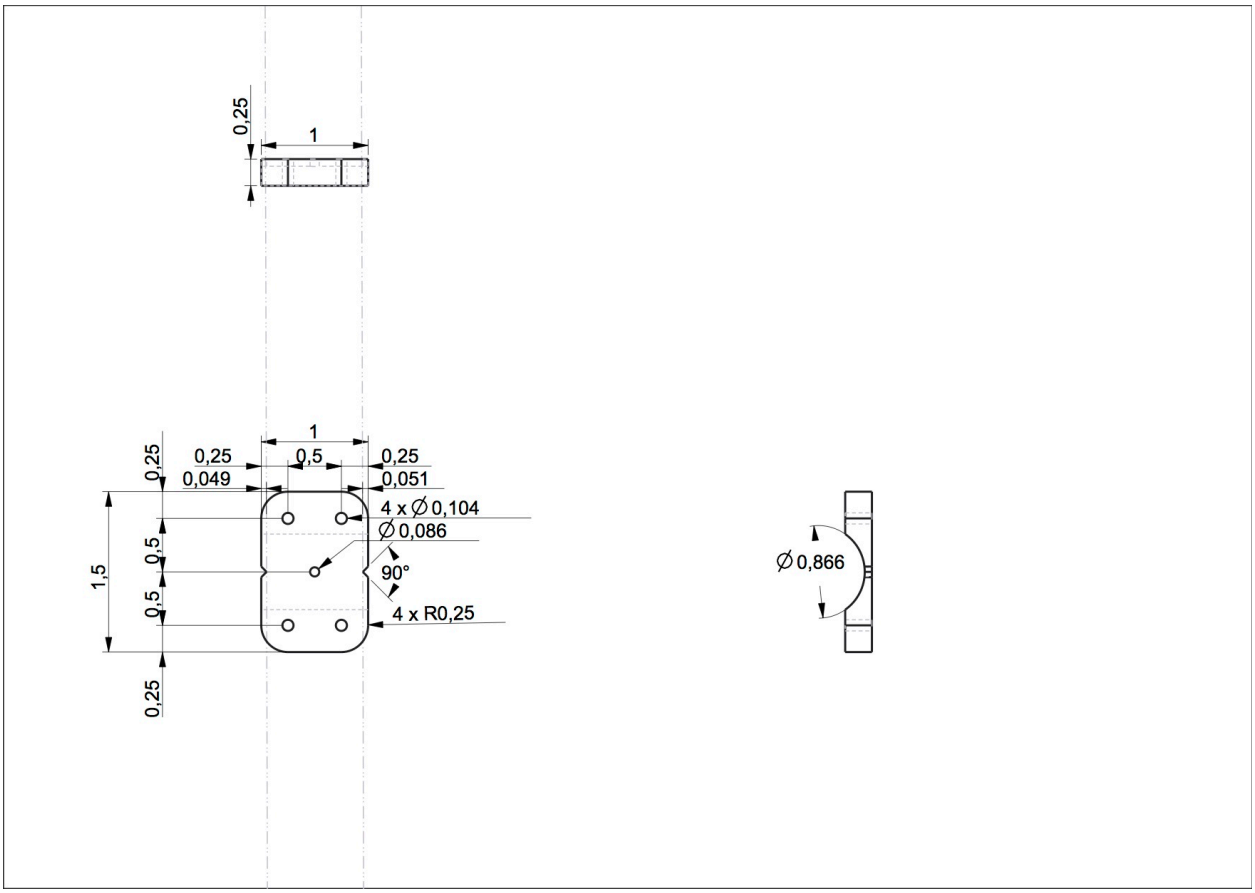

Figure A20: Item 20 – Delrin gimbal link 3 outer layer (Inches)

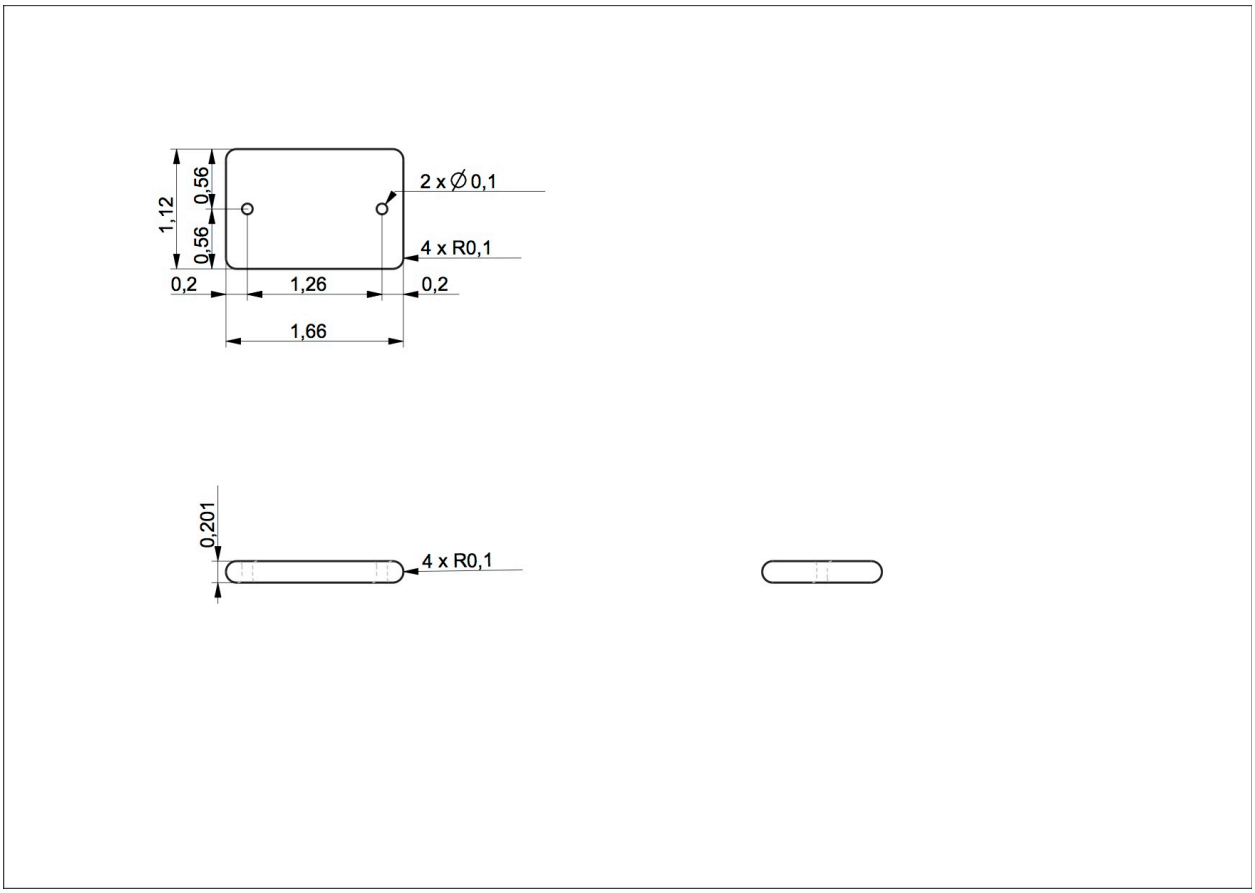

Figure A21: Item 21 – Alpha 3 ABS wedge (Inches)

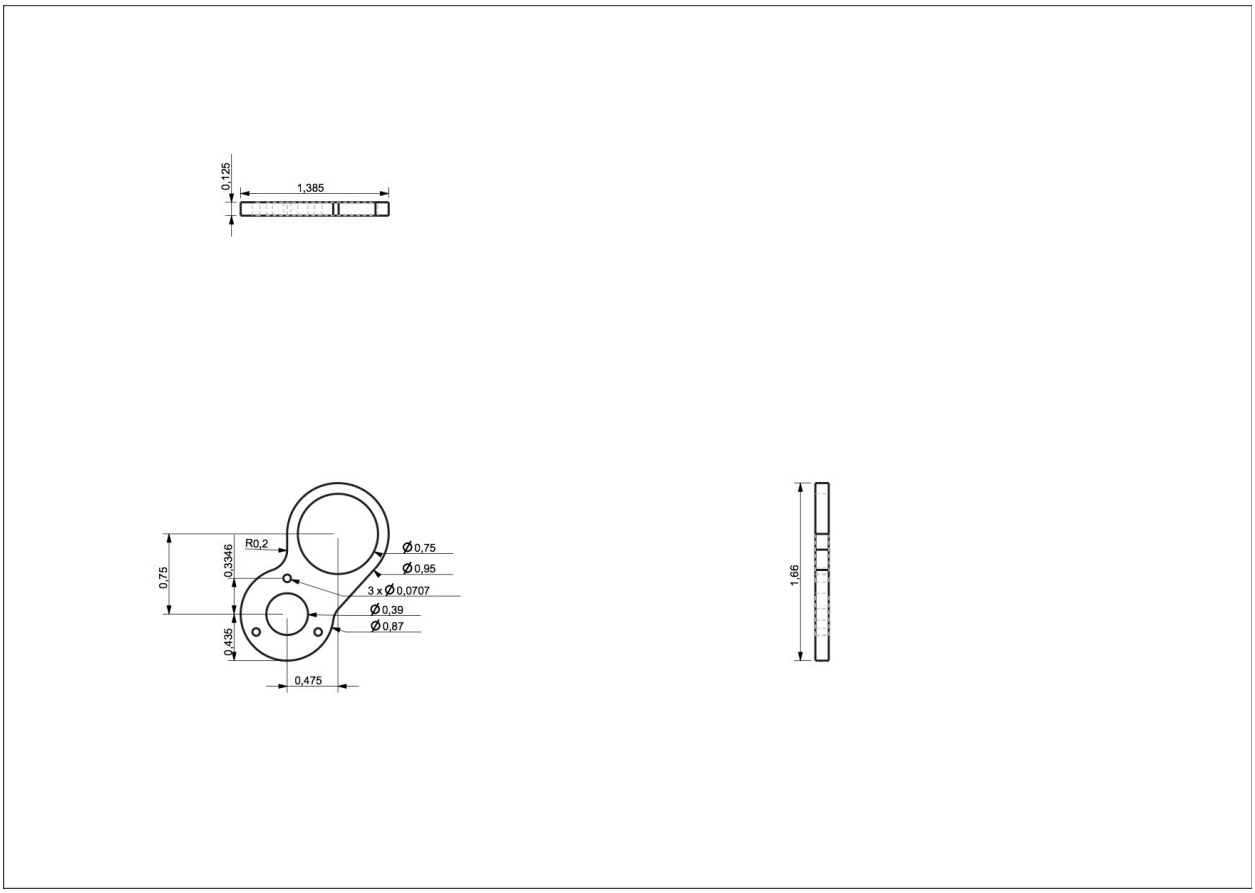

Figure A22: Item 22 – 22 mm motor delrin mounting plate (Inches)

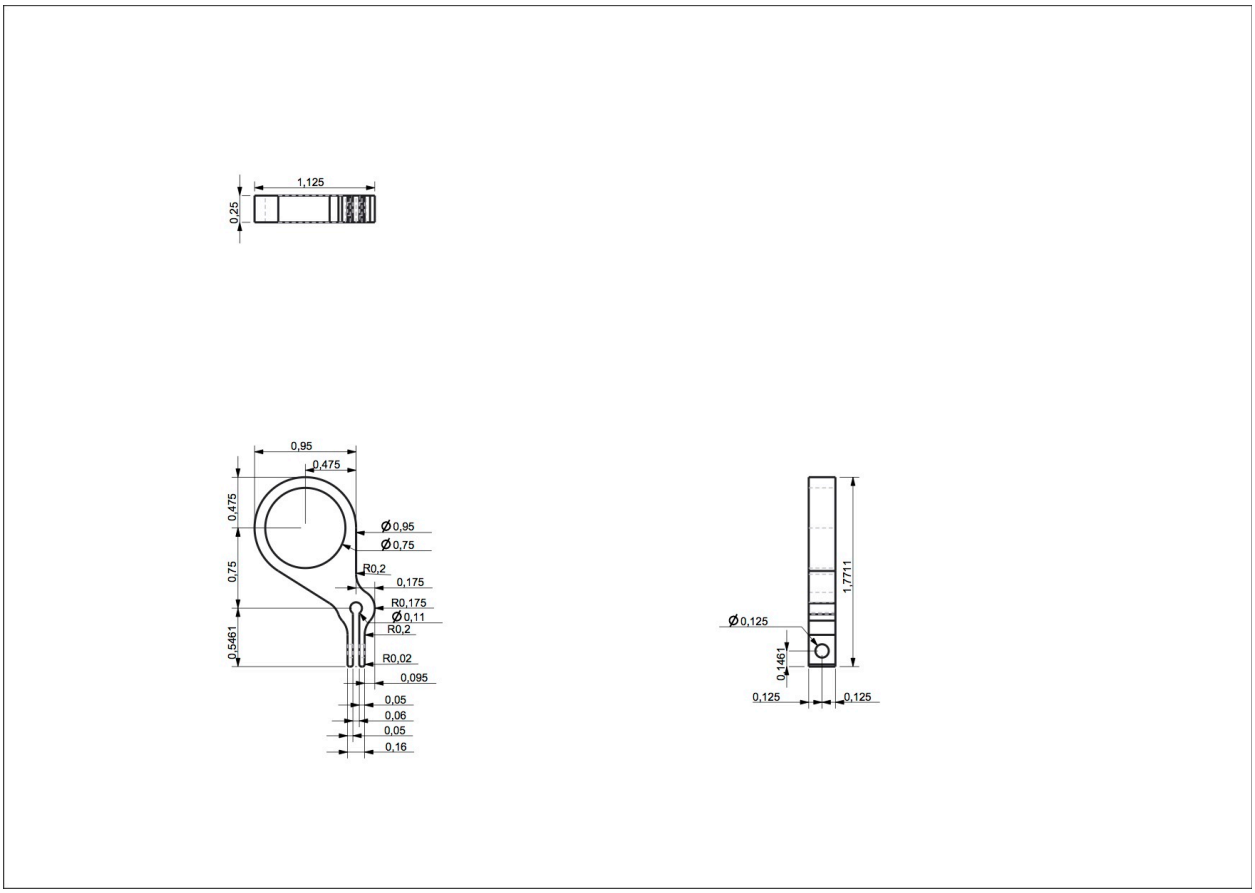

Figure A23: Item 23 – End effector gripper (Inches)

Attributes	Values
Working Length (in) (1.03 to 5)	5 Set
CSC #	12013
OD (in)	0.6710
OD (mm)	17.04
ID (in)	0.5770
ID (mm)	14.70
Free Length (in)	5.00
Wire Dia (in)	0.0470
Solid Length (in)	1.030
Material	SST
Ends	CG
Finish	N
Sugg Max Defl (in)	4.0000
Sugg Max Defl (mm)	101.000
Sugg Max Load (lbs)	5.1000
Total Coils	22.00

Figure A24: Item 24 – Compression spring data

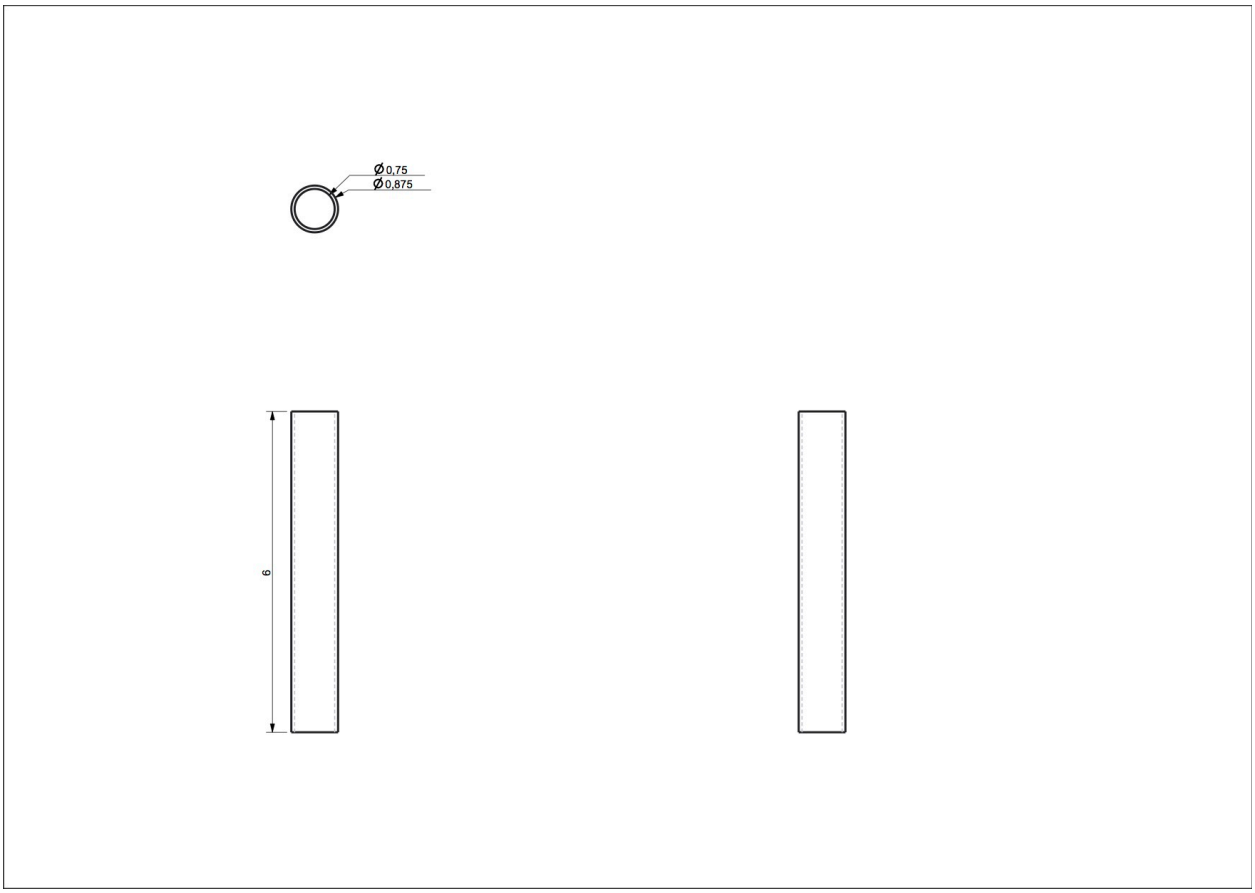

Figure A25: Item 25 – Compression spring delrin tube (Inches)

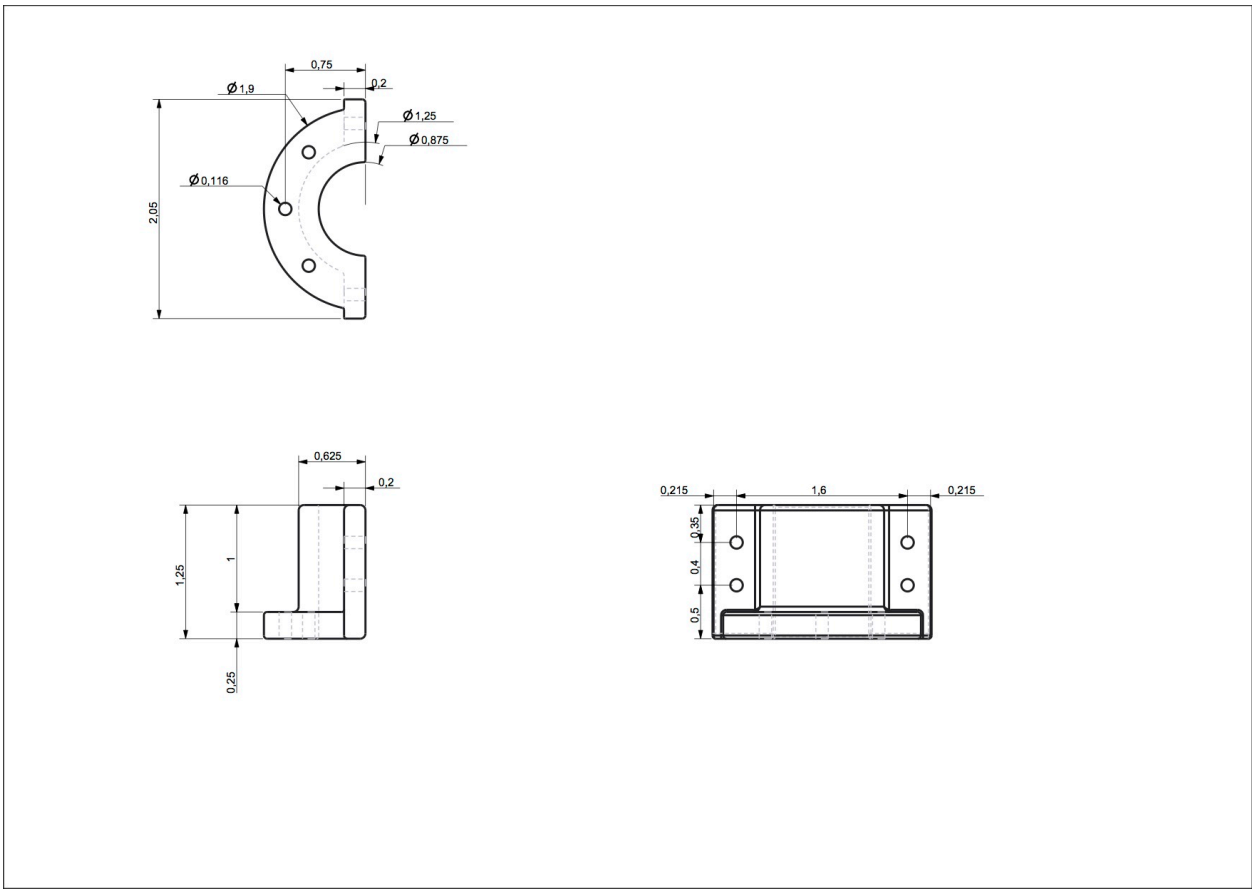

Figure A26: Item 26 – Compression spring delrin tube holder (Inches)

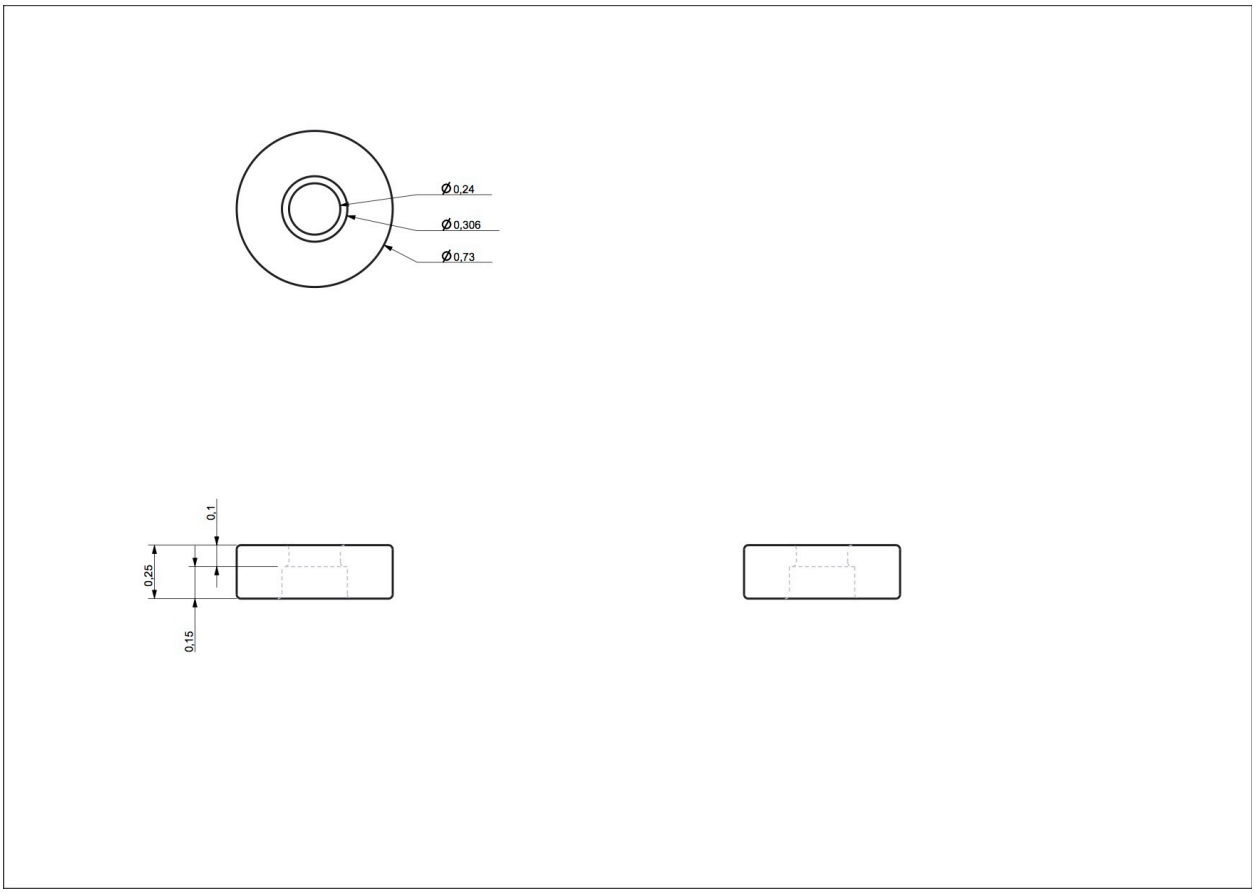

Figure A27: Item 27 – Ceramic eyelet holder (Inches)

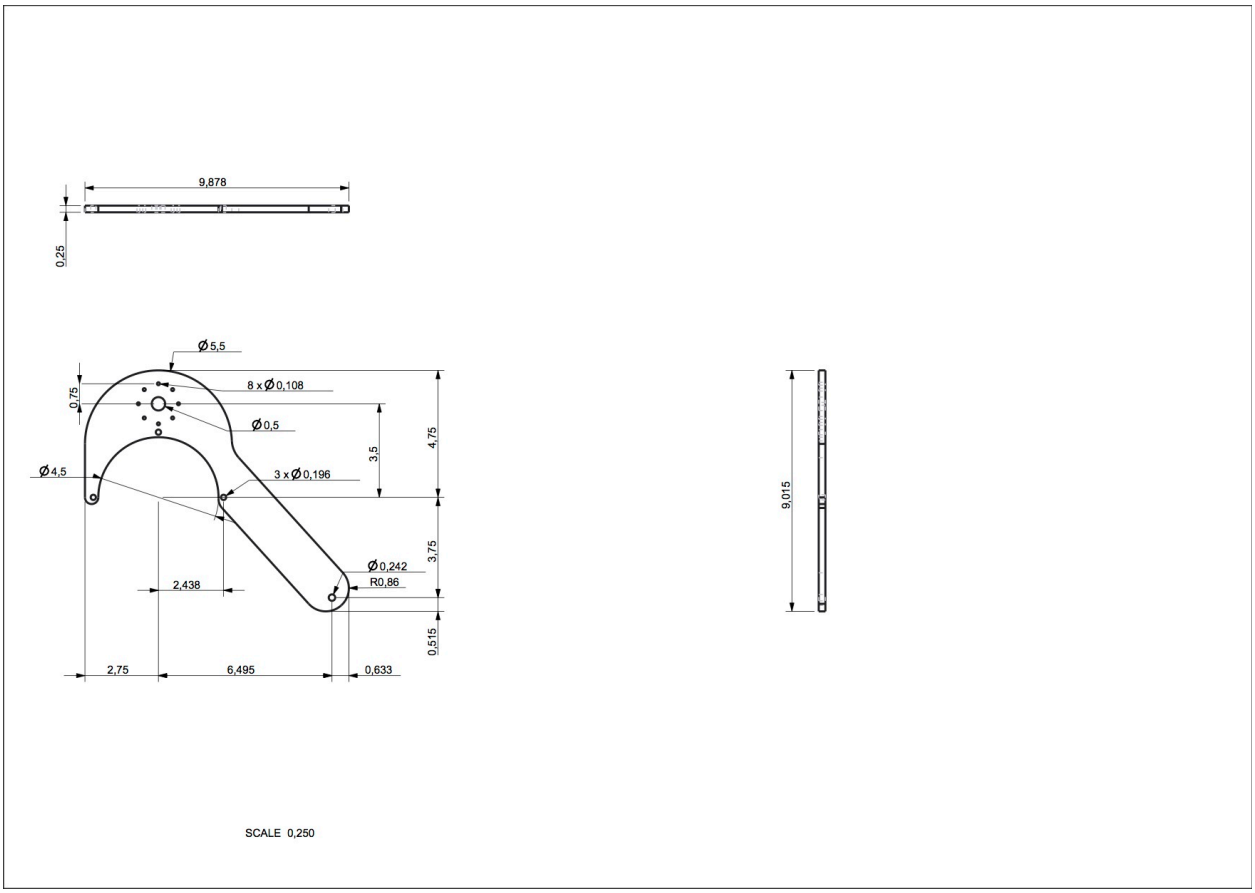

Figure A28: Item 28 – Spring mount delrin plate for base robot (Inches)

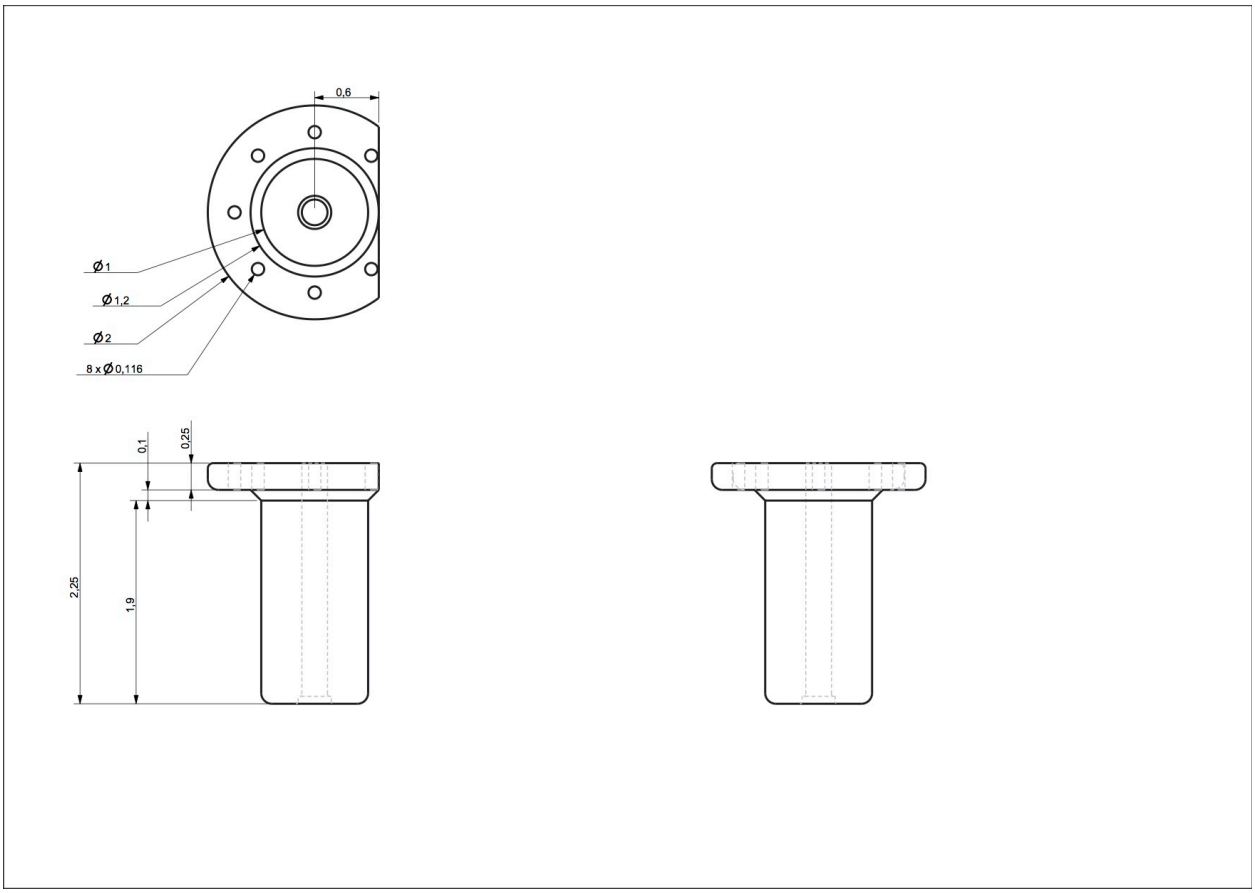

Figure A29: Item 29 – Eyelet mount for inside portion of delrin plate (Inches)

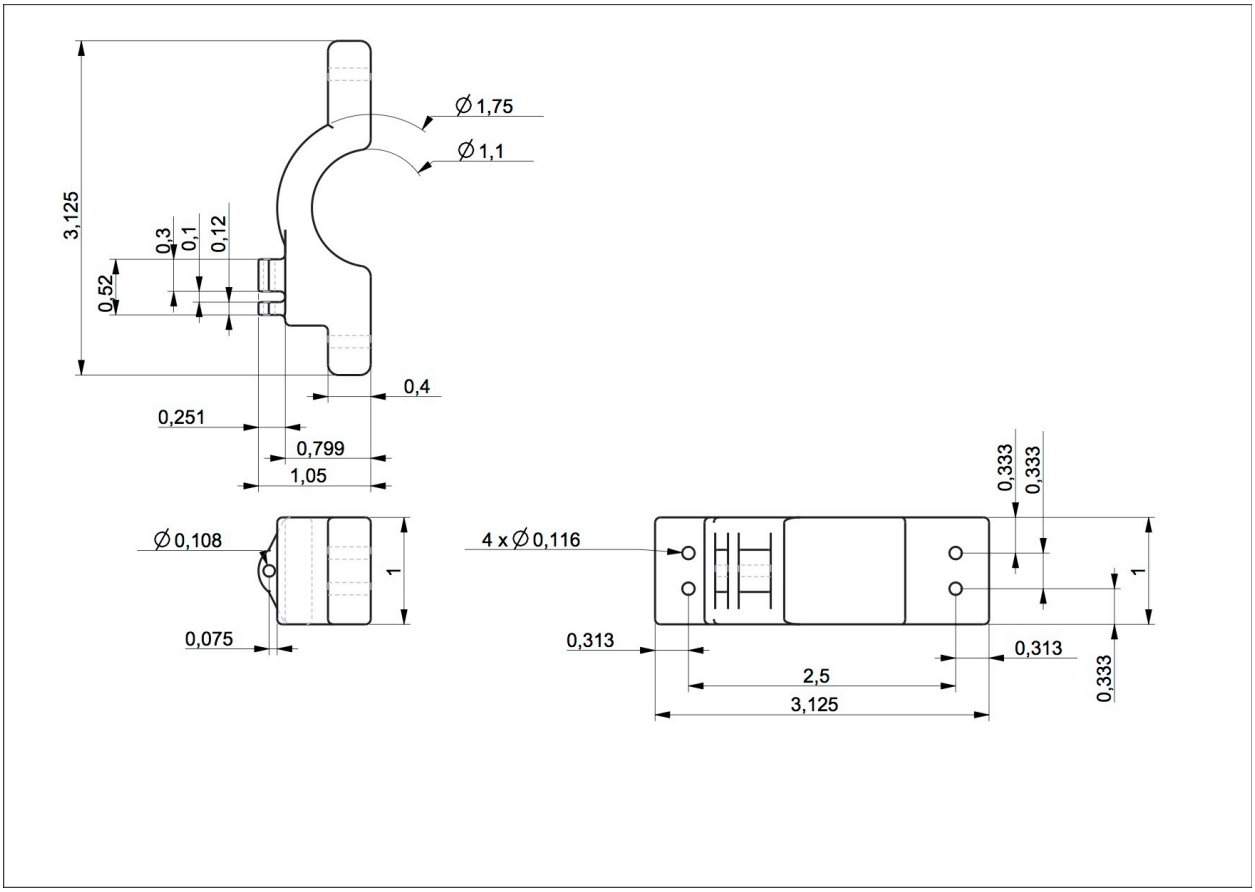

Figure A30: Item 30 – Base robot link 1 mount for compression spring cables (Inches)

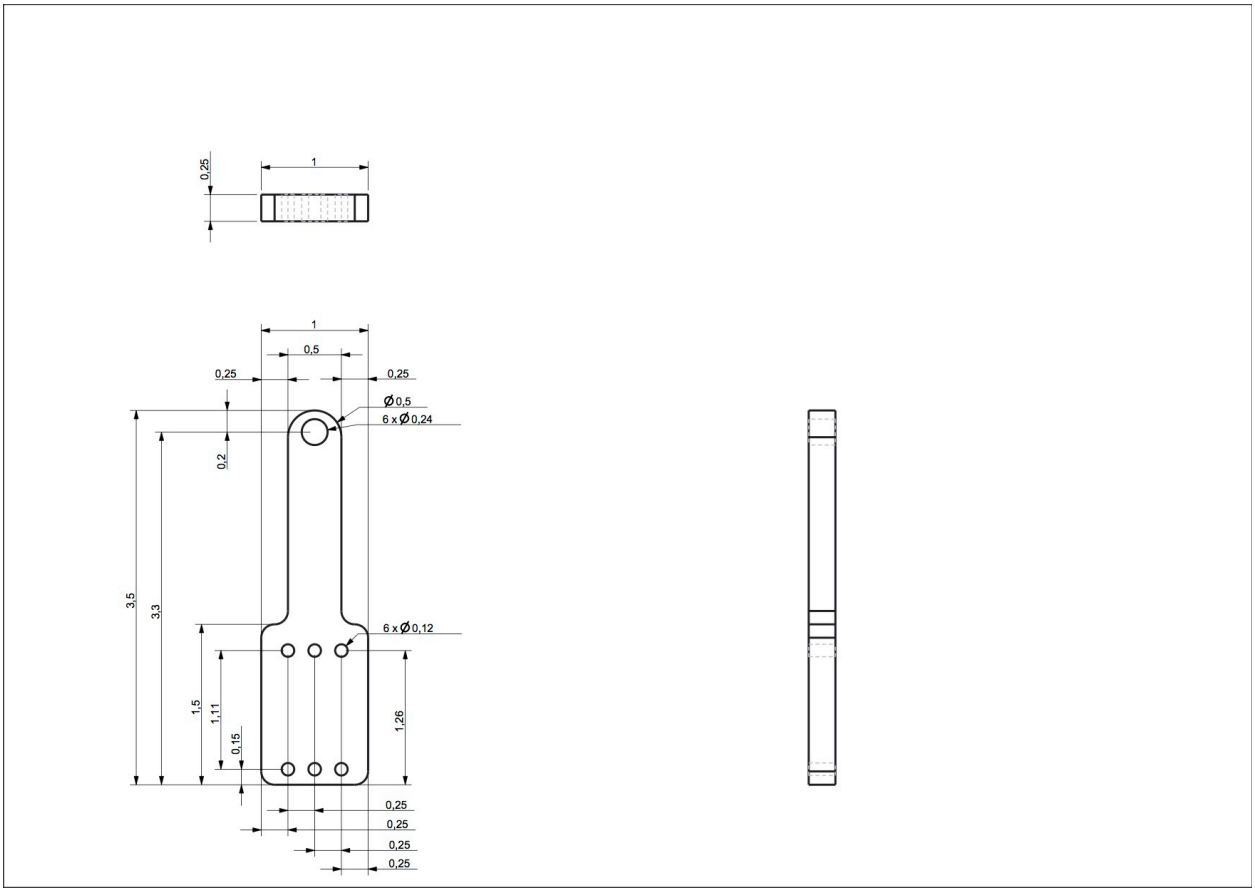

Figure A31: Item 31 – Extension spring mount for link 2 of base robot (Inches)

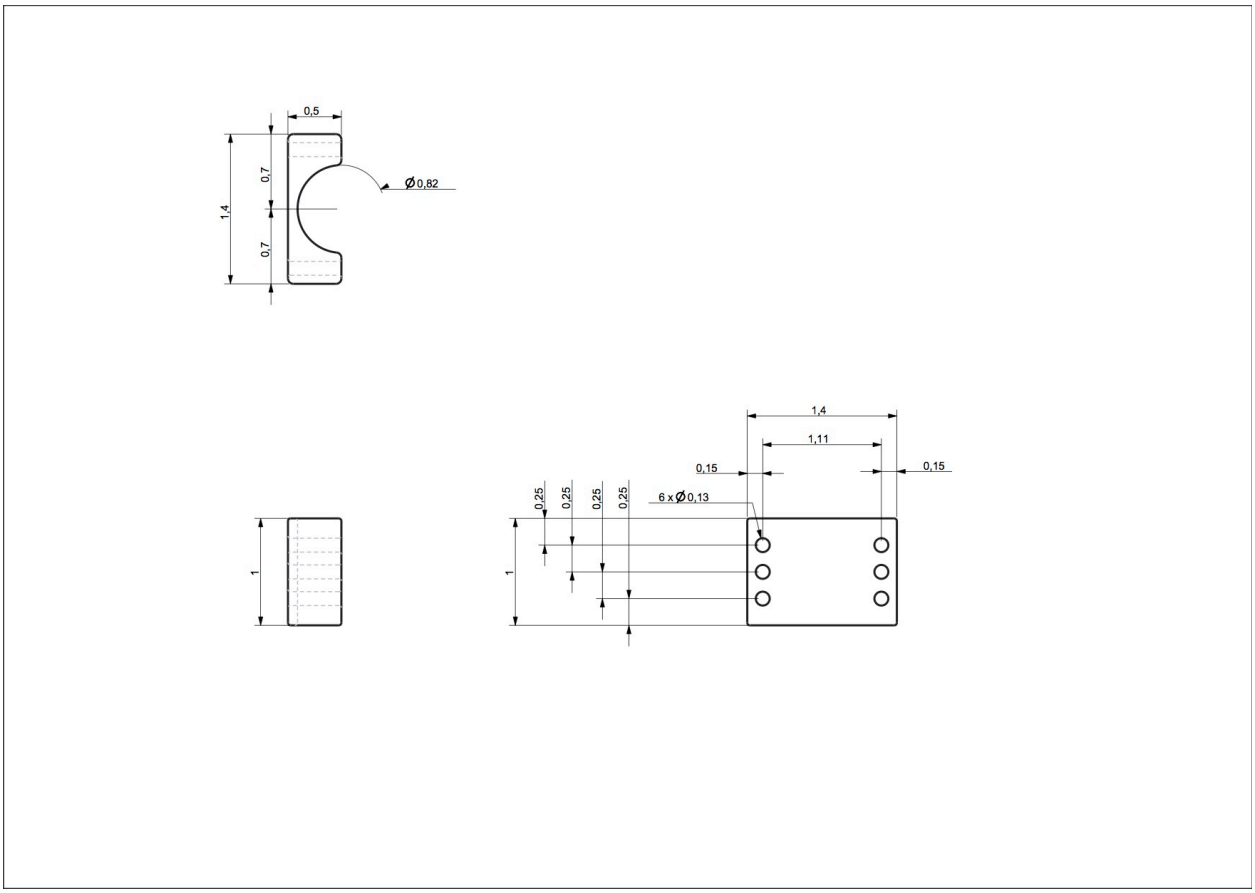

Figure A32: Item 32 – Base robot link 2 holder for delrin spring mount (Inches)

Attributes	Values
Working Length (in) (3 to 10.5)	3 Set
CSC #	80666
OD (in)	0.5000
OD (mm)	12.70
Length (in)	3.00
Rate (lbs/in)	0.80
Wire Dia (in)	0.0410
Material	MW
Finish	N
Sugg Max Defl (in)	7.5000
Sugg Max Defl (mm)	191.000
Sugg Max Load (lbs)	6.5000
Initial Tension (lbs)	0.50

Figure A33: Item 33 – Extension spring data (Inches)

APPENDIX B

Appendix B is composed of schematics describing the electronics package used in operating the robot.

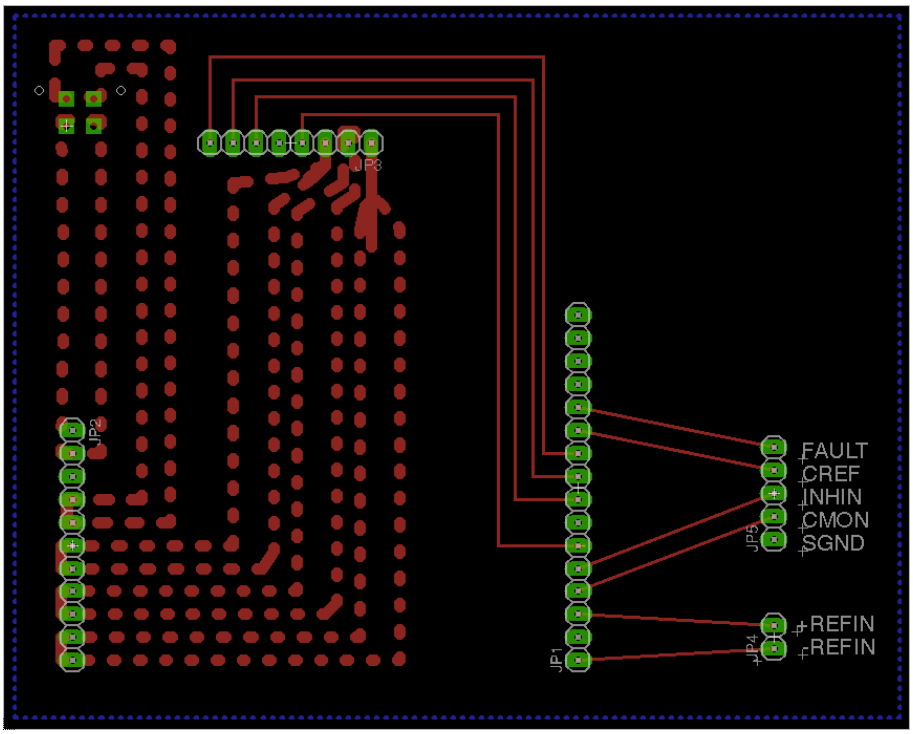

Figure B1: PCB for brushless servoamp

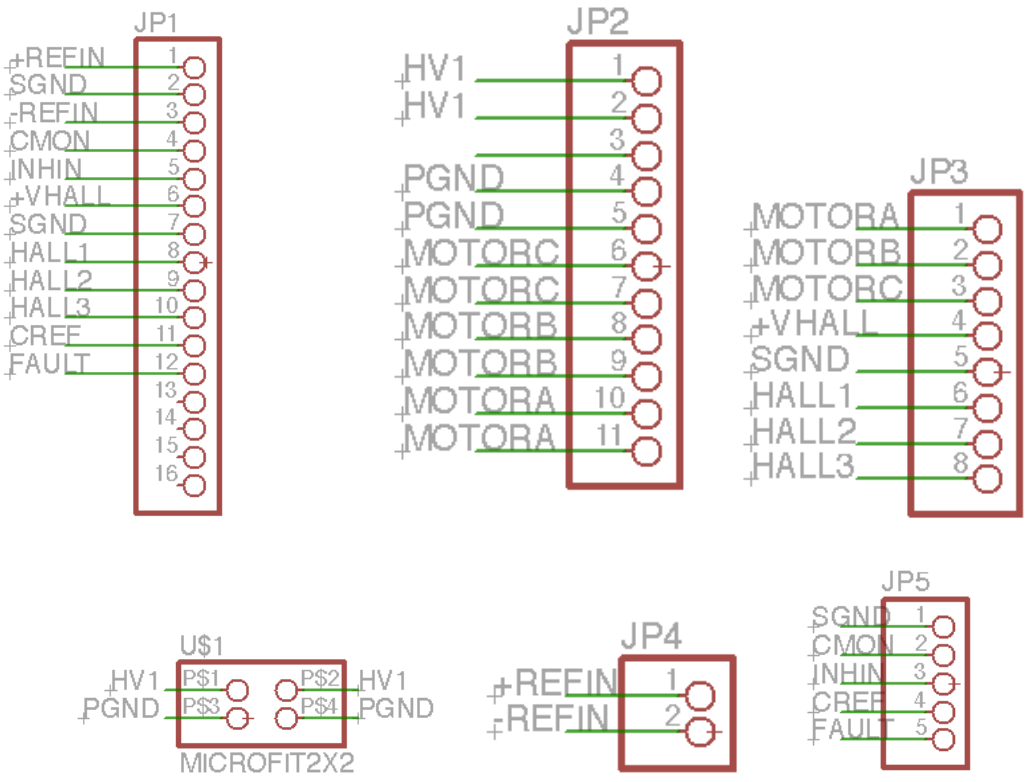

Figure B2: Connections for PCB for brushless servoamps

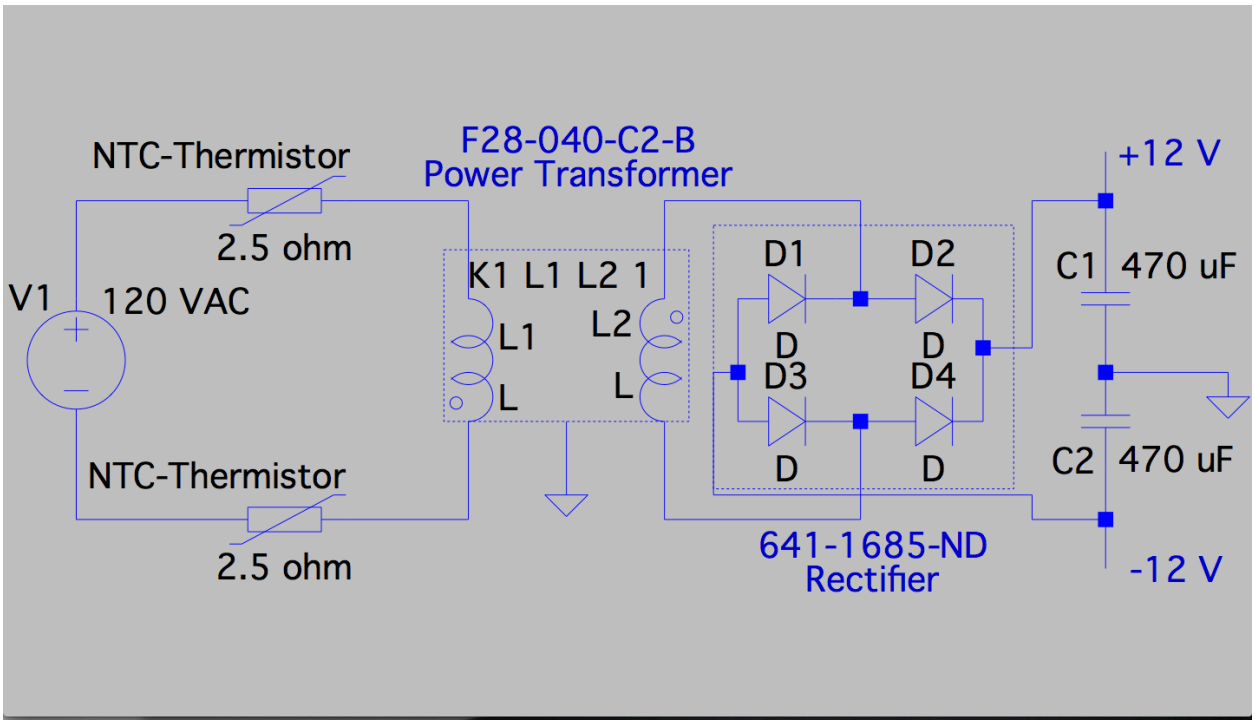

Figure B3: A circuit to transform 120 Vac into +12Vdc and -12Vdc

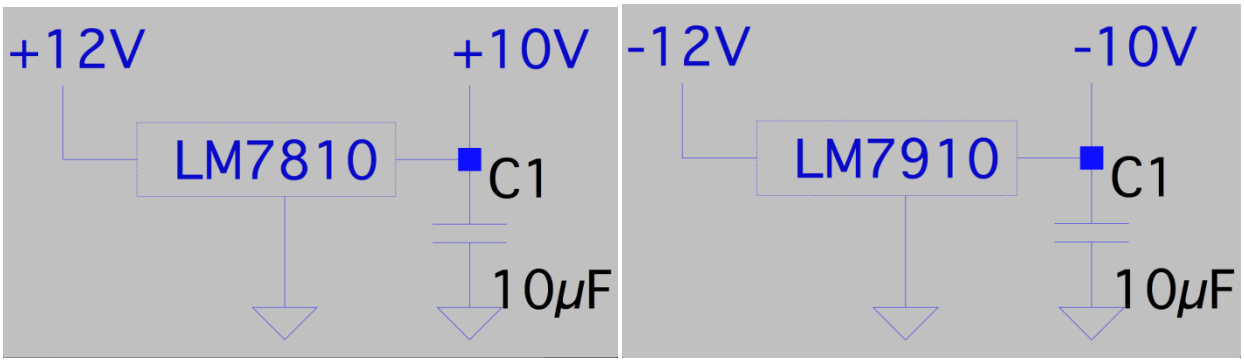

Figure B4: Voltage regulators converting +12 V into +10 V and -12 V into -10 V, respectively

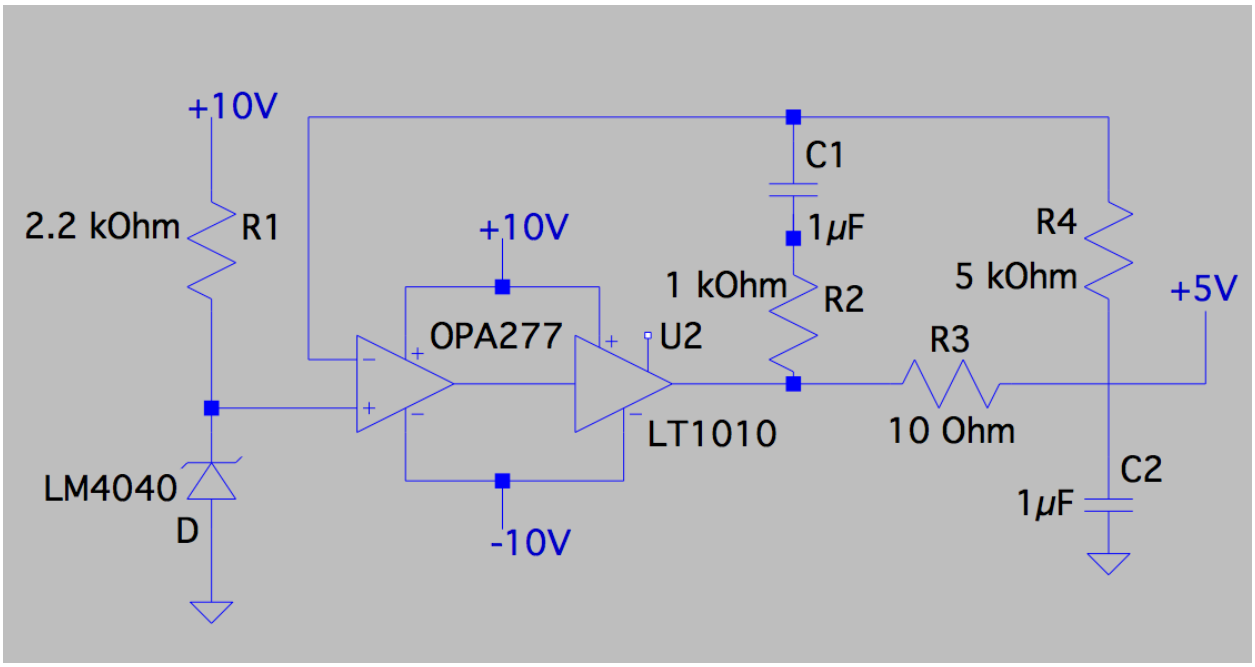

Figure B5: A circuit producing +5 V from the +10 V rail

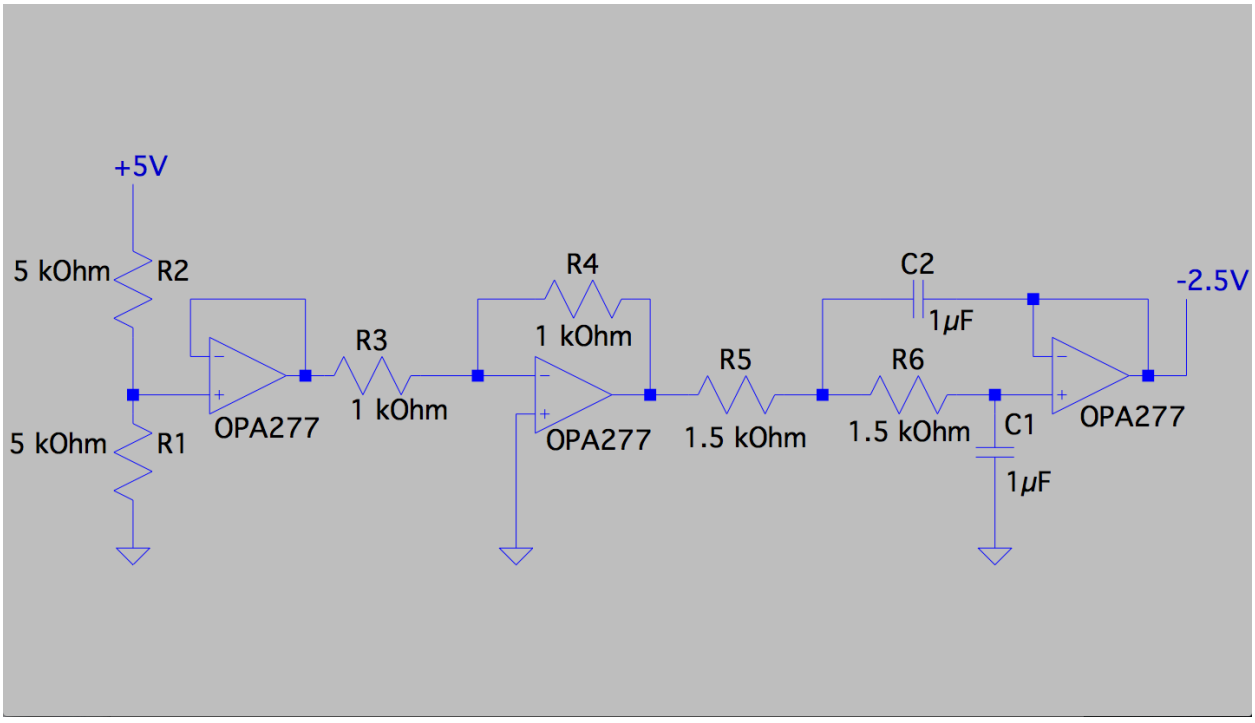

Figure B6: A circuit producing -2.5 V from the +5 V rail

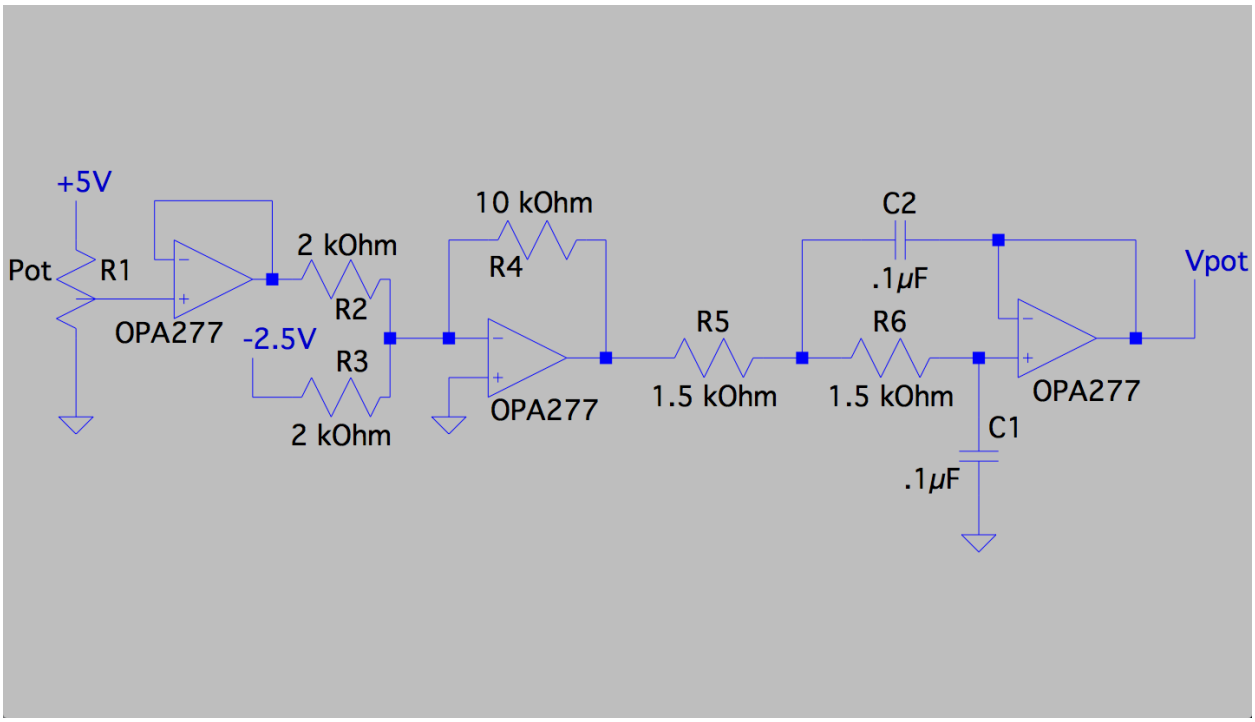

Figure B7: A circuit processing each potentiometer output signal. The potentiometer output range of was amplified ~21x for each potentiometer. The voltage was offset to keep the new range of outputs within the readable range of the analog input board. Low-pass filters were included to remove harmonic emissions that may impact the potentiometer signal.

APPENDIX C

Appendix C is composed of the computer code used to control the robot.

```
% rotationX.m
% Creates a rotation matrix about the x axis by "th" radians
function R = rotationX(th)
R = [ 1    0     0; ...
    0    cos(th) -sin(th); ...
    0    sin(th) cos(th)];
end
```

```
% rotationY.m
% Creates a rotation matrix about the y axis by "th" radians
function R = rotationY(th)
R = [cos(th)  0    sin(th); ...
    0        1      0; ...
    -sin(th) 0    cos(th)];
end
```

```
% rotationZ.m
% Creates a rotation matrix about the Z axis by "th" radians
function R = rotationZ(th)

R = [cos(th) -sin(th) 0; ...
    sin(th)  cos(th) 0; ...
    0        0       1];

end
```

```
% Adjoint.m
% Creates an adjoint matrix of a given matrix "g"
function [ Adg ] = Adjoint( g )
Adg = [ g(1:3,1:3) hat3(g(1:3,4))*g(1:3,1:3);
        zeros(3,3) g(1:3,1:3)];

end
```

```
% hat.m
% a generalization of the skew-symmetric matrix w^ in so(3)
function xhat = hat(x)
xhat = [ 0 -x(6) x(5)  x(1); ...
```

```
        x(6) 0   -x(4) x(2); ...
        -x(5) x(4) 0   x(3); ...
        0      0   0    0];
end
```

```
% forward_kinematics.m

% Establish angle variables for calculations
syms phi theta1 theta4 alpha1 alpha2 alpha3 real

% Known distances of the system
d1 = .191;
l1 = .178;
l4 = .165;
sigma = .0292;

% Coordinate frames defined by distances and rotation angles from the
% inertial frame
g10 = eye(4);
g20 = [rotationX(pi/2), zeros(3,1); zeros(1,3), 1];
g30 = [rotationX(pi/2), [0,0,l1]'; zeros(1,3), 1];
g40 = [rotationY(pi/2)*rotationZ(pi/2), [l4+d1,0,l1+sigma]'; zeros(1,3),1];
g50 = [rotationX(-pi/2)*rotationZ(pi), [l4+d1,0,l1+sigma]'; zeros(1,3),1];
g60 = [rotationZ(pi), [l4+d1,0,l1+sigma]'; zeros(1,3),1];

% Spatial twists
xi1_s = [0; 0; 0; 0; 0; 1];
xi2_s = [0; 0; 0; 0; -1; 0];
xi3_s = [l1; 0; 0; 0; -1; 0];
w4_s = [-1;0;0];
xi4_s = [cross(g40(1:3,4),w4_s); w4_s];
w5_s = [0;1;0];
xi5_s = [cross(g50(1:3,4),w5_s); w5_s];
w6_s = [0;0;1];
xi6_s = [cross(g60(1:3,4),w6_s); w6_s];

% Product of exponentials formula
e1 = simplify(expm(hat(xi1_s)*phi));
e2 = simplify(e1*expm(hat(xi2_s)*theta1));
e3 = simplify(e2*expm(hat(xi3_s)*theta4));
e4 = simplify(e3*expm(hat(xi4_s)*alpha1));
e5 = simplify(e4*expm(hat(xi5_s)*alpha2));
e6 = simplify(e5*expm(hat(xi6_s)*alpha3));

% Forward kinematics map for each coordinate frame
g1 = simplify(e1*g10);
```

```
g2 = simplify(e2*g20);
g3 = simplify(e3*g30);
g4 = simplify(e4*g40);
g5 = simplify(e5*g50);
g6 = simplify(e6*g60);

forward_kinematics_has_run = 1;
```

```
% Dynamics.m

% The height of the center of mass of the first three coordinate frames
hL1 = g1(3,4);
hL2 = g2*[0; .0803; 0; 1];
hL3 = g3*[.127; .0466; 0; 1];

% The transformation matrix between the center of rotation to the center
% of mass of each link of the gimbal
CoGL4 = [-.07356; -.000188; -.09852; 1];
CoGL5 = [-.0001333; -.01345; -.0684; 1];
CoGL6 = [-.00407; -.000243; -.03514; 1];

% The vector from the inertial frame to the center of mass of each link
% of the gimbal
hL4 = g4*CoGL4;
hL5 = g5*CoGL5;
hL6 = g6*CoGL6;

% Constants characteristic of the robot
g = 9.81;
m1 = 0;
m2 = .1054;
m3 = .4345;
m4 = .220718;
m5 = .28;
m6 = .316;

% Link 1 Spring Energy
% Code calculating the spring energy necessary for gravity compensation
% of Link 1 as described in Chapter 3
k1 = 1.3;
c = 2.2;
eyeletdistance = .87;
eyeletheight = 3.5;
arc = sqrt((c^2)+(c^2)-(2*c*c*cos(theta1)));
arc_fun = matlabFunction(arc);
cableheight = sqrt((eyeletheight^2)+(c^2)-(2*eyeletheight*c*cos(theta1)));
```

```
cable = sqrt((eyeletdistance^2)+(cableheight^2));
cable_fun = matlabFunction(cable);
% stretchedcable = sym('.0254')*sqrt((arc^2)+(cable^2));
% stretchedcable_fun = matlabFunction(stretchedcable/.0254);
cable = cable * .0254;
k1 = k1*4.45/.0254;
SpringEnergyL1 = 2*.5*k1*((cable)^2);
SpringEnergyL1_fun = matlabFunction(SpringEnergyL1);

% Link 4 Spring Energy
% Code calculating the spring energy necessary for gravity compensation
% of Link 4 as described in Chapter 2
k = .8;
springlen = 3;
freelength = springlen-(0.5/k);
freelength = freelength*.0254;
D1 = 7.5;
D2 = 3;
extendedlength = simplify(.0254*sqrt((D1^2)+(D2^2)-2*D1*D2*cos(pi/2-theta4-theta1)));
extendedlength_fun = matlabFunction(extendedlength);
k = k*4.45/.0254;
SpringEnergyL4 = simplify(2*.5*k*((extendedlength - freelength)^2));
SpringEnergyL4_fun = matlabFunction(SpringEnergyL4);

% Gravitational Forces
% The height of each center of mass of each link of the robot
h = [hL1;
   hL2(3,1);
   hL3(3,1);
   hL4(3,1);
   hL5(3,1);
   hL6(3,1)];

% Mass matrix of each link
m = [m1, m2, m3, m4, m5, m6];

% Summation of all energy in the system
V = m*h*g + SpringEnergyL1 + SpringEnergyL4;
V_fun = matlabFunction(V);

% Torques needed at each joint to compensate for gravity as described in
% [24]
N = [diff(V, phi);
   diff(V, theta1) - diff(V, theta4);
   diff(V, theta4);
   diff(V, alpha1);
```

```
   diff(V, alpha2);
   diff(V, alpha3)];
N = simplify(N);
N_fun = matlabFunction(N);

% Function to determine maximum torque needed for theta1 and theta4 at any
% point in time
J = zeros(6, 10000000);
i = 1;
      for th1 = -pi/2:.1:pi/2
         for th4 = -pi/2:.1:pi/2
               J(:, i) = N_fun(0, 0, 0, th1, th4);
                  i = i + 1;
         end
      end

% Determine the maximum torque that will be needed for theta1 and theta4
theta1max = max(J(2,:))
theta4max = max(J(3,:))
```

```
% Dynamics Function block in the block diagram. Calculates the motor
% torques necessary for each joint angle

function N = dynamics_fun(alpha1, alpha2, alpha3, theta1, theta4)
%DYNAMICS_FUN
%    N = DYNAMICS_FUN(ALPHA1,ALPHA2,ALPHA3,THETA1,THETA4)

%    This function was generated by the Symbolic Math Toolbox version 6.0.
%    19-Jun-2015 15:17:30


t2 = theta1+theta4;
t3 = cos(t2);
t4 = sin(t2);
t5 = cos(alpha2);
t6 = t3.*t5;
t7 = cos(alpha1);
t8 = sin(alpha2);
t9 = t4.*t7.*t8;
t10 = t6+t9;
t11 = t4.*-2.0e1+2.9e1;
t12 = cos(alpha3);
t13 = sin(alpha1);
t14 = sin(alpha3);
t15 = t4.*t8;
t16 = t3.*t5.*t7;
```

t17 = t15+t16;
t18 = t4.*t5;
t19 = t18-t3.*t7.*t8;
N = [0.0;sin(theta1).*(-5.019359439999996e-3);t3.*3.1802839919784-t4.*4.32580441536e-1+t3.*t5.*3.661484400000045e-4-t3.*t8.*1.458770544e-1+t4.*t7.*4.070657930400033e-4-t4.*t13.*3.471564377448e-1+t10.*t12.*1.26168372e-2-t10.*t14.*7.532902799999984e-4-t3.*1.0./sqrt(t11).*(sqrt(t11).*1.2e1-1.9e1).*3.3909e-1+t4.*t5.*t7.*1.458770544e-1+t4.*t7.*t8.*3.661484400000045e-4+t4.*t12.*t13.*7.532902799999984e-4+t4.*t13.*t14.*1.26168372e-2;t3.*(t7.*1.490717228395421e72+t13.*1.74797274311606e69+t5.*t13.*6.264076208245784e71-t7.*t12.*3.234688101058061e69-t7.*t14.*5.417769782430591e70+t8.*t13.*1.572270389694911e69+t8.*t12.*t13.*5.417769782430591e70-t8.*t13.*t14.*3.234688101058061e69).*2.328787989647591e-73;t4.*t5.*(-1.458770544e-1)-t4.*t8.*3.661484400000045e-4-t12.*t17.*1.26168372e-2+t14.*t17.*7.532902799999984e-4-t3.*t5.*t7.*3.661484400000045e-4+t3.*t7.*t8.*1.458770544e-1;t12.*t19.*(-7.532902799999984e-4)-t14.*t19.*1.26168372e-2-t3.*t12.*t13.*1.26168372e-2+t3.*t13.*t14.*7.532902799999984e-4];

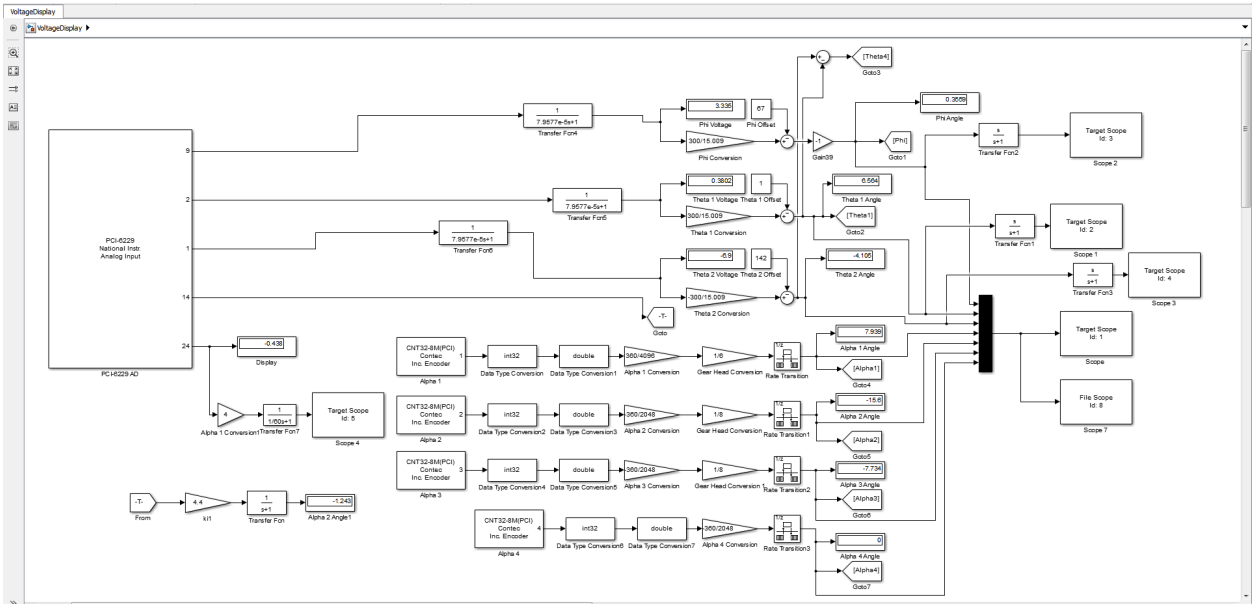

Figure C1: Reading all joint angles

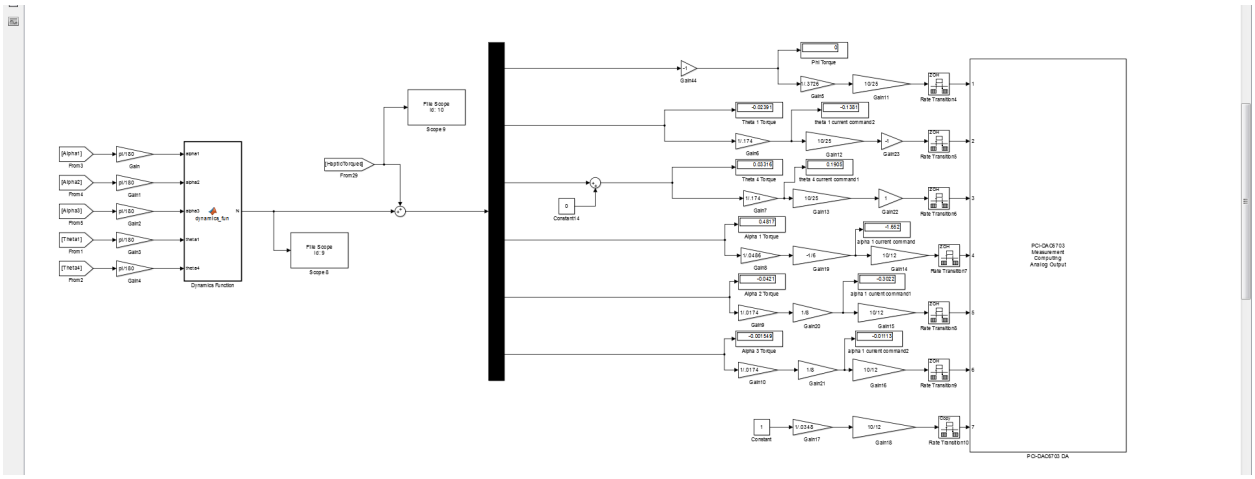

Figure C2: Determine the joint torques for gravity compensation from the dynamics and add the haptic box torques

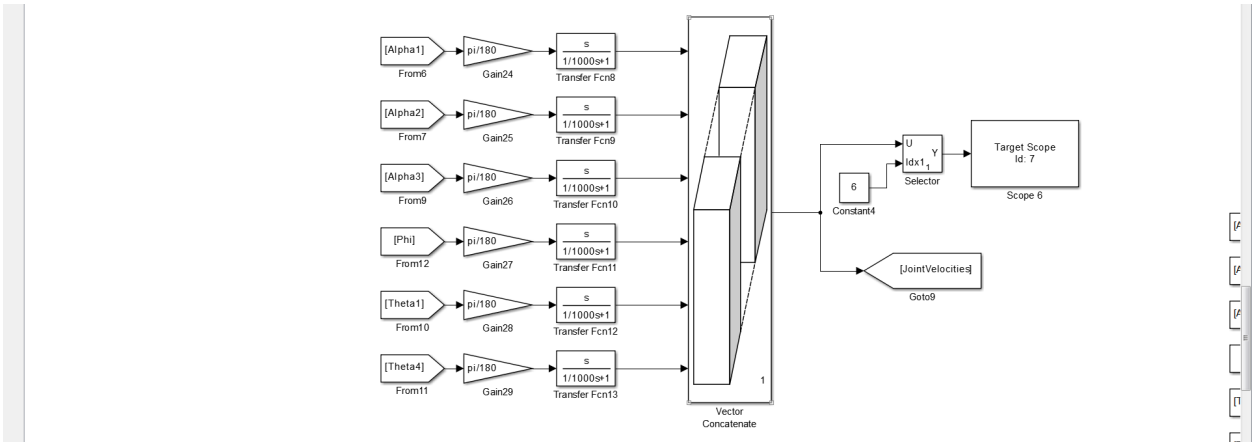

Figure C3: Computing joint velocities

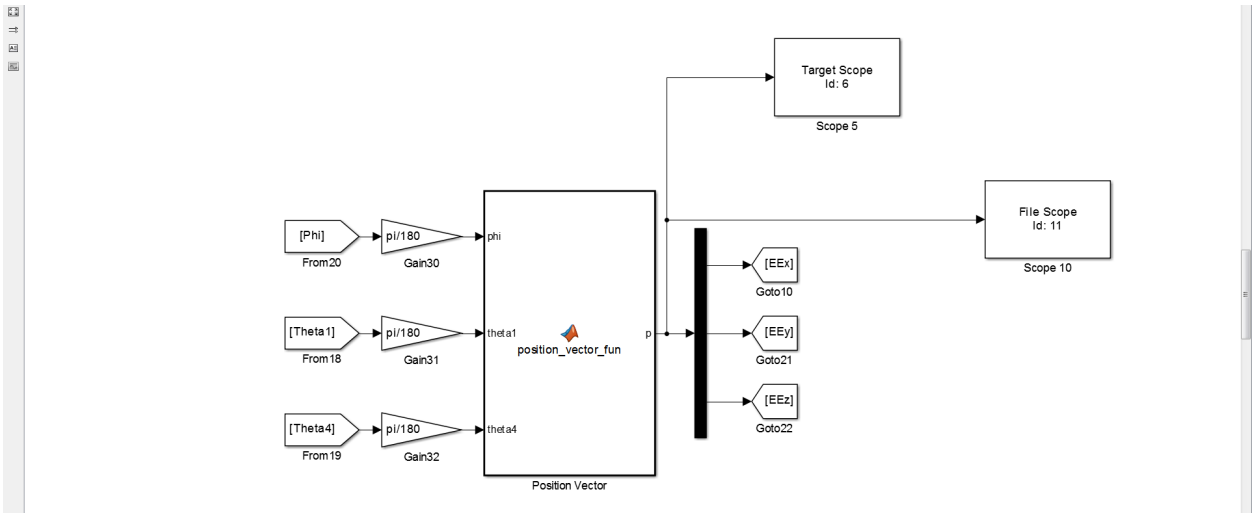

Figure C4: Determines the position of the end effector

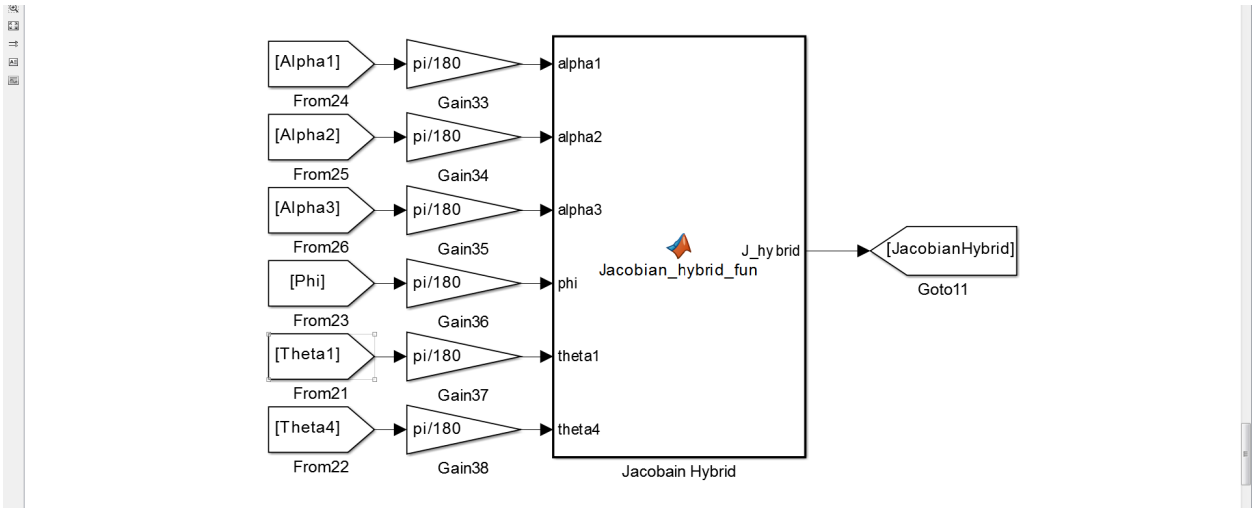

Figure C5: Computes the hybrid jacobian

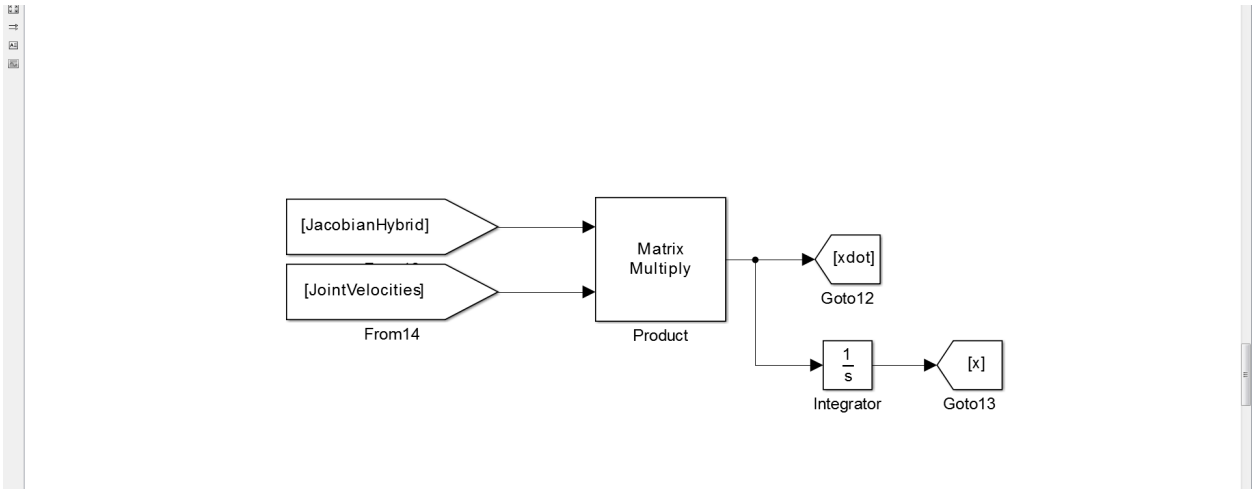

Figure C6: Computes the end effector velocity

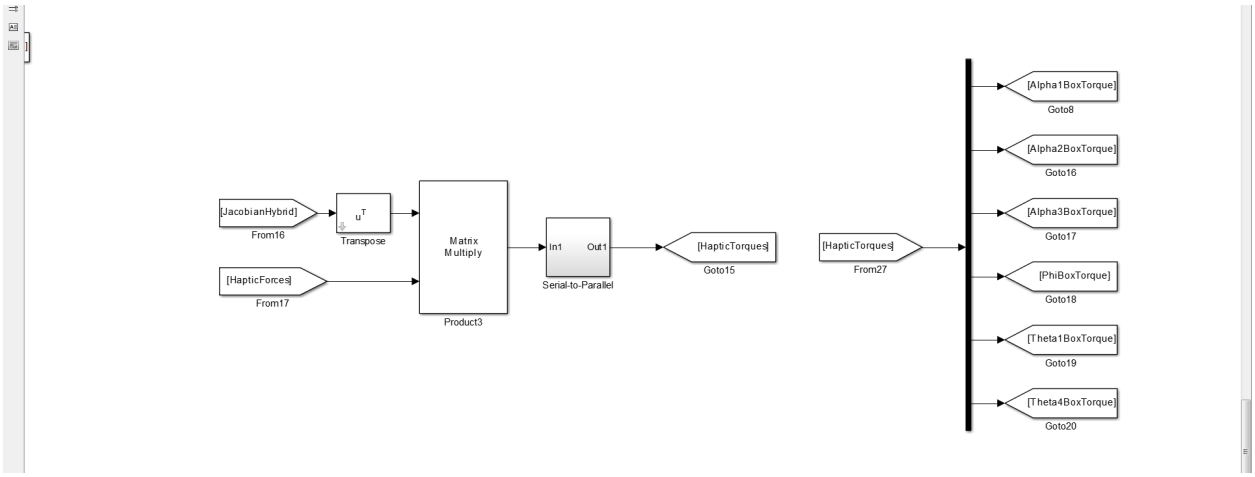

Figure C7: Computes the haptic torques

APPENDIX D

Appendix D contains all tables referenced

Data Type	Terminal Number	Corresponding Port Number
ϕ		
Current Monitor Out	23	AI 15
Current Reference Out	57	AI 7
Inhibit In	19	P0.4
Potentiometer Out	34	AI 8
θ_1		
Current Monitor Out	58	AI 14
Current Reference Out	25	AI 6
Inhibit In	52	P0.0
Potentiometer Out	33	AI 1
θ_2		
Current Monitor Out	26	AI 13
Current Reference Out	60	AI 5
Inhibit In	51	P0.5
Potentiometer Out	68	AI 0
α_1		
Current Monitor Out	61	AI 12
Current Reference Out	28	AI 4
Inhibit In	17	P0.1
Fault Out	16	P0.6
α_2		
Current Monitor Out	63	AI 11
Current Reference Out	30	AI 3
Inhibit In	49	P0.2
Fault Out	48	P0.7
α_3		
Current Monitor Out	31	AI 10
Current Reference Out	65	AI 2
Inhibit In	47	P0.3
Fault Out	46	PFI 11/P2.3
α_4		
Current Monitor Out	66	AI 9
Current Reference Out	J23	AI 31
Inhibit In	45	PFI 10/P2.2
Fault Out	11	PFI 0/P1.0

Table D1: Connections between the servoamps and the National Instruments Analog Input board

REFERENCES

[1] Tholey, Gregory. "A General-Purpose 7 DOF Haptic Device: Applications Toward Robot-Assisted Surgery." *IEEE/ASME Transactions on Mechatronics* Vol. 12. No. 6 (2007): 662-669.

[2] Healthgrades, *The fifth Annual HealthGrades Patient Safety in American Hospitals Study,* news story, Apr. 2008.

[3] Suematsu M.D., Ph.D., Yoshihiro, Pedro J. del Nido, M.D. "Robotic Pediatric Cardiac Surgery: Present and Future Perspectives." *The American Journal of Surgery* Vol. 1888. Issue 4 (2004): 98-103.

[4] A.M. Okamura, (2004), "Methods for haptic feedback in teleoperated robot-assisted surgery", Industrial Robot: An International Journal, Vol. 31 Iss 6 pp.499-508

[5] Coles, Timothy R., Dwight Meglan, Nigel W. John. "The Role of Haptics in Medical Training Simulators: A Survey of the State of the Art." *IEEE Transactions on Haptics* Vol. 4. No.1 (2011): 51-66.

[6] Y. Zhu, D.R. Magee, D. Kessel, and R. Ratnalingam, "A Virtual Ultrasound Imaging System for the Simulation of Ultrasound-Guided Needle Insertion Procedures," *Proc. Medical Image Understanding and Analysis*, pp. 61-65, 2006.

[7] V.L. Barker, "Cathsim," *Studies in Health Technology and Informatics*, vol. 62, pp. 36-37, 1999.

[8] A.J. Vickers, C.J. Savage, M. Hruza, I. Tuerk, P. Koenig, L. Martinez-Pineiro, G. Janetschek, and B. Guillonneau, "The Surgical Learning Curve for Laparoscopic Radical Prostatectomy: A Retrospective Cohort Study," *The Lancet Oncology*, vol. 10, no. 5, pp. 475-480, May 2009.

[9] Satava, R.M. (1998), "The Virtual Surgeon," *The Sciences*, 38: 34-39

[10] Shennib H, Bastawisy A, Mack MJ, Moll FH. Computer-assisted telemanipulation: an enabling technology for endocopic coronary artery bypass. Ann Thorac Surg. 1998; 66:1060-1063.

[11] Bethea BT, Okamura AM, Kitagawa M, *et al.* Application of haptic feedback to robotic surgery. *J Laparoendosc Adv Surg Techn A* 2004; **14**(3): 191–195.

[12] Wagner, C.R., Stylopoulos, N. and Howe, R.D. (2002), "*The role of force feedback in surgery: analysis of blunt dissection*", *Proceedings of the 10th Symposium on Haptic Interfaces for Virtual Environments and Teleoperator Systems*, Orlando, FL, March 2002, pp. 68-74.

[13] N.A. Langrana, G. Burdea, K. Lange, D. Gomez, and S. Despande, “Dynamic Force Feedback in a Virtual Knee Palpation,” *Artificial Intelligence in Medicine*, vol. 6, no. 4, pp. 321-333, Aug. 1994.

[14] G. Burdea, G. Patounakis, V. Popescu, and R.E. Weiss, “Virtual Reality-Based Training for the Diagnosis of Prostate Cancer,” *IEEE Trans. Biomedical Eng.*, vol. 46, no. 10, pp. 1253 – 1260, Oct. 1999.

[15] M. Mclaughlin, I. Cohen, M. Desbrun, L. Hovanessian, M. Jordan-Marsh, S. Narayanan, G. Sukhatme, P. Georgiou, S. Ananthakrishnan, W. Peng, and W. Zhu, “Haptic Simulator for Training in Clinical Breast Examination,” Annenberg School for Comm., 2003.

[16] S. Baillie, A. Crossan, S. Brewster, D. Mellor, and S. Reid, “Validation of a Bovine Rectal Palpation Simulator for Training Veterinary Students,” *Studies in Health Technology and Informatics*, vol. 111, pp. 33-36, 2005.

[17] Z. Mayooran, L. Watterson, P. Withers, J. Line, W. Arnett, and R. Hortley, “Mediseus Epidural: Full-Procedure Training Simulator for Epidural Analgesia in Labour,” *Proc. SimTecT Healthcare Simulation Conf.*, 2006.

[18] M.A. Srinivasan, “Video of Episim,” http://www.sensable.com/industries-simulation-visualisation.htm, Oct. 2007.

[19] C.K. Chui, J.S.K. Ong, Z.Y. Lian, Z. Wang, J. Teo, J. Zhang, C.H. Yan, S.H. Ong, S.C. Wang, H.K. Wong, C.L. Teo, and S.H. Teoh, “Haptics in Computer-Mediated Simulation: Training in Vertebroplasty Surgery,” *Simulation and Gaming*, vol. 37, no. 4, pp. 438-451, Dec. 2006.

[20] Kim, Seahak, J. J. Berkley, and M. Sato. "A novel seven degree of freedom haptic device for engineering design." *Virtual Reality* 6.4 (2003): 217-228.

[21] Perry, Carl M. "Design of a High Performance Robot for Use In Haptic Interface and Force Feedback Research." Thesis. Graduate School of Vanderbilt University, 1997. Print.

[22] “Man-Systems Integration Standards.” NASA. Volume 1, Section 4.8, May 2015

[23] Herder, Just. “Energy-free Systems.” Thesis. Technische Universiteit Delft, 2001. Print.

[24] Murray, Richard M., Zexiang Li, and S. Shankar Sastry. *A Mathematical Introduction to Robotic Manipulation*. N.p.: CRC, 1994. Print.

[25] James, John T., PhD. "A New, Evidence-based Estimate of Patient Harms Associated with Hospital Care." *Journal of Patient Safety* 9.3 (2013): 122-28. Print.